

Universität Potsdam, Institut Physik und Astronomie, Karl-Liebknecht-Str 24/25, Gebäude
28 D-14476, Potsdam, Deutschland

Thinning and Turbulence in Aqueous Films

Diplomarbeit in Physik

angefertigt am
Institut für Physik und Astronomie
Arbeitsgruppe für statistische Physik und Chaostheorie

eingereicht an der
Mathematisch-Naturwissenschaftlichen Fakultät der Universität Potsdam

von

Michael Winkler

Potsdam,
21. Februar 2011

Erstgutachter: Dr. Markus Abel, Institut für Physik an der Universität Potsdam

Zweitgutachter: Dr. Rumen Krastev, Naturwissenschaftliches und Medizinisches Institut an
der Universität Tübingen

This work is licensed under a Creative Commons License:
Attribution - Noncommercial - Share Alike 3.0 Germany
To view a copy of this license visit
<http://creativecommons.org/licenses/by-nc-sa/3.0/de/>

Published online at the
Institutional Repository of the University of Potsdam:
URL <http://opus.kobv.de/ubp/volltexte/2011/5310/>
URN [urn:nbn:de:kobv:517-opus-53107](http://nbn-resolving.org/urn:nbn:de:kobv:517-opus-53107)
<http://nbn-resolving.org/urn:nbn:de:kobv:517-opus-53107>

Abstract

This thesis covers the topic "Thinning and Turbulence in Aqueous Films". Experimental studies in two-dimensional systems gained an increasing amount of attention during the last decade. Thin liquid films serve as paradigms of atmospheric convection, thermal convection in the Earth's mantle or turbulence in magnetohydrodynamics. Recent research on colloids, interfaces and nanofluids lead to advances in the development of micro-mixers (lab-on-a-chip devices). In this project a detailed description of a thin film experiment with focus on the particular surface forces is presented. The impact of turbulence on the thinning of liquid films which are oriented parallel to the gravitational force is studied.

An experimental setup was developed which permits the capturing of thin film interference patterns under controlled surface and atmospheric conditions. The measurement setup also serves as a prototype of a mixer on the basis of thermally induced turbulence in liquid thin films with thicknesses in the nanometer range. The convection is realized by placing a cooled copper rod in the center of the film. The temperature gradient between the rod and the atmosphere results in a density gradient in the liquid film, so that different buoyancies generate turbulence.

In the work at hand the thermally driven convection is characterized by a newly developed algorithm, named Cluster Imaging Velocimetry (CIV). This routine determines the flow relevant vector fields (velocity and deformation). On the basis of these insights the flow in the experiment was investigated with respect to its mixing properties. The mixing characteristics were compared to theoretical models and mixing efficiency of the flow scheme calculated.

The gravitationally driven thinning of the liquid film was analyzed under the influence of turbulence. Strong shear forces lead to the generation of ultra-thin domains which consist of Newton black film. Due to the exponential expansion of the thin areas and the efficient mixing, this two-phase flow rapidly turns into the convection of only ultra-thin film. This turbulence driven transition was observed and quantified for the first time. The existence of stable convection in liquid nanofilms was proven for the first time in the context of this work.

Zusammenfassung

Diese Diplomarbeit behandelt das Thema "Dünnung und Turbulenz in wässrigen Filmen". Experimente in zweidimensionalen Systemen erfuhren in den vergangenen Jahren zunehmend an Aufmerksamkeit. Dünne Flüssigkeitsschichten dienen als Modell für atmosphärische Konvektion, thermische Konvektion im Erdmantel oder Turbulenz in der Magnetohydrodynamik. Aktuelle Forschung im Bereich der Kolloide, Grenzflächen und Nanofluidik führt zu Fortschritten in der Entwicklung von Mikromixern ("lab-on-a-chip"). In diesem Projekt wird eine detaillierte Beschreibung eines Dünnschichtexperiments mit Fokus auf die besonderen Oberflächenkräfte vorgestellt. Die Auswirkung der Turbulenz auf die Dünnung von parallel zur Gravitationskraft orientierten Flüssigkeitsschichten wurde untersucht.

Es wurde ein Experiment entwickelt, welches die Aufnahme von Dünnschichtinterferenzmustern unter kontrollierten Oberflächenbedingungen und Atmosphäre erlaubt. Der Messaufbau dient auch als Prototyp eines Mixers auf Basis von thermisch induzierter Turbulenz in Flüssigkeitsfilmen mit Dicken im Nanometerbereich. Die Konvektion wird durch das Platzieren eines gekühlten Kupferstabs in der Mitte des Films realisiert. Der Temperaturgradient zwischen Stab und äußerer Atmosphäre resultiert in einem Dichtegradienten in dem flüssigen Film, sodass durch unterschiedliche Auftriebskräfte Turbulenz erzeugt wird.

In der vorliegenden Arbeit ist die thermisch getriebenen Konvektion an Hand eines neu entwickelten Verfahrens (Cluster Imaging Velocimetry - CIV) zur Ermittlung des strömungsrelevanten Vektorfeldes (Geschwindigkeit und Deformation) charakterisiert worden. Auf Basis dieser Erkenntnisse wurde die im Experiment vorherrschende Strömung in Hinsicht auf ihre Mischungseigenschaften im Vergleich zu theoretischen Modellen untersucht und die Mischungseffizienz berechnet.

Die gravitationsgetriebene Ausdünnung der Flüssigkeitsschicht unter Einfluss der Turbulenz wurde analysiert. Durch starke Scherkräfte kommt es lokal zur Bildung ultradünner Domänen bestehend aus "Newton black film". Diese Zweiphasenströmung geht durch das exponentielle Ausdehnen der dünnen Bereiche und die effiziente Mischung sehr schnell in eine Konvektion von ausschließlich ultradünnem Film im Gleichgewichtszustand über. Dieser turbulenzgetriebene Übergang wurde zum ersten Mal beobachtet und quantifiziert. Die Existenz stabiler Konvektion in flüssigen Nanofilmen ist zum ersten Mal im Rahmen dieser Arbeit belegt worden.

Contents

1. Introduction	1
2. Thin Films	3
2.1. Chemical Composition of the Thin Films	3
2.2. Governing Equations of the Membrane Stability	5
2.2.1. Marangoni Flow	5
2.2.2. Disjoining Pressure	5
2.2.3. Formation of Common and Newton Black Film	7
2.2.4. Electrolyte Concentration and Newton Black Films	7
2.2.5. Marginal Regeneration	8
2.2.6. Capillary Pressure	11
2.2.7. Surface Viscosity and Surface Elasticity	11
2.3. Thickness Profiling Methods	12
2.4. Fluid Dynamics	14
3. Mixing and Theory	16
3.1. Basic Definition of Mixing	16
3.2. Fixed Points and Orbits	16
3.3. Baker's Transformation	19
3.4. Linked Twist Maps	22
4. Experiment	23
4.1. Setup	23
4.2. Limitations	25
4.2.1. Atmosphere	25
4.2.2. Contrast of Video Data	26
4.2.3. Crystallization	26
4.3. Solution Design and Measuring Procedure	28
4.4. Motion Capturing System	29
4.4.1. Influence of Software Filters	29
5. Convection	31
5.1. Convection Velocity	31
5.2. Flow Field Characterization	33
5.2.1. Cluster Imaging Velocimetry	33
5.2.2. Velocity and Deformation Distribution	36
5.3. Air Convection Velocity	43
6. Mixing	45
6.1. Spatial and Spectral Analysis	45
6.1.1. Scale and Aspect Ratio Considerations	49

6.2. Key Elements and Quality of Mixing	50
6.3. Fluid Transfer between Convection Rolls	52
6.4. Mixing Efficiency	56
7. Thinning	58
7.1. Intrinsic Thin Film Effects and Regular Thinning	58
7.2. Superfast Thinning	60
7.2.1. Thinning and Turbulence	60
7.2.2. Superfast Thinning	61
8. Discussion	66
8.1. Turbulence	66
8.2. Mixing	67
8.3. Thinning	69
9. Outlook	70
A. Appendix	71
A.1. Cluster Algorithm Source Code	71
A.2. Publications	74
B. Bibliography	81

Acknowledgments

First and foremost, I would like to express my gratitude to my supervisor Dr. Markus Abel who was always a great motivator, helpful with detailed theoretical explanations and overall very enthusiastic about this topic. I am equally indebted to Dr. Rumen Krastev for fruitful discussions and an unbureaucratic cooperation with the Max Planck Institute for Colloids and Interfaces. I would like to show my gratitude to Professor Ke-Qing Xia for kindly welcoming me into his research group at the Chinese University of Hong Kong. I would also like to sincerely thank Dr. Silke Stöckle for helpful discussions about thin films and experimental obstacles. Additionally, I am indebted to Dr. Gugli Kofod for his contributions in questions regarding cryogenics and kindly making lab space and equipment available. I would like to say thank you to all friends who helped shaping this documents with thoughtful recommendations and peer reviews. In conclusion, I would also like to thank my parents for their kind support during every step of my physics diploma which culminates in this thesis.

List of Figures

2.1. Disjoining pressure isotherm	6
2.2. Flow scheme proposed by Stein [42]	10
3.1. Basic orbit scheme	17
3.2. Orbit schematic for the presented experiment	18
3.3. Representation of a Baker's transformation and Smale-Horseshoe-Map . .	20
3.5. Sequence of the captured turbulent motion at an earlier stage	21
3.6. Sequence of the captured turbulent motion at a later stage	21
3.4. Basic sequence of the development of a horseshoe in the flow field	21
4.1. Measurement Cell Assembly	24
4.2. Laboratory Setup	24
4.3. Creation of the cooling disc	27
4.4. Sequence of snapshots of a perturbation at the crystallization disc	28
5.1. Velocity profile of an advected cluster for two full rotations	32
5.2. Sequence of ProAnalyst blob tracking snapshots	33
5.3. Example of the cluster identification for one frame	35
5.4. Absolute velocity distribution	37
5.5. Absolute deformation distribution in the thin film.	38
5.6. Distribution of the major principal axis	39
5.7. Distribution of the minor principal axis	39
5.8. Average velocity vector field	40
5.9. High speed convection with cooling rod contact. Min.lifetime: 2 frames .	41
5.10. High speed convection with cooling rod contact. Min. lifetime: 3 frames .	42
5.11. Low speed angular velocity distribution	42
5.12. Velocity and acceleration of a particle advected in the cooling jet	43
6.1. Temporal evolution of a horizontal line probe (1)	46
6.2. Temporal evolution of a horizontal line probe (2)	46
6.3. Normalized variance of the center cut images	47
6.4. Plot of the spatial frequency over time of figure 6.2 (1)	48
6.5. Pplot of the spatial frequency over time of figure 6.2 (2)	49
6.6. Simplified scheme of the turbulent branching of fluid filaments	51
6.7. Snapshots taken from the motion tracking software proAnalyst	51
6.8. Individual snapshots of fluid transport at the bottom center secction . . .	53
6.9. Peak extraction of the fluid transfer area over time	53
6.10. Frequency power spectrum of the inter-convection roll fluid transfer . . .	55
6.11. Averaged path of fluid involved in transfer between convection rolls . . .	55
6.12. Stretching rate distribution	57
7.1. Thinning snapshots taken at two different stages of the film thinning . .	59

7.2. Sequence of snapshots while introducing turbulence in black film	60
7.3. Sequence of snapshots of the developing film destabilization	62
7.4. Thinning of an unperturbed and turbulent film over time	64

List of Symbols

k	Boltzmann constant
Γ	surface concentration of the surfactant
h_{head}	length of the surfactant head group
h_{core}	thickness of the aqueous core surfactant headgroups + water (without tails)
h_{tail}	length of the surfactant carbon chain tail
ϵ	dielectric constant in the medium
A	Hamaker constant
κ	inverse Debye length
Ψ_0	surface potential
h	total film thickness: $h_{core} + 2 \cdot h_{tail}$
R_w	specific gas constant for water - $461,52 \frac{J}{kg K}$
e	vapor pressure
W^s	stable manifold
W^u	unstable manifold
$\vec{\Phi}_t$	flow / mapping function at time t
\vec{T}	stress tensor at the liquid interface
\vec{n}	unit vector normal to the fluid surface
\vec{t}	unit vector parallel to the fluid surface
η	bulk viscosity of the solution
ρ	bulk density of the solution
σ	local surface tension of the thin liquid film
χ	surface curvature
d	overall film thickness

1. Introduction

In this work a novel approach on fluid dynamics in thin liquid films is presented covering three different research topics: Interface science on a molecular level; Fluid dynamics and chaos theory to analyze the mixing behavior. Surface forces govern the behavior of thin films in their equilibrium and transient thinning state. Driving the thin film with an external force makes it necessary to involve fluid dynamic models for the bulk fluid movement. Due to the nature of the convection, a statistical analysis in terms of mixing theorems is presented.

An essential step in the understanding of thermal convection and turbulence in three-dimensional real world examples is the investigation of fundamental fluid behavior in well defined small scale experiments. Examples are planetary atmospheres or convection in the outer mantle of the Earth's core. Another fundamental area of research that is usually treated as two-dimensional turbulence is magnetohydrodynamics. The restriction to two dimensions simplifies the set of necessary equations describing the system and significantly reduces the processing power for comparable computational models.

surface science Thin foam films are the center of attention of this thesis. These self-sustained fluid layers and are used for fluid dynamic experiments. Due to the confinement of the velocity field to a surface they can be treated as two-dimensional. Their properties are discussed with regard to their specific surface physics and chemistry.

Longterm stability of soap films is an ever-present issue. Conventional soap film experiments in fluid dynamics rely on commercial solutions that are not well controlled in their composition [11, 16, 18]. Especially the presence of anti-foaming agents diminishes film stability. Furthermore, it is essential that the atmosphere around the thin film is well controlled to yield a reliable relation of the chemical components and prevent changes and premature rupture due to evaporation or contamination. In collaboration with the Max Planck Institute of Colloids and Interfaces (MPI-KG) a measurement cell was designed which minimizes the number of uncontrolled parameters and is capable of maintaining a soap film for a long period of time. The presented setup is ideal for a hydrodynamical classification of turbulent motion in liquid thin films. The specific surfactant used to stabilize the thin sheet of water has been used in a variety of experiments at the MPI-KG and is well characterized in its chemical and physical properties.

fluid dynamics An additional motivation is the need of further understanding of nano thin films in turbulent motion. The characteristics of thin films are well known in the equilibrium regime. This thesis provides an experimental approach to merge the knowledge on turbulent convection with the governing surface forces.

In this thesis a temperature gradient is introduced into the thin liquid film via a cooled copper rod. This leads to buoyancy driven turbulence due to the different densities inherent to the temperature gradient.

One of the main advantages of the developed setup and analytical methods is the ability to characterize thermal convection in a very cost-efficient manner. The solution volume involved in the experiment is vastly smaller compared to other large scale convection experiments which produce high maintenance costs.

Additionally, the integration of comprehensive knowledge about surfactant layers into a turbulence experiment results in a well defined system, both from a fluid dynamics and surface science point of view. Sophisticated models and experience with surfactant stabilized equilibrium films already exist yielding an excellent tool to analyze fluid dynamics with the presented setup.

Recent turbulence experiments are based on flowing soap solutions [33, 38], external actuation via airstreams [6] or temperature gradients induced by heating the film in experiments similar to Rayleigh-Bénard-Convection in bulk media [47, 48]. In this study we focus on thermally forced convection, which disqualifies moving soap films as their flow speed is too high to accurately observe buoyancy driven flows.

Heating a thin liquid film poses two distinct complications. Firstly, the vapor pressure is lowered which enhances evaporation. Secondly, due to thermal excitation the thin film stability is diminished. Both obstacles can be overcome by shifting the temperature gradient realized by cooling the thin film instead of heating it. The perturbation is introduced via a cooling rod placed at the center of the thin liquid film. Two stable convection rolls form below the cooling rod filling the lower half of the frame.

mixing The thermally driven convection exhibits several chaotic properties which leads to the characterization of the two-dimensional turbulence in terms of mixing theorems. Furthermore, its mixing efficiency is calculated from the information about folding and stretching obtained from the flow field characterization.

thinning Another aspect is the thinning of macroscopic liquid thin films with regards to dynamic effects. Particularly the influence of turbulent motion and mechanisms that are present at the frame-film interface namely marginal regeneration.

This study is not only concerned with the thick transient state visualized in most fluid dynamic experiments involving soap films but also with the interaction of ultra-thin Newton black films.

In the presence of turbulent motion in the thin film the generation of black film and the speed of thinning are severely altered. The analysis presented here are congruent with results obtained from heat-induced turbulence experiments conducted during a cooperation with the research group of Professor Ke-Qing Xia at the Chinese University of Hong Kong. The main driving force of the turbulence is a gravitational drift due to a density increase of the cooled liquid.

2. Thin Films

To understand the behavior of freestanding thin liquid films, it is necessary to identify the governing surface forces. In this chapter, an insight into the chemical components used for the experiments is given and the concepts of black film formation, marginal regeneration and the influence of disjoining pressure are described. Since the system is in a transient state during the turbulent motion not only static equilibrium equations need to be considered but fluid dynamic concepts need to be discussed as well. Furthermore, an overview about possible observation techniques regarding thin films is given with emphasis on visible light reflection spectra.

2.1. Chemical Composition of the Thin Films

General Composition Macroscopic foam films are investigated in this study. These films are obtained by filling an aluminum frame with surfactant solution creating a quasi two-dimensional liquid film with an area of several square centimeters. The base solvent is deionized water with a residual conductivity of $1.37 \mu S/cm$. Generally, it is recommended to use purified Mili-Q® water to create solutions [25] as it reduces contaminations with non-conducting carbon chain remnants. However, comparing experiments revealed that soap film stability and black film formation were not affected by the type of water used.

A film consisting of only pure water ruptures almost immediately due to the capillary forces generated by the surface tension. Adding a surfactant that covers the surface of the film generally reduces the surface tension and increases the surface elasticity, therefore stabilizing the sheet of water. In this work the sugar-based non-ionic surfactant n-dodecyl- β -maltoside is used and its properties will be discussed in detail in the following.

Another key component to create macroscopically large films with an area of several square centimeters or meters [23, 19] is glycerin. Due to its high viscosity of $\eta = 945 mPa \cdot s$ it reduces the thinning speed of vertical films and allows the film to remain stable for a longer period of time [13]. In general a concentration of 25 %_{vol} was used which yields a net viscosity of roughly $2 mPa \cdot s$ [34]. Experiments on 2D fluid dynamics frequently involve a constant stream of soap solution [19, 38, 46] that require a different approach on the composition [33]. The key quantities determining the amount of glycerin are bulk and surface viscosity which will be discussed in detail in section 2.2.7.

The last ingredient characterizing a thin film in the presented setup is the electrolyte concentration. Commonly used electrolyte types are sodium chloride ($NaCl$), lithium chloride ($LiCl$), calcium chloride ($CaCl_2$) and aluminium chloride ($AlCl_3$) [49]. For the ease of use sodium chloride was chosen as the influence on surface tension and critical micelle concentration (CMC) of the particular type of ions is negligible. To eliminate

any surface active contaminations the laboratory grade $NaCl$ was roasted at 600°C . The desired effect of adding ions to the solution is to shield the electrostatic double-layer repulsion as described by the DLVO-theory [8] hence controlling the final thickness of the film. A detailed description of the influence of ions on the solution is given in section 2.2.4.

Surfactant This study focuses on the application of n-dodecyl- β -maltoside as a surface stabilizing surfactant. It belongs to a group of new generation sugar-based surfactants which are synthesized using environment-friendly and low-cost chemicals. The biological advantages of maltosides are of lesser importance for the presented fluid-dynamical analysis but allow experiments with relatively low safety precautions. The decision of specifically using n-dodecyl- β -maltoside was made in discussion and cooperation with the Max Planck Institute of Colloids and Interfaces which is at front and center of the investigation of the physical and chemical properties of sugar-based surfactants. Especially the recent work of Dr. Rumen Krastev and his Co-workers [41, 25] provides a detailed background on the physical behavior of this surfactant.

N-dodecyl- β -maltoside (here after β - $C_{12}G_2$) consists of a hydrophilic headgroup which is made up of two glucose rings ($C_6H_{12}O_6$) connected by an ether bond and a hydrophobic alkyl chain ($C_{12}H_{25}$). Several factors determine the surface activity (usually expressed in mol per surface area) of an amphiphilic molecule. At the critical micelle concentration (CMC) the surfactant spontaneously starts to aggregate into micelles hence shielding the hydrophobic part from the aqueous solution which decreases the system free energy. The CMC is a property of the bulk material and therefore surface independent. However, below the CMC, the surface tension is greatly affected by the surfactant concentration [25, 49]. In addition, the required area per head group and the interfacial tension at concentrations above the CMC characterize the surface activity.

A typical value for the area of the head group is $A \approx 45 \text{ \AA}^2$ [2]. The hydrocarbon tail determines the order of magnitude of the critical micelle concentration as shown by Molina-Bolívar and Ruiz [32, p.70]. For β - $C_{12}G_2$ the reported CMC ranges from 0.08 to 0.25 mM [50, 25, 32, p.74]. However, for the presented research the only concern is to have a surfactant concentration above the CMC so that the density of surfactant molecules on the surface is constant. In this regime the surface tension for β - $C_{12}G_2$ is $\sigma_{CMC} = 35,3 \frac{mN}{m}$ and the area per molecule at the air-water interface is $A_{CMC} = 0,467 \text{ nm}^2$ [31].

If the surface concentration is decreased micelles close to the surface will break up and diffuse to the surface restoring the equilibrium. Vice versa, if the surface concentration is increased surfactant molecules will move into the bulk liquid. The diffusion constant for β - $C_{12}G_2$ is $D = 3.5 \cdot 10^{-10} \text{ m}^2/\text{s}$ [44]. Considering that the typical distance from a micelle to the surface is likely to be less than 100 nm the resulting time the molecule needs to reach the surface is in a rough approximation below 1 ms ($\tau_D \propto \frac{L^2}{D}$ whereas L is the characteristic length). The effects of surfactant replenishment will be assessed in conjunction with marginal regeneration (section 2.2.5).

2.2. Governing Equations of the Membrane Stability

2.2.1. Marangoni Flow

The Marangoni Effect, also called thermo-capillary convection describes a force generated by surface tension gradients. The phenomenon was studied in detail at first by Carlo Marangoni, hence the name. Areas of large surface tension exert a larger force on the liquid than the surrounding low surface tension areas. In the absence of any other forces The liquid will therefore flow towards the areas of high surface tension.

The surface tension σ is related to the scalar fields present in the system. In the presented example differences in surface concentration of the surfactant c_s at the border and the temperature gradient imposed at the cooling rod represent the scalar fields and induce surface tension gradients leading to Marangoni flows. The tangential stress balance at a free surface is given by:

$$\vec{n} \cdot \vec{T} \cdot \vec{t} = -\vec{t} \cdot \nabla \sigma \quad (2.1)$$

The tangential component of the hydrodynamic stress must be compensated by stress associated with a surface tension gradient. In a static system $\vec{n} \cdot \vec{T} \cdot \vec{t} = 0$ which implies that $\nabla \sigma = 0$. Therefore, a present surface tension gradient introduces a dynamic force into the system as tangential surface stress can only be balanced by viscous stress associated with fluid motion. It is not possible to balance the surface tension with a pressure gradient as it can only compensate stress normal to the interface.

Any fluid motion characterized by the generation or reduction of surface area will be suppressed by the surfactant due to the Marangoni stress. This results in an effective surface elasticity which gives the thin liquid layer its stability compared to a pure water film.

2.2.2. Disjoining Pressure

The repulsive forces separating the two surfaces of a free-standing foam film is called disjoining pressure (Π) (figure 2.1). Following the DLVO-theory [8] it is the sum of electrostatic repulsion Π_{el} , van der Waals attraction Π_{VdW} and a short-range repulsive part Π_{sr} :

$$\Pi(h) = \Pi_{el}(h) + \Pi_{VdW}(h) + \Pi_{sr}(h) \quad (2.2)$$

Π_{sr} cannot be described with a basic term, as surface waves, peristaltic fluctuations, protrusion of surfactants at the surface and head group overlap contribute to the short range pressure [14, 1]. Following Stubenrauch et. al. [43] Π_{sr} is controlled by head group overlap. De Gennes [7] calculated the resulting pressure to be:

$$\Pi_{sr}(h) \simeq kT\Gamma^{3/2} \left[\left(\frac{2h_{head}}{h_{core}} \right)^{9/4} - \left(\frac{h_{core}}{2h_{head}} \right)^{3/4} \right] \quad (2.3)$$

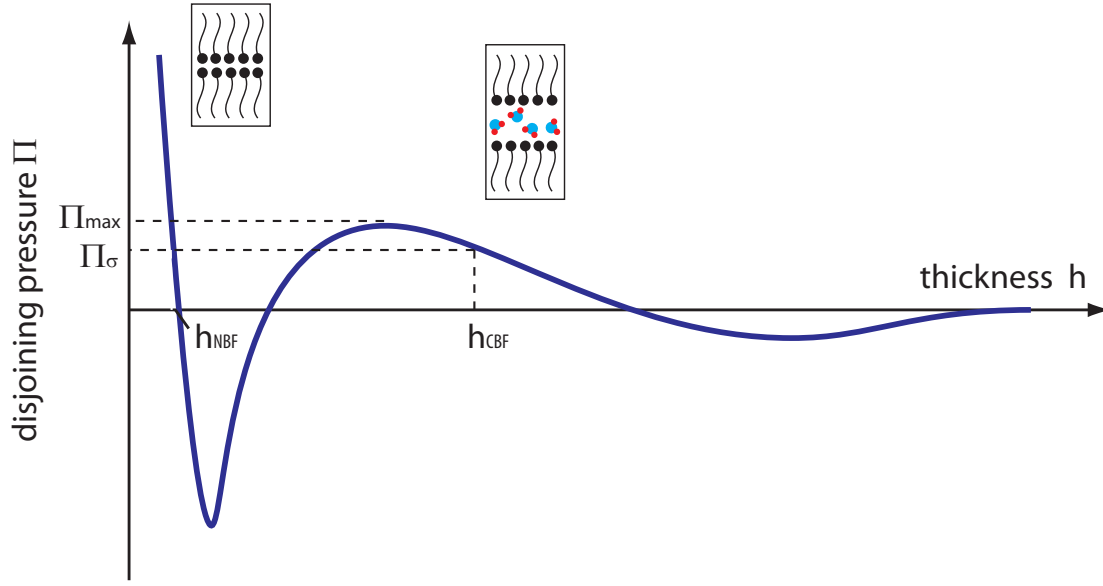


Figure 2.1.: Disjoining pressure isotherm (adapted from Exerowa [10]).

Assuming constant surface potential boundary conditions the electrostatic component Π_{el} can be calculated using a linearized Poisson-Boltzmann equation resulting in the following equation:

$$\Pi_{el} = \frac{\epsilon \kappa^2}{8\pi} \Psi_0^2 \text{sech}^2(\kappa h) \quad (2.4)$$

The electrostatic part is based on the solid charged wall model which implies that the charges are located at the air-water-interface for non-ionic surfactants. Note that the application of this model for thin films is still under debate (see [43] and references therein).

The long range attractive component of the disjoining pressure is given by the van der Waals component:

$$\Pi_{VdW} = -\frac{A}{6\pi h^3} \quad (2.5)$$

This formula represents the small thickness limit of the van der Waals contribution as electromagnetic retardation is omitted. In thicker films (infinite phase) the surrounding medium does contribute in addition to the microscopic interaction and must be considered which was first discussed in detail by Scheludko [39].

2.2.3. Formation of Common and Newton Black Film

After its creation the liquid film thins due to capillary suction at the border and additionally gravity when considering vertical films. They reach very small thicknesses in the equilibrium state and are therefore called nano foam films following the nomenclature of the IUPAC (International Union of Pure and Applied Chemistry). Depending on chemical composition of the solution two equilibrium states are distinguished: common black films (CBF) and Newton black films (NBF). The former is characterized by a thickness of $5 - 20 \text{ nm}$ and an aqueous core between the two surfactant layers. The Newton black film on the other hand is a bilayer formation without any free water. All water molecules are bound by the surfactant head group and therefore cannot move freely. The thickness of Newton Black Films depends mainly on the size of the surfactant molecule and is usually in the range of $4 - 10 \text{ nm}$ [41]. They are called black films as no light glances off their surface due to the interference condition which makes them translucent.

When the equilibrium of disjoining pressure, surface tension and hydrostatic pressure is reached the common black film stays constant in thickness. This corresponds to the point Π_σ in figure 2.1. The transition into Newton black film depends on the electrolyte concentration which is discussed in the following section. According to the DLVO-theory the disjoining pressure should decrease indefinitely until the film collapses. However, due to the formation of a molecular bilayer which is stabilized by strong short ranged repulsion a second stable equilibrium can be reached with the Newton black film at h_{NBF} .

2.2.4. Electrolyte Concentration and Newton Black Films

Following the presented theory in section 2.2.2 the local maximum in disjoining pressure $\Pi_{max}(h)$ must be overcome to reach a Newton Black Film. For microscopic films this transition is mostly dependent on the electrolyte concentration c_{el} , however, it has been reported [15] that macroscopic films with an area of several square centimeters do form Newton Black films at concentrations below $c_{el,crit}$ in the presence of perturbations. Prior investigations focus on perturbations created by heating or alpha particle irradiation [15, 9] which force a transition from Common Black Film to Newton Black Film. The effect of turbulence on the black film formation will be discussed in detail in section 7.2.2.

The electrolyte concentration does not influence the surface concentration of the surfactant, it does, however, lower the surface tension and the CMC for $\beta\text{-C}_{12}\text{G}_2$ [49]. This effect can be attributed to the strong hydration of the sugar head group which limits ion interaction thereby increasing the effective concentration of the surfactant. A similar explanation is based on the argument that the amount of work necessary to insert a surfactant molecule into the molecular structure of water is increased by salt ions. This decreases the effective solubility of the surfactant [24]. Both explanations yield the same result - limitation of interaction between ions and head groups.

Recently, it has been reported that the addition of electrolytes has a similar effect to increasing the pressure on pure water resulting in an effective pressure increase of 1.4 kbar compared to pure water [21]. This is due to the disruptive effect of Na^+ ions on the hydrogen bond structure of pure water which does not only apply to the first hydration shell of the ions but extends further into the bulk liquid [22]. On the contrary, Cl^-

ions can substitute an oxygen site in the H_2O -network without major distortions to the structure. Overall, the addition of NaCl has a disruptive character on the hydrogen-bond network of water creating more monomeric water molecules which promote hydration of the surfactant. Conclusively it must be stated that the presented arguments are mainly valid for non-ionic surfactants and that the influence of electrolytes on ionic surfactants differs in many aspects [32].

Quantitative data on the effect of electrolyte concentration on β - $C_{12}G_2$ -solution was published by Zhang et al. [49]. A chosen surfactant concentration of 0.4 mM and a salt concentration of 0.2 M are well in the saturated regime where the surface tension is constant at approximately $\sigma_s \approx 35 \frac{\text{mN}}{\text{m}}$.

2.2.5. Marginal Regeneration

One of the first drainage classifications of thin aqueous films was introduced by Mysels [26]. He distinguishes between rigid films that do not show any instabilities during the thinning process and mobile films which thin faster due to turbulent motion at the margins of the film. Two special cases of the mobile films discussed by Mysels are relevant for this study. Irregular mobile films generate instable domains of black film inside the thick colored film that break the layered structure of the film and allow rapid thinning. Secondly, he describes a class of films which develop a negligible amount of "streamers of black film" and therefore do not show an accelerated thinning behavior. The critical phenomenon that leads to rapid thinning is the surrounding of a domain of thick film with black film. Due to gravity this patch of thick film will be accelerated downwards thereby leaving a trace of thin black film behind. When a critical velocity and size is reached the thick element will not coalesce with the surrounding thick film and continues to be surrounded by a precursor of black film. The blob continues to sink and will reach the bottom margin of the frame where black film is continuously produced and expedited upwards as it is much lighter than the surrounding thick film. In that way, additional channels of black film are created which will lead to a destabilization of the thick colored film that will rapidly collapse and transform into black film. This phenomenon will be discussed in detail in section 7.2.2 in conjunction with experimental results.

In a rigid film the thinning is governed by Poiseuille flow as the two surfactant sheets form immobile walls so that the liquid core is restricted to gravitationally driven laminar flow with a parabolic velocity profile. Generally, this thinning mechanism is about three orders of magnitude slower [6] compared to the mechanism described above as the rigid area impeding the flow is a lot larger compared to the volume of the aqueous core (i.e. $V = 3\text{ }\mu\text{L}$, $A = 10\text{ cm}^2$).

A surfactant layer is considered mobile when no rigid monolayer is formed, the surfactants can move freely and whole elements of the film can be rearranged. In these films the governing process of thinning is marginal regeneration [26]. Regions of thinner film are formed at the borders of the film which are then transported into the film due to gravitational buoyancy or other mechanisms described below. The generation of thin patches at the borders was experimentally verified and quantified by V. Nierstrasz and G. Frens [27].

Laplace pressure gradient The first theory to explain marginal regeneration was published by K.J. Mysels [26]. He suggests that the primary reason for this effect is a border geometry induced pressure drop. At the contact of frame and liquid a meniscus forms with increased surface curvature with a concave outward orientation resulting in a pressure that is reduced relative to the outer atmospheric pressure. This negative pressure acts upon the cross section of the film and results in a force which is proportional to the thickness of the lamella. Therefore, thick parts of the film will be transported towards and thinner regions away from the border. This motion results in the generation of thin film and vanishing of thick film.

Initial differences in film thickness are expected to exist due to thermal fluctuations. The process is mainly opposed by the friction of the core liquid between the surfactant sheets as it is squeezed out. Therefore, rapid motion will generate thicker elements which in return reduce the net driving force. Film that is created more slowly thins more effectively by the suction of the border pressure gradient increasing the driving force. These two effects balance each other and for a given film thickness the velocity of the film moving away from the border remains constant. This also falls in line with Mysels experimental observations. The thinning velocity is also inversely proportional to the frame width indicating that the thinning is mainly controlled by the vertical borders. At any time, no visual sign of the marginal regeneration process is present at the top horizontal border and the exchange effects at the bottom do not seem to contribute to the thinning which is in contrast to Mysels model [42].

Static pressure equilibrium In the context of marginal regeneration it is vital to discuss by which means the weight of the film is supported. The weight of the liquid is not compensated by a decrease of hydrostatic pressure with increasing height as the surface curvature is approximately zero. Thus the pressure inside the film is equal to the external atmospheric pressure and the only option to support the film is an increase in surface tension σ .

$$\frac{d\sigma}{dz} = \frac{\rho g d}{2} \quad (2.6)$$

The surface tension gradient $d\sigma/dz$ is parallel to the z-axis pointing upwards. As the film has two surfaces only one half of the pressure needs to be balanced by one surface.

Surface tension at the film border At the frame - film border the pressure does change with height as the surface curvature decreases. Experimental values published by H.N. Stein [42] indicate a surface tension gradient $d\sigma/dz$ of $5 \cdot 10^{-4} \frac{N/m}{m}$ to $5 \cdot 10^{-3} \frac{N/m}{m}$ for films ranging from 0.1 - 1 μm in thickness.

Furthermore, Stein suggests that the liquid is transported upwards in the film near region of the border and downwards in the thicker streams directly at the frame as depicted in figure 2.2. The proposed scale of the thick stream is around 250 μm in diameter which is below the optical resolution limit of the setup presented (see section 4.2) hence cannot be verified at this point. The upward movement will continue until a pressure equilibrium is reached or friction stops the process. If friction at the border and at the interface of

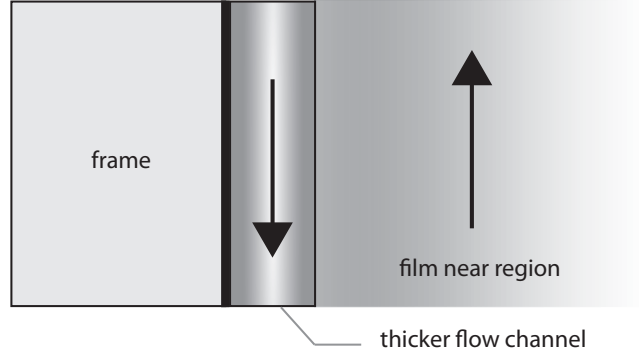


Figure 2.2.: Flow scheme proposed by Stein. The arrows indicate the general direction of fluid movement.

the two liquid streams moving in opposite direction is omitted one expects the upwards velocity to decay to zero when the following equilibrium is reached:

$$\frac{d\Delta p}{dz} \cdot d_{border} \cdot dx = 2 \cdot \left(\frac{d\sigma}{dz} \right)_{border} dx \quad (2.7)$$

Δp : deviation from hydrostatic equilibrium pressure ($\rho g d$)

The experiments and calculations by H.N. Stein result in an upward movement of domains in the film near border area until the border to film thickness ratio reaches a value of 3 [42]. The liquid in the top section of the film is directed towards the frame as the surface tension gradient prevents a downward flow along the film surface. The discrepancy to Mysels model concerning the lack of visible turbulence at the top border can be explained by the expected surface tension decrease in the downwards direction. Therefore, liquid flowing from the border into the film would create a flow acting against the principle of Marangoni flow and is not observable. However, a flow from the bottom margin into the liquid follows the positive surface tension gradient resulting in a regular Marangoni flow. As the height of the frame is the single parameter influencing the thinning velocity it must be concluded that this process does not influence the thinning rate. H.N. Stein argues that the elements of higher surface tension expand in area far away from the border inside the film and thereby just create local thickness deviations which do not contribute towards the global fluid transport [42].

surfactant concentration effects Another argument concerning marginal regeneration is given by Nierstrasz [27]. His work focuses on the effect of the surface tension gradient created by the stretching and compression of film elements. The surface tension σ_s of the film is mainly controlled by the surfactant concentration c_s . In general the surface tension decreases with increasing surfactant concentration until the saturation point is reached. Although Nierstrasz focuses on the marginal regeneration at the lower boundary of the film, the presented theory applies to the vertical borders as well when omitting the influence of gravity. When a film element merges into the plateau border its thickness is increased and the surface area shrinks [28]. Effectively it is compressed along an axis parallel to the film and perpendicular to the border. The compressed surface is

still covered with the same amount of surfactant molecules leading to a non equilibrium surfactant concentration. A possible mechanism to balance this effect is the diffusion into the core liquid leading to the formation of additional micelles if the used solution is already above the CMC. The amount of core liquid to absorb additional surfactants is relatively small so that the concentration would have to increase several orders of magnitude to reach the equilibrium surface concentration. and thereby is a very slow mechanism [28].

It is suggested that the saturated surface layer possesses an instability and separates into periodic areas of higher and lower surface concentration. The elements of lower surface tension will then expand thereby stretching the film and decreasing their density. This leads to an upward directed gravitational drift back into the film. This process is brought to a halt when the element of lower surface tension is surrounded by film of the same thickness and surface tension.

Mysels argues that these effects are mainly controlled by the type of surfactant and its concentration. At its core this argument is valid though recent investigations and experiments presented in this study suggest that the formation of thinning instabilities can be forced in stable films by creating non-equilibrium states induced by rapid motion.

2.2.6. Capillary Pressure

The capillary pressure P_c is relevant whenever a curved surface is present. In this study this is only relevant at the margins of the frame and at the interface of black film and colored film. The curved interface between air and liquid induces an increased pressure in the liquid film relative to the outer atmospheric pressure. The capillary pressure is also dependent on the wetting of the involved media and the resulting wetting angle θ .

$$P_C = \frac{2\sigma \cdot \cos\theta}{r_C} \quad (2.8)$$

r_C : radius of the curved liquid surface.

2.2.7. Surface Viscosity and Surface Elasticity

Due to the very small thickness of the film viscous friction in the film plane is not only determined by the bulk viscosity but also by the surface viscosity of the two surfactant sheets. The stability of foam films can not solely be attributed to the disjoining pressure and the surface charge density which act perpendicular to the film surface. The major in-plane properties of the film are surface viscosity and surface elasticity. The balance between disjoining pressure and surface tension does not necessarily yield a stable film, as was proven for non-ionic surfactants by Stubenrauch [35]. It is hypothesized that surface viscosity and elasticity of the mono layer allow the film to have dampening mechanisms to compensate distortions in plane with the liquid layer that would otherwise lead to rupture of the film. Surface elasticity measurements are usually performed in dependence on frequency of stretching and compression [44].

2.3. Thickness Profiling Methods

The research concerned with the analysis of thin liquid films employs various experimental techniques to examine the physical and chemical properties of ultra thin liquid layers. This section will give a brief overview of the optical methods relevant to this study.

Neutron Reflectometry Neutron reflectometry is an established technique to study thin films and interfaces. An advantage of the use of neutrons over visible light is the simple relation of the refractive index to density and composition of the material and can measure thicknesses in the range of $5 - 200 \text{ nm}$ [12].

A collimated beam of neutrons is directed onto a flat surface and the intensity of the reflection is measured with respect to the angle of incidence or neutron wavelength. It is possible to extract information about the surface structure, thickness and density of a thin film. The reflected intensity is described in terms of a scattering vector q_z :

$$q_z = \frac{4\pi}{\lambda} \sin(\theta) \quad (2.9)$$

λ : neutron wavelength (typically $2 - 10 \text{ \AA}$). θ : angle of incidence.

An advantage over visible light or x-ray spectroscopy is that it probes nuclear contrast instead of electron density. Therefore, it is sensitive to isotopic substitution which makes it possible to focus on i.e. deuterium labeled features of the film.

However, this method intrinsically delivers point-like data as it is a specular reflection technique that averages over the beam diameter and cannot image the area profile of the liquid layer. Furthermore, a neutron source requires a relatively high maintenance and costly infrastructure.

Fabry-Pérot Interferometry A Fabry-Pérot Interferometer is made of two parallel reflective surfaces with a transparent core. The distance between the two surfaces influences the transmission spectrum. When the incident wavelength is in resonance with the interferometer and the internal reflections lead to constructive interference, the transmitted intensity is maximized.

A liquid thin film is intrinsically an interferometer with varying distance between the reflecting surfaces. In practice a spatially coherent beam would be necessary to avoid ring like structures which appear due to a changing angle of incidence. A Fabry-Pérot interferometer requires a high reflectivity of the surfaces to yield a high finesse factor $F = \frac{\Delta\lambda}{\delta\lambda}$ which is a measure of the contrast of the resulting image. This is difficult to achieve in foam films.

Shadowgraph Imaging Shadowgraph imaging is used to reveal changes in density exploiting a change in refractive index. It is widely used in the study of explosions or air turbulence in the presence of a heat source. Shockwaves and the mixture of hot and cold air alter the density of air leading to different refractive indices. These differences can be made visible by illumination with a parallel light source and casting a shadow on a screen. The light intensity is proportional to the second spatial derivative of the refractive index ($I \propto \Delta n$).

Another variant of this method is Schlieren flow visualization which in addition to the shadowgraph setup features a knife edge in front of the camera blocking out the light that was not refracted in the interaction with the refractive index field. This is achieved by focusing the light beam to a single point after the interaction. Only the light rays that did not interact with the refractive index field will still be parallel and hit the knife edge placed at that position. This method yields a light intensity proportional to the first derivative of the refractive index ($I \propto \nabla n$).

In liquid thin film experiments the gradient map of the refractive index is given by the differences in thickness. Zhang et al. [48] successfully used this technique to visualize the turbulence in a soap film. However, with several micrometers the thickness of the film in their experiment was significantly larger delivering good contrast in the shadowgraph. Tests with the solution and thicknesses used in the presented setup which were conducted during a cooperation with the research group of Professor Xia at the Chinese University of Hong Kong revealed an insufficient contrast to apply this technique.

Visible Interference Patterns The diffused light is reflected by the front and back side of the film whereas the front reflection is shifted by π due to reflecting off an optically thicker medium. If the film thickness is much smaller than $\lambda/4$ of the smallest emitted wavelength the light waves interfere π out-of-phase and no light is reflected. Hence the name black film. The reason why there is no smooth transition in the intensity of the reflected light is the abrupt change in thickness when the common or Newton black film is formed (section 2.2.3).

At $\lambda/4$ of the smallest wavelength, which is around 112 nm in the case of the used full spectrum halogen bulb, the reflected waves interfere constructively. In addition, every other wavelength is reflected as well which sums up to a white color with a blue tint. Before the film is thinned to that thickness it exhibits an orange tint as the film is approximately 200 nm thick which corresponds to the amplification of red light and the cancellation of blue.

In general, it can be concluded that the visible color corresponds to the wavelength that interferes constructively at that particular thickness as every other wavelength is diminished in intensity. In thicker regions the pattern mainly alternates between a light pink and green hue as red and blue are reduced in intensity when green is amplified and vice versa. To get an absolute value of the thickness corresponding to a certain color displayed one needs to take into account that the refractive index of the solution is slightly higher than that of pure water.

2.4. Fluid Dynamics

Since this experiment is not only concerned with the static equilibrium state of thin liquid films it is necessary to take fluid dynamic regularities into account as well. The combination of surface forces and bulk fluid dynamics will be discussed briefly and follows the analysis published by R. Bruinsma [4].

The characteristic variables for this analysis are the film thickness $d(x, z, t)$ and the flow velocity of the surfactant sheet $\vec{V}(x, z, t)$. The film is parallel to the x-z plane and symmetric with regards to the y-axis. Small scale phenomena at the margin are omitted for the discussion in this chapter which makes it possible to set the surfactant area density γ to its constant equilibrium value. Consequently, the continuity equation $\frac{d\gamma}{dt} + \nabla \cdot \gamma \vec{V} = 0$ yields an incompressible surfactant flow field:

$$\nabla \cdot \vec{V}(x, z, t) = 0 \quad (2.10)$$

To complete the description of the surface flow it is necessary to state a second two-dimensional differential equation which is available in form of the Navier-Stokes-equation which will also be applied in the following description of the aqueous core.

$$\rho_{surf} (\partial_t \vec{V} + \vec{V} \cdot \nabla \vec{V}) = \eta_{surf} \Delta \vec{V} - \nabla \vec{p}_{surf} \quad (2.11)$$

Navier-Stokes-equation in two dimensions with the in-plane pressure \vec{p}_{surf} and density ρ_{surf} .

In addition to the two-dimensional surface motion it is necessary to define the flow of the aqueous core between the surfactant sheets. The hydrodynamic pressure inside the film $\vec{\Pi}(r, t)$ which is equivalent to the disjoining pressure balance discussed in section 2.2.2 accounts for the forces stabilizing the liquid thin film. Additionally, the thin film is under the influence of gravity and capillary forces which are subsumed in the external force $\vec{f} = \chi\sigma - \rho g z$. The Laplace pressure $\chi\sigma$ is only relevant in the border regions where the surface curvature χ is non-zero. The second part $\rho g z$ is the gravitational pressure. To account for the forced motion in the thin liquid film the aforementioned quantities are combined in the Navier-Stokes-equation with the convective acceleration $\vec{v} \cdot \nabla \vec{v}$ which is based on the advective operator $\vec{v} \cdot \nabla$:

$$\rho (\partial_t \vec{v} + \vec{v} \cdot \nabla \vec{v}) = \eta \Delta \vec{v} - \nabla \vec{\Pi} + \vec{f} \quad (2.12)$$

Navier-Stokes-equation

The term $\eta \Delta \vec{v}$ accounts for velocity scaled viscous effects and $\frac{d\vec{v}}{dt}$ is the unsteady acceleration. Following the lubrication theory for thin films as an approximation [29], inertia can be omitted and the flow treated as a Poisseuille flow (laminar, viscous and incompressible) between the two surfactant sheets placed at $y = \pm \frac{d}{2}$ with d being the total thickness along the y axis. The parabolic velocity profile is given by $\vec{v}(x, y, z, t) \approx \vec{V}(\vec{r}, t) - \frac{\nabla f}{2\eta} \left[y^2 - \frac{1}{2} d(\vec{r}, t)^2 \right]$. In combination with the Navier-Stokes-equation, this leads to a constituent equation for the surfactant layers in the form of a Stokes law in two dimensions:

$$\eta_{surf} \cdot \Delta \vec{V}(\vec{r}, t) = \nabla P_{surf}(\vec{r}, t) - \frac{1}{2} d(\vec{r}, t) \cdot \vec{f}(\vec{r}, t) \quad (2.13)$$

Please note that the differential operators in this equation only act along the surfaces of the thin film. Thereby $\Delta V(\vec{r}, t)$ is the flow density of the gradient of the surfactant flow and P_{surf} equals $2(\sigma_0 - \sigma)$ representing the surface pressure. By including the Poisseuille flow profile as an approximate solution for the Navier-Stokes-equation yields:

$$\frac{\partial d}{\partial t} + \vec{V} \cdot \nabla d + \nabla \cdot \left(\frac{d^3}{12\eta} \cdot f(\vec{r}, t) \right) = 0 \quad (2.14)$$

These four equations (2.10, 2.11, 2.12, 2.13 and 2.14) are a closed set of hydrodynamic equations for this simplified model of a vertically oriented soap films. A more detailed review on the coupling of surface and bulk via wall shear stress can be found in Oron's review [29].

3. Mixing and Theory

This chapter introduces the essential principles of ergodic theory and mixing that are necessary for the evaluation of the presented mixing and turbulence experiments. A thorough presentation of the theoretic background can be found in Sturman and Ottino's book covering "The Mathematical Foundations of Mixing" [45]. At first a description of orbits and their representation in the experiment is given. Subsequently, the Baker's transformation and Linear Twist Maps are introduced as appropriate tools to describe the mixing scenario. A detailed view on analytic tools to describe mixing behavior can be found in Ottino's "The kinematics of mixing: stretching, chaos, and transport" [30].

3.1. Basic Definition of Mixing

The presented research is only concerned with mixing in two dimensions so that the general measure is the *Lebesgue measure* μ which constitutes the term area in Euclidean space. Mixing is generally described by a mapping $f : A \rightarrow B$ which is bijective and therefore has an inverse f^{-1} that is one-to-one and onto. This criteria, however, is of more theoretical value as in the presented experiments the observation method cannot match a blob of fluid to its previous representation when its thickness changes. This means that the tracking of a single color includes a certain percentage of volume loss over time due to thickness change and merging with other fluid streams.

In this section however we consider all transformations to be well behaved including invertibility, measureability and differentiability. Furthermore, the Lebesgue measure will be preserved and finite.

The mapping f describes the geometric alteration of the initial conditions. This is essentially observable in the stretching and folding of the fluid. Omitting diffusion and break up of fluid segments deformation is the only possibility for the fluid to mix.

3.2. Fixed Points and Orbits

Flow structures which lead to stretching or folding of liquid filaments are often represented in terms of orbits. Elliptic periodic orbits are stable which means that particles form a closed loop after n applications of the transformation f . Furthermore, orbits in the vicinity remain close to the elliptic orbit. This is an unfavorable scheme for mixing as coherent regions develop which do not mix. Another type of periodic orbits are hyperbolic orbits which are instable. Nearby orbits will move away from these orbits although short term attraction is possible.

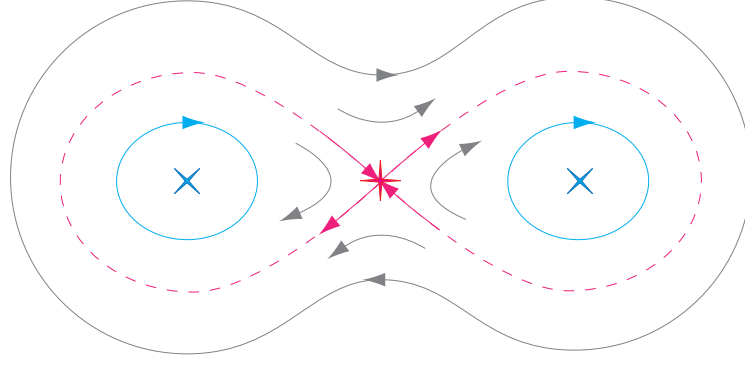


Figure 3.1.: Basic orbit scheme - blue: elliptic orbits and elliptic points; pink: hyperbolic orbit and hyperbolic points; gray: direction of fluid motion along and between the orbits.

Homoclinic orbits asymptotically approach the same hyperbolic orbit for forward and inverse advection cycles which means that there exists only one hyperbolic saddle point. Hereby, the direction of the advection cycle refers to the observation in positive (forward) or negative (inverse) time. Heteroclinic orbits, on the other hand, approach different hyperbolic orbits for positive and negative time.

Figure 3.1 displays the general outline of the hyperbolic cycle which contracts a blob of fluid in one direction and stretches it in another. The mixing is improved by feeding the outflow of the hyperbolic point (red star in figure 3.1) into the inflow. In the vicinity of the hyperbolic region the stretching is exponential. When a line segment passes by the hyperbolic point for each cycle the stretching may be combined so that the overall stretching for the segment is exponential [30].

If the flow is steady and isochoric the stream lines of a fluid filament join smoothly and are trapped between equipotential surfaces of the stream thus inhibiting good mixing. This is similar to a Couette flow which describes the laminar flow of a fluid between two shearing plates. However if the flow becomes unsteady and turbulent good mixing is possible as discussed later in this chapter.

The fluid transfer between the two convection rolls that develop below the cooling point can be characterized by a homoclinic orbit with the hyperbolic point at the bottom center of the convection as displayed in figure 3.2. Additionally, the centers of the convection rolls are defined by elliptic points to which nearby orbits converge. However, in the presented experiment an anomaly appears which causes a reverse drift of orbits into the outer homoclinic orbit. This instability is marked in figure 3.2 by the green hyperbolic orbit from which orbits in the vicinity move away. In principle this scheme is identical to the standard case of a connected hyperbolic orbit shown in figure 3.1 with the exception that the right cycle is mirrored at the horizontal axis of symmetry. This is not to be confused with two counterrotating elliptic orbits.

Although in principle the basic motion is comparable the confinement of the turbulence in the frame alters the fluid flow considerably. In a standard hyperbolic orbit the two flows joining head on in the hyperbolic point \vec{P} form a stable manifold W^s whereas the stream constantly moving away from \vec{P} forms unstable manifold W^u :

$$\begin{aligned} W^s(\vec{P}) &= \{\text{all } \vec{X} \in \mathbb{R}^2 \text{ such that } \vec{\Phi}_t(\vec{X}) \rightarrow \vec{P} \text{ as } t \rightarrow +\infty\} \\ W^u(\vec{P}) &= \{\text{all } \vec{X} \in \mathbb{R}^2 \text{ such that } \vec{\Phi}_t(\vec{X}) \rightarrow \vec{P} \text{ as } t \rightarrow -\infty\} \end{aligned} \quad (3.1)$$

stable and unstable manifold

A small blob of fluid at point \vec{P} is stretched in one direction and contracted in the other after one period when the point is hyperbolic. On the contrary, if the point is elliptic the application of one period would only result in a net rotation when \vec{P} returns to its original position. Further quantitative mixing analysis is presented in section 6.3.

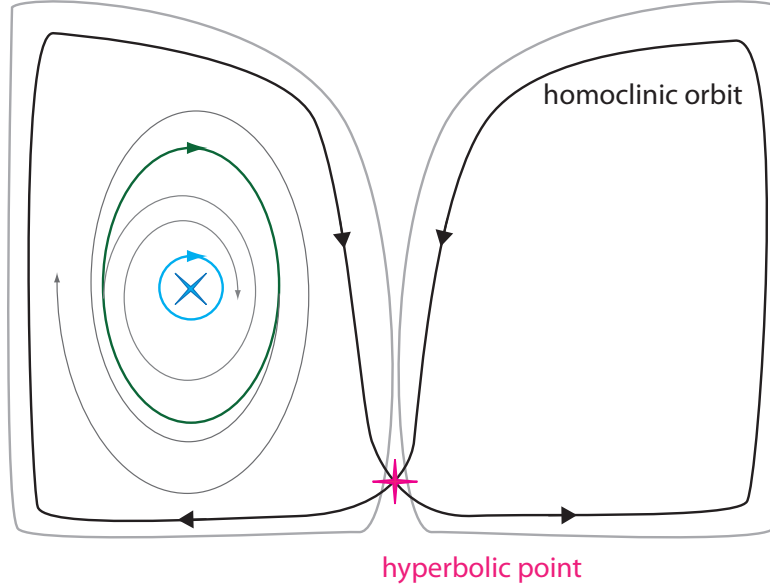


Figure 3.2.: Orbit schematic for the presented experiment. For reasons of simplicity, only the right half of the convection zone is shown in detail. The light gray outer line represents the shape of the two convection zones in the experiment. The gray traces represent orbits moving away or towards the center of convection. The elliptic orbits are marked with a light blue circle around the stationary elliptic point (blue cross) in the center of the convection zones. Green marks the limit between converging and diverging orbits.

Mixing is generally measured by the distribution of a marked fluid in a set domain. The initial conditions define a region of identifiable fluid (i.e. an ink drop surrounded by clear liquid). There exists an N so that for $n \geq N$ applications of the mapping f (or a time $t > T$) each subdomain becomes indistinguishable from any other subdomain. Taking a blob of ink in a clear liquid as an example this means that in every arbitrary area the same amount of ink can be found after n applications of f .

3.3. Baker's Transformation

In the following section a description of one of the more prominent mixing schemes is presented. The level of detail is motivated by the identification of similar patterns in the turbulent flow of the experiment and its significance in proving chaotic behavior.

The simplest proven way to achieve mixing in terms of the above definition in two dimensions without remaining unmixed islands is the Baker transformation (figure 3.3(a)). It is a volume preserving transformation consisting of two simple steps. In the first step, a square shaped domain of fluid is stretched in one direction with factor λ_1 (in this example $\lambda_1 = 2$) and in the other direction with factor λ_2 (in this example $\lambda_2 = 0.5$). In the second step, the stretched square is cut in half and stacked so that the original shape is restored. A flow is equivalent to the Baker's map when a homeomorphism (continuous function between the two topological spaces including an inverse) exists that transforms a region of the flow into a square resembling the Baker's transformation.

Nevertheless, in practical mixing experiments with continuous streamlines the process of the stacking is difficult to implement and is therefore usually accomplished by folding the stretched fluid back onto itself. Due to the non-zero curvature of the bend there will be a certain amount of fluid which will leave the original square and not be part of subsequent iterations as shown in figure 3.3(b). This concept is known as the Smale-Horseshoe-map which is the closest experimental approximation of a Baker's transformation. The volume loss in the presented experiment is given by the outflow of material at the bottom margin due to gravitationally driven thinning. Following Ottino [30, chapter 5.9] a system is chaotic when the flow has homoclinic and/or heteroclinic points or the flow produces horseshoe maps. Both criteria are fulfilled in the presented mixing scenario.

Folding happens at the top and bottom sections of the convection rolls where the fluid is decelerated. The fluid filament deforms and becomes thicker as material is not transported away fast enough and accumulates (figure 3.4/1). The faster incoming fluid is pressed into this formation thereby forming a horseshoe (figure 3.4/2-3). An example of the horseshoe development in the experiment is shown in figure 3.5. A quantitative description of the measured stretching and folding in the experiment is given in section 5.2.

Similarly, when the lower border of the blob is decelerated and the top border maintains a high velocity a somersault of the material forms. This is identical to the folding described above except that the continuing stream of fluid would be on top of the fold and not below. An example of a horseshoe forming under these conditions is displayed in figure 3.6.

Generally, this behavior is constrained to the outer rim of the convection rolls where the deformation is highest. A detailed review on the measured velocity and deformation fields is presented in section 5.2. The stretching happens mainly but not exclusively in the vertical part of the convection roll where the velocity and its gradient towards the border are maximized (marked blue in figure 3.4). These formations can be observed to a lesser extent closer to the core of the convection roll as the velocity gradient is slower and the overall motion more laminar.

These horseshoe formations have a creation period which is connected to the sequential fluid transfer discussed in section 6.3. Whereas in between these formations a laminar flow that just stretches the fluid filament may be observed.

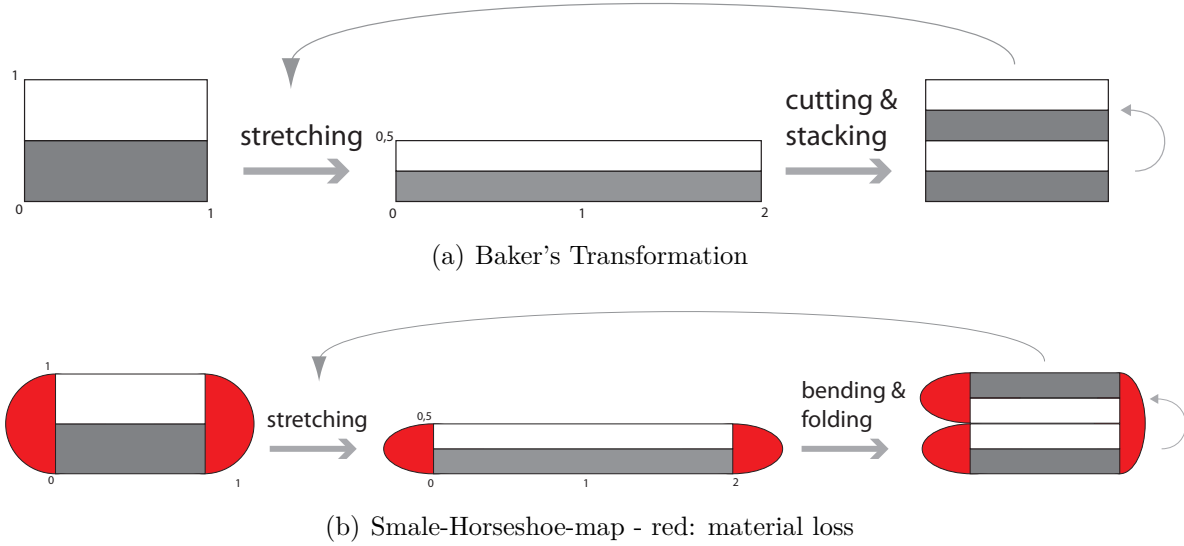


Figure 3.3.: Stepwise representation of a Baker's transformation and the simplest and most common case of a Smale-Horseshoe-Map

The loss of material defined by the Smale-Horseshoe-Map is not relevant for the mixing in this experiment as the horseshoe formation is not ideal and the folded fluid may be transformed by another horseshoe with different geometry or stretched until it is disconnected and forms two separate blobs. However, material is lost at the bottom margin due to the continuous outflow and at the upper border to the black film as newly generated black film is not part of the turbulent motion. Additionally the fluid stream is stacked after one full rotation back on itself resembling a second type of folding.

The mixing scenario is asymmetric with regard to the ratio of the area that are folded versus the total convected area. Only a relatively thin layer on the outer convection roll satisfies the conditions regarding the velocity gradient that allow folding. However, turbulent flow perturbations will lead to exchange of fluid between the core and outer region of the convection roll.

The identification of a Baker's transformation or an equivalent map is very important as it has been mathematically proven that the Baker's transformation has the Bernoulli property [45]. This means that it is identical to a random process more specifically chaotic mixing behavior.

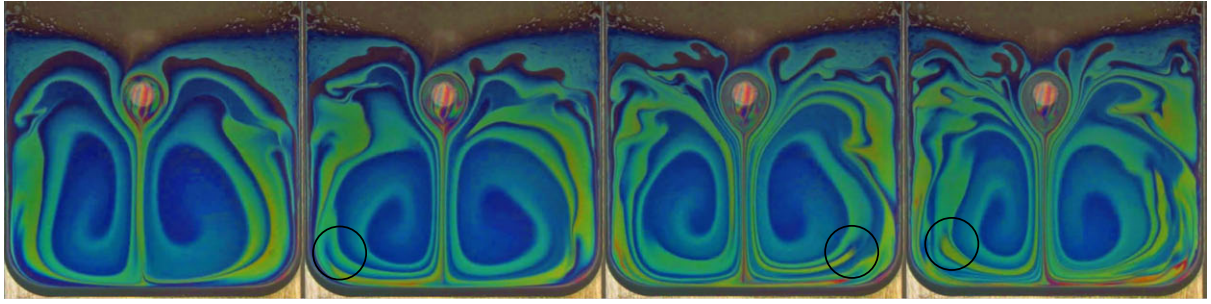


Figure 3.5.: Sequence of the captured turbulent motion. Each frame is set apart by 400ms. The circle marks the position of various horseshoes. Note that this is an early stage of the convection where the layering is still coarse.

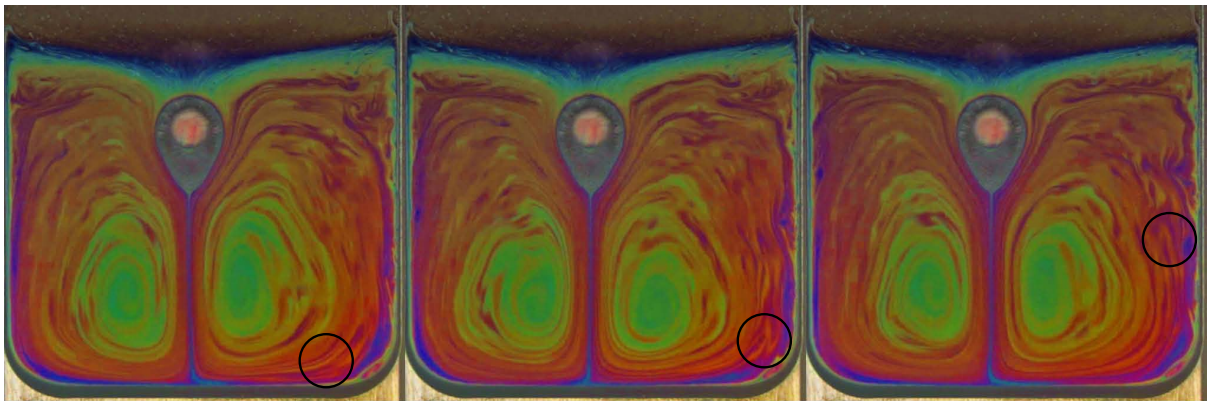


Figure 3.6.: Sequence of the captured turbulent motion at a later stage. Overall finer layered structures can be observed. Each frame is set apart by 400ms. The circle tracks the evolution of one particular horseshoe which is fully developed in the second frame.

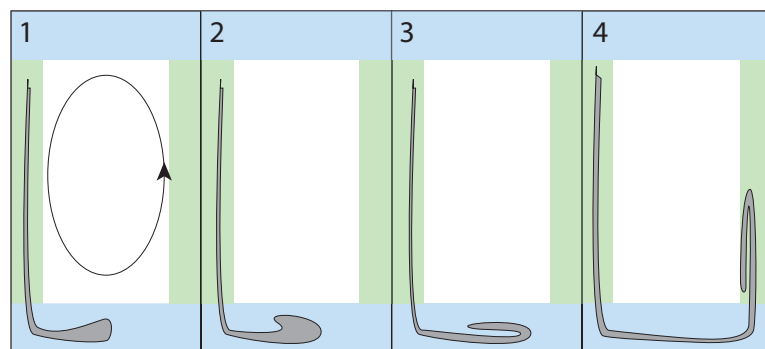


Figure 3.4.: Basic sequence of the development of a horseshoe in the flow field. Green marks the areas of stretching. Blue represents folding. Shown for the right convection roll (counter clockwise motion). The schematic is not to scale and exaggerates the horseshoe formation to illustrate the mechanism.

3.4. Linked Twist Maps

The analysis for the presented experiment is based on the fundamentals of mixing, which include the identification of the mixing scheme (i.e. tendril whirl flow or blinking vortex flow) and stationary points and orbits. Geometry wise, the soap film can be treated as a two-dimensional fluid with an area to thickness ratio of approximately $2 \cdot 10^4$. The current setup forces two counter-rotating annulars which are bounded by the rectangular frame. At the intersection of the two annuli the counter-rotating shear results in a co-twisting linked twist map [45]. The description of any mixer in terms of linked twist maps (LTM) gives a quantitative understanding of the efficiency and quality of its mixing properties. LTMs are simply defined by the composition of a uniform shear map and a twist map ($M_{LTM} = M_{shear} \circ M_{twist}$). For one annulus the twist map in angular coordinates can be written as

$$M_{LTM}(r, \theta) = (r, \theta + f_1(r)) \quad (3.2)$$

The annuli are centered at a certain distance l out of the center. It is therefore necessary to apply a transformation that shifts accordingly:

$$\begin{aligned} &\text{shift for left annulus :} \\ &T_1(r, \theta) = (r \cos \theta - 1, r \sin \theta) \\ &\text{shift for right annulus:} \\ &T_2(r, \theta) = (1 - r \cos \theta, -r \sin \theta) \end{aligned} \quad (3.3)$$

It is now possible to combine the two transformed twist maps to describe the system:

$$M = T_1 M_{LTM}^{(1)} T_1^{-1} \circ T_2 M_{LTM}^{(2)} T_2^{-1} \quad (3.4)$$

It is assumed that M is a bijection. Due to the nature of the experiment the fluid domains of varying thickness will diffuse to a certain extent and therefore are not volume-conserving. Nevertheless, the diffusion constant is considered to be small enough to be neglected. Applying this ergodic theory to the presented setup imposes the problem that the consecutive twist (i.e. blinking vortex flow) of the right and left annulus actually acts simultaneously. This circumstance is solved by discretization of the flow which will be discussed in section 6.4 where the presented LTM is applied to the experimentally observed convection. Further details on the application of linked twist maps can be found in [45].

In the generated velocity field, the fluid is stretched in regions of high velocity and compressed when it enters areas of lower velocity. Due to the shear, which is present between layers of different velocity, folding happens. These two processes are the main aspects of mixing in a two-dimensional fluid. Diffusion processes can be neglected as the Reynolds number is of the order of 10^3 .

4. Experiment

In the following sections the layout of the experiment will be introduced including the technical details concerning the chemistry of the solution and conduction of the experiment. The experimental setup was designed with regards to the optimization of the capture of the light reflection from the thin film to visualize the turbulent motion.

4.1. Setup

The measuring cell assembly consists of the following items:

- (1) Aluminum case with open bottom and top, viewing window in the front and several access holes
- (2) Top PTFE-block with a notch to hold the frame and a hole for the glass rod
- (3) Bottom PTFE-block with a cavity to hold the solution
- (4) Milled aluminum frame that holds the free standing liquid film
- (5) T-shaped glass rod
- PMMA protective screen taped onto the aluminum case

The assembled measuring cell and its parts are shown in figure 4.1. To create a liquid film, the glass rod is covered with solution by dipping it into the filled solution reservoir in the bottom PTFE block and then pulled upwards along the frame. This setup was developed at the Max-Planck-Institute for Colloids and Interfaces (MPI-KG) to study particle effects in macroscopic Newton black films and concentration dependent thinning behavior [41].

The aluminum casing was modified to allow the intake of the cooling rod through a hole in the back. Additionally, the inner faces which are in the field of view of the camera are covered with black cellular rubber to minimize reflections and enhance contrast in the video recording.

The setup is designed to generate an equilibrated atmosphere in the cell and enable multiple cycles of thin film generation without the necessity to open the cell.

To make the thin film visible it is illuminated with a diffuse light source at an angle of incidence of approximately 16° which yields the maximum intensity in the reflected light. Accordingly, the camera is placed at -16° with respect to the optical plummet perpendicular to the plane of the liquid layer. The complete setup in the laboratory is depicted in figure 4.2.

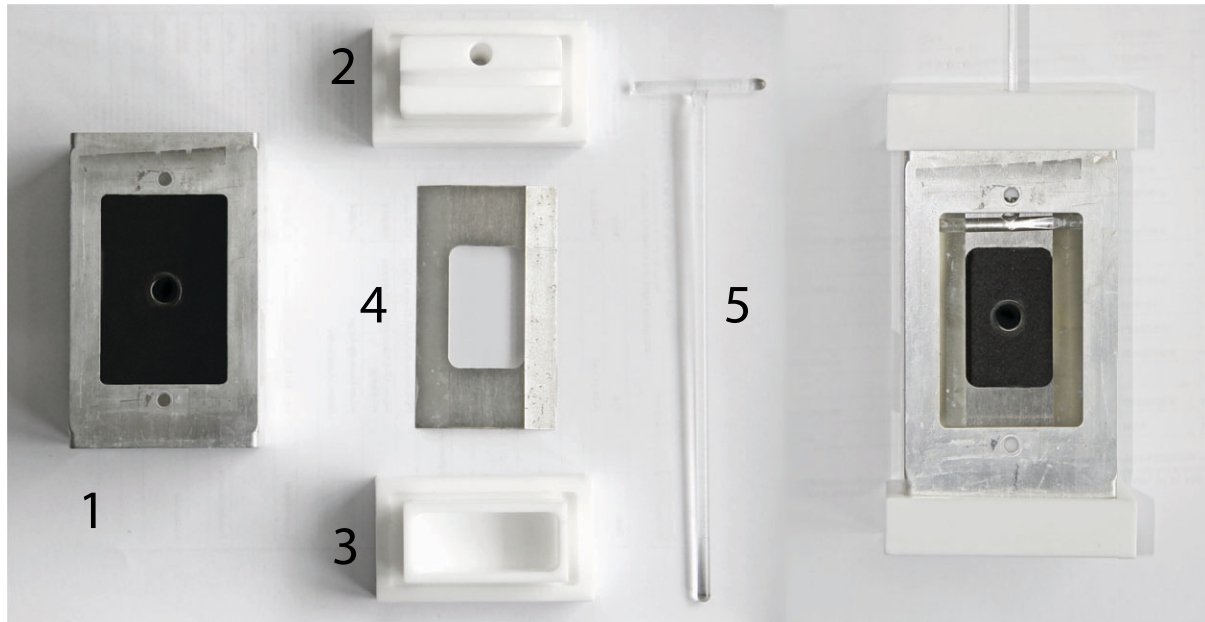


Figure 4.1.: The parts of the measurement cell is shown in the left. A front view of the assembled cell can be seen on the right side. The numbers correspond to the listed items on page 23.

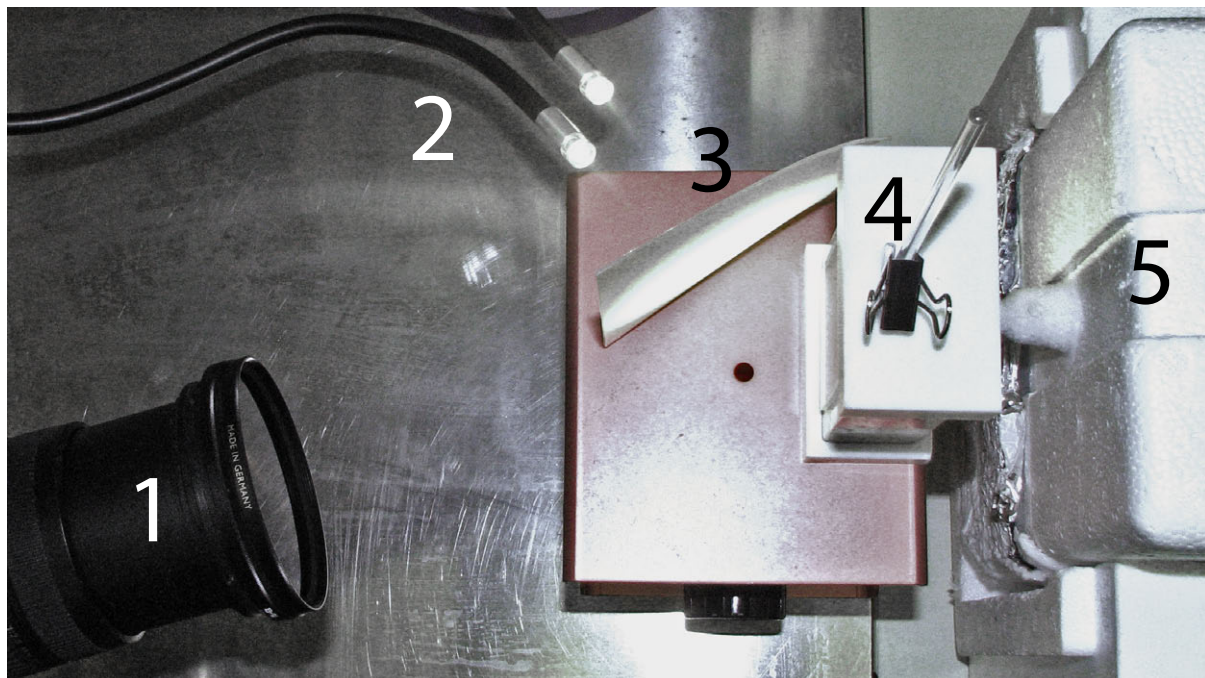


Figure 4.2.: Top view of the laboratory setup.

(1): video camera, (2): halogen lamp, (3): diffusor, (4): assembled measurement cell, (5): Cooling reservoir including the copper rod (covered in ice crystals)

The cooling rod is made of high purity electrolyte copper with a diameter of 8 mm and contains a PT-100 temperature sensor in its tip. To equip differently shaped cooling tips, the copper rod has a hollow opening at the front where the desired cooling tip can be inserted and fixed with two plastic screws. Mounting it on a massive copper pod makes the L-shaped rod less prone to overturning and serves as a cooling reservoir. The rod is placed in an isolated vessel which is filled with approximately 2 liters of liquid nitrogen which is able to keep the cooling rod at a constant temperature of -168°C for about 2 hours.

4.2. Limitations

4.2.1. Atmosphere

Due to the high surface versus volume ratio of the thin liquid film it is important to consider evaporation and its effects. The atmosphere in the measuring cell saturates with water vapor reaching maximum humidity thereby preventing any further evaporation from the solution chamber or the film. The necessary time to reach an equilibrium atmosphere is approximately 30 minutes [40]. Following the ideal gas equation the necessary volume that needs to be evaporated is readily calculated:

$$\begin{aligned}\rho_{\text{vapor}} &= \frac{e}{R_w \cdot T} = \frac{m_{\text{vapor}}}{V_{\text{cell}}} \\ V_{\text{water}} &= \frac{\rho_{\text{vapor}} \cdot V_{\text{cell}}}{\rho_{\text{water}}}\end{aligned}\tag{4.1}$$

ρ_{vapor} : absolute humidity; V_{water} : required volume to reach saturation

The saturated vapor pressure e can be calculated using the Antoine-equation which is derived from the Clausius-Clapeyron-Equation.

$$e = 10^{A - \frac{B}{C+T}} \text{ [mmHg]}\tag{4.2}$$

Antoine-equation

The fitting parameters for water in the temperature range of $273 - 303\text{ K}$ are $A = 5.40221$, $B = 1838.675$ and $C = -31.737$ yielding a value of $e = 2315.1\text{ Pa}$ [3] for the vapor pressure. A rough estimate with an assumed cell volume of 0.07 m^3 at standard temperature and pressure yields $V_{\text{water}} = 1,2\text{ ml}$. Considering that the total amount of solution in the vessel is around 5 ml relatively large evaporation losses and concentration changes need to be considered over longer periods of time. The composition of the solution will change as the vapor pressure of glycerin is about two orders of magnitude smaller than that of water. This results in a lower evaporation of glycerin compared to water at the same atmospheric conditions. The saturation vapor pressure is approached asymptotically so that even after a short period of time an adequate level of saturation can be reached. This has only been verified experimentally in a qualitative manner during

this study. Reaching an equilibrium state is also impeded by the minimal air exchange with the lab atmosphere through the necessary holes in the measuring cell.

Moving the cooling rod into the chamber immediately results in a thin cover of frozen liquid on the metal surface that limits the heat conduction to the film. The cooling winds falling downwards along the cooling rod will lower the average air temperature inside the cell. This has the positive side effect of lowering the amount of vapor necessary to saturate the atmosphere in the cell.

Dust As mentioned before it is crucial to keep the atmosphere free from any dust particles. They would create local perturbations in the film what in turn affects film stability. An indication for high contamination levels are visible dust particles. Due to the current mechanism of the film creation there is the possibility to carry dust that has settled on the glass rod into the measuring chamber. It is therefore advisable to limit the number of cycles of film creation before resetting the experiment.

4.2.2. Contrast of Video Data

The amount of reflected light is inherently dependent on the thickness of the liquid film. for thinner films this leads to a decrease in intensity which results in a lower contrast as undesired reflections from the background become more visible. Another factor is the reflection from the protective PMMA-screen: In addition to adding a constant intensity offset, it introduces slight color fringes due to its non-uniform thickness. These factors lead to a severely reduced contrast of the thin film reflection in comparison to the optimal situation without protective window and background and make contrast enhancing software filters necessary.

4.2.3. Crystallization

The sequence of snapshots in figure 4.3 shows a typical growth of the crystallization disc when the cooling rod is brought into contact with the liquid layer. Once the contact with the thin film is established the formation of a crystalline disc starts. This is depicted in the third frame at 80 *ms* in figure 4.3. The equilibrium diameter is reached within seconds. Despite the minor perturbations visible in figure 4.4 the influence of the crystallization disc around the copper rod is neglected in the analysis of the turbulence and mixing experiments. The freezing temperature of the used solution is approximately -7°C [5] not taking the influence of the surfactant into account due to its low concentration in the bulk media.

Despite the high temperature difference the crystallization disc only reaches a diameter in the order of one centimeter as the liquid layer is too thin and the heat flux from the atmosphere around it too large to support further crystallization. Even before the contact, the thickness of the liquid layer will increase which is evident by the color change from blue over green to red from the first to the second snapshot. Once in contact the formation of crystals starts with a radial symmetry which is perturbed due to turbulences. This results in an extension of the crystallized area in the downward direction and a

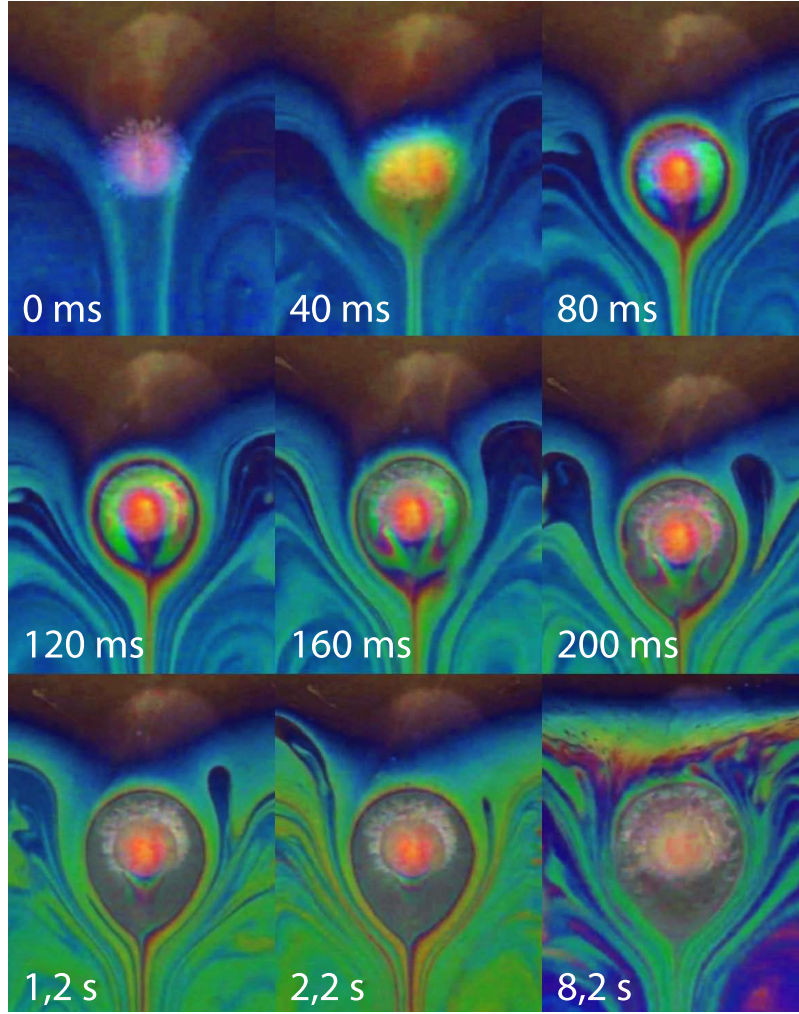


Figure 4.3.: Creation of the cooling disc. Sequence of snapshots of the cooling rod contacting the film. The time is given in absolute values.

delayed freezing of the area below the cooling tip. The ice disc continues to thicken evident by the changing color fringes until its equilibrium thickness is reached.

In general, the crystal growth is of dendritic nature. However, the fluid transport around the crystal results in a rounding off leading to a circular, smooth shape.

In terms of influence on the convection, the crystallized disc is another rigid to liquid phase interface that may produce marginal regeneration artifacts similar to the ones present at the aluminum frame. Such an artifact is shown in figure 4.4. The overall frequency of such a phenomenon is relatively small and does not influence the turbulence significantly. The color pattern of the perturbation visible in figure 4.4 suggests an influx of thicker material from the crystal to the liquid layer. It might be released due to a local thermal fluctuation that triggers the melting of the solution.

Around the crystallization disc flows a constant stream of liquid downward into the convection roll. The blob of black film which is transported through the convection roll and gets trapped at the bottom of the crystallization disc may be the origin of the perturbation. The presence of black film may locally accelerate the fluid flow and abruptly change the surface tension gradient around the crystallization disc leading to the

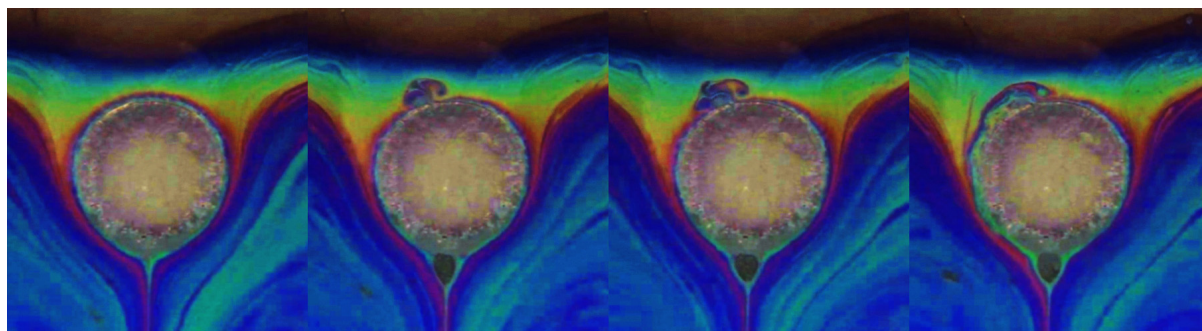


Figure 4.4.: Sequence of snapshots of a perturbation at the crystallization disc.

1. frame: initial unperturbed regime
 2. frame: turbulence after 0.48 s
 3. frame: turbulence after 0.64 s
 4. frame: fully developed outflow after 2.24s
- The perturbation vanishes after approximately 17 s.

visible burst of liquid. However, the temporal correlation of the two events might just be a coincidence. This phenomenon requires more detailed focus in separate experiments.

4.3. Solution Design and Measuring Procedure

solution design A few difficulties needed to be overcome in the process of generating chemical samples that meet the same qualitative standard as solutions prepared at the MPI-KG. It is crucial to minimize the influence of dust and weigh out every constituent very precisely. First attempts to recreate samples with the final concentration values failed due to the spread preparation over three sample preparing stations. Only the switch to a single lab station and the creation of samples from concentrated stem solutions made it possible to achieve stable nanoscale thin films.

Another obstacle was the unknown water quality available in the physics laboratory at the University of Potsdam. Conductivity measurements of sampled water performed at the chemistry department confirmed sufficiently low ion concentrations at a conductivity of $1.37 \mu\text{S}/\text{cm}$. The conductivity is therewith on the level compared to the purified water at the MPI-KG. However, non-conductive pollutants which could affect film stability were not determined.

It is advisable to add the crystalline raw materials to a sufficiently large amount of water to avoid high surfactant or ion concentrations. Otherwise, this might lead to increased micellar formation or unusual behavior of the surfactant.

In between preparation sessions the surfactant was stored at -18°C to prevent degradation. The samples were stored in air tight vessels at 6°C to minimize evaporation losses.

Due to the highly viscous glycerin portion, the prepared solutions were put on a shaker for several hours to ensure good mixing of water and glycerin. Shaking was stopped when a clear liquid without visible streaks or filaments of glycerin had evolved. Thereafter, the samples were put aside for at least 12 hours before use to allow equilibration. The

solution in the measuring chamber was left to equilibrate for ten minutes before each thin film creation as suggested in recent literature [41].

measuring procedure The first step involves filling the polystyrene vessel with liquid nitrogen and submerging the copper rod in it. In doing so, it is necessary to take into account that the wiring of the temperature sensor may not come into contact with liquid nitrogen as this can damage the insulation or brake the conductor.

Once the assembly of the cooling system is complete the temperature of the cooling rod is monitored via a digital temperature measuring device (Meilhaus Redlab TEMP). When the equilibrium temperature of -168°C is reached the cooling rod is ready to be contacted with the liquid film.

The measuring cell is assembled by clamping the aluminum frame and the glass rod to the top PTFE-cap and mounting it on the aluminum casing. After the viewing window is inserted and all unused access holes are sealed with tape, the bottom part can be filled with solution and merged with the remaining assembly. The only fact influencing the order of assembly is the desire to minimize solution evaporation.

When the solution is in the chamber and a timespan of at least 30 minutes has passed to allow sufficient saturation of the atmosphere, a liquid film can be generated.

4.4. Motion Capturing System

For the video captures presented in this work a professional video camera which was provided and operated by the Audio-Visual-Center of the University of Potsdam was used. It has a lateral resolution of 1200 pixel covering approximately 2.5 cm of the liquid film. This equals in approximately $25\text{ }\mu\text{m}/\text{pixel}$. As described in section 4.1, the camera needs to be mounted at an angle with respect to liquid thin film. This creates two problems: Firstly the plane of focus does not coincide with liquid layer which leads to out of focus areas. Secondly, the square film plane is distorted into a trapezoidal shape. The latter can easily be adjusted by video editing software. On the contrary, the blur cannot be reversed in post-processing. The amount of focus loss is dependent on the aperture of the video system and the size of the image sensor. However, the amount of light available limits the use of smaller apertures and the gain in depth of field at short focal distances is limited. In practice this effect limits the sharpness to an area which is approximately one half of the frame. To avoid this problem it is planned to change the camera system and implement a tilt-shift-lens which makes it possible to rotate the focus plane aligning it with the liquid layer and correcting geometric distortions.

4.4.1. Influence of Software Filters

The video processing in Adobe After Effects includes the application of a series of filters. The most prominent loss in the data processing is the intensity of each color. This is due to the equalization of light and dark areas to reach a uniform contrast and brightness over the whole film.

Another necessity is the correction of the color temperature offset of the camera to yield a neutral reproduction of the captured image.

Furthermore, the geometric distortion introduced by capturing the film at an angle of approximately 16° was corrected with a trapezoidal perspective transformation.

5. Convection

This chapter presents a quantitative characterization of the flow field in terms of the averaged local velocity and deformation profile of the liquid layer. The mixing behavior discussed in chapter 6 is based on the experimental data presented in this section. Techniques of manual and automated fluid blob tracking are presented and evaluated. Additionally, the contribution of friction coupling between the liquid layer and the air drag generated by cooling winds from the copper rod is reviewed.

5.1. Convection Velocity

definition of a cluster In the following sections a blob of fluid is denoted as a cluster - a term borrowed from the percolation theory. In this study a cluster is defined by a blob of fluid with homogeneous thickness that is different from the surrounding fluid. By recording the thin liquid film the continuous fluid blobs are discretized by the pixel grid. A connected area of identically colored pixels are then identified as one cluster.

velocity profile As a preparatory step to the automated cluster tracking algorithm presented in section 5.2, a single blob of fluid was tracked and its velocity determined with a motion tracking program (proAnalyst®). Although a more detailed view of the velocity field will be presented in section 5.2 it is important to analyze single streamlines as they can reveal effects of inertia. In figure 5.1 the velocity of a cluster is shown for two complete convection cycles. The maximal velocity in this example is about one order of magnitude smaller than the air velocity (section 5.3). This indicates relatively small skin friction or to be precise drag coefficient as expected for a flat sheet of liquid.

As depicted in figure 5.2 the cluster remains on an elliptic orbit in the right convection roll, not crossing the separatrix in its lifetime. The tracking of clusters with varying distance to the convection center revealed opposing converging behavior as described earlier in section 3.1. Clusters close to the center would on average shift to orbits closer to the stationary center whereas clusters with larger radii will tend to move away from the center of convection into the border area. The outward directed motion can partly be explained by the high friction and resulting shear close to the margin. The cluster is decelerated and material with a higher velocity is passing it on the inner side resulting in stretching and rotational motion. A similar process can be observed around the center of the convection where material transport towards the center leads to an increase in thickness. This effect is discussed in more detail in section 7.2.1. A cluster with higher density but equal velocity compared to the surrounding material is also likely to move further away from its original orbit due to its higher inertia.

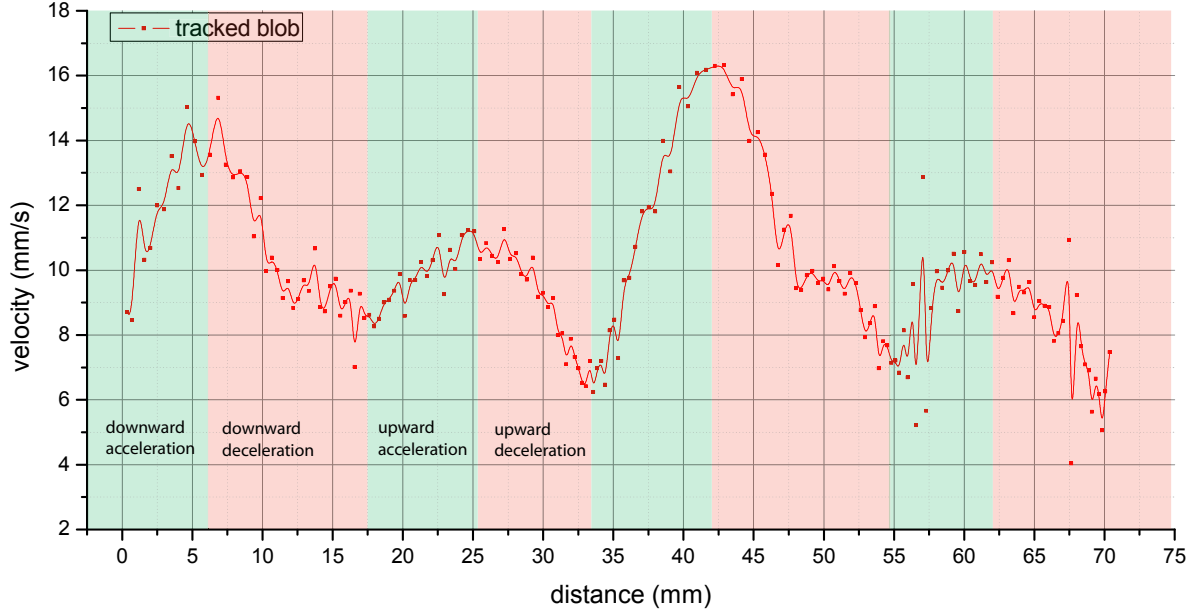


Figure 5.1.: Velocity profile of an advected cluster for two full rotations plotted over the total distance travelled by the blob.

In analyzing the velocity of the liquid layer it is also necessary to check the resolution-related capabilities of the video camera in use. Usually it is desired to oversample the fluid motion to avoid the loss of information about the fluid flow. In the current setup the camera delivers 25 frames per second with a spatial resolution of $25\mu\text{m}/\text{pixel}$. Assuming a maximum speed of $20\frac{\text{mm}}{\text{s}}$ any object is smeared out over the distance of approximately 30 pixels.

$$\Delta s = \left(20 \frac{\text{mm}}{\text{s}} \cdot \frac{1}{25} \text{s}\right) \cdot 40 \frac{\text{pixel}}{\text{mm}} = 32 \text{ pixel} \quad (5.1)$$

Fortunately this loss in spatial resolution only affects the areas of high velocity and overall smearing is usually less than 8 pixels for non-contact convection, where the cooling rod is placed at a distance behind the liquid layer. In contact convection experiments the velocity often exceeds 20 mm/s and smearing of up to 80 pixels might occur. The only option to increase spatial resolution while keeping the film at the same velocity is the increase of the frame rate of the camera. For the scope of this project the reliance on standard video capturing devices limits the available frame rate to a maximum of 25 frames per second.

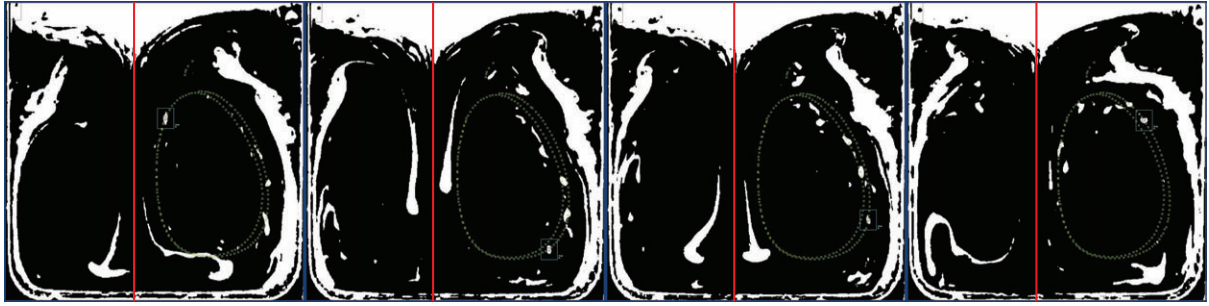


Figure 5.2.: Sequence of blob tracking snapshots done with the motion tracking software ProAnalyst. The tracked position of a single cluster is shown by the cyan bounding box for four different time steps. All tracked positions are marked in green. The boundary separating the two modes of the convection (separatrix) is marked by the red line.

5.2. Flow Field Characterization

In this section the deformation and velocity profiles of the turbulent motion in the liquid layer will be discussed. The analysis is based on a 2D cluster tracking algorithm named Cluster Imaging Velocimetry (CIV) which works similar to Particle Imaging Velocimetry (PIV). Its output are traces of fluid domains in the liquid layer with the same effective density. The terms stretch and compression in this section refer to changes in effective 2D density when the fluid thins or thickens. This does not imply an actual volume change of the liquid as it is still considered to be incompressible but an effective compressibility can be assigned due to the possibility to move in the third dimension.

5.2.1. Cluster Imaging Velocimetry

algorithm layout The identification of flow patterns relies on the identification of the velocity and deformation of a cluster which are ideally measured at every point of the flow. Thereby deformation is equivalent to the elongation and contraction of a domain of fluid with constant area that is moving along the trajectories of the velocity field.

This was accomplished by tracking areas of the same thickness. The data was converted to a black and white video: White accounts for a certain color representing a particular thickness and every deviation from that color is rendered black. To allow for fluctuations of the color value that was chosen, the filter was applied with a threshold that includes a narrow range of similar colors. The resulting video depicts clusters of nearly the same thickness following the trajectories of the flow field thereby changing their shape and speed.

This is taken as the input data for the cluster tracking algorithm. Following the concept of percolation the algorithm was designed to identify each cluster and track its movement and deformation over all frames.

A single cluster is located by finding a white pixel and subsequently checking all of its eight neighboring pixels whether they are white or black. Additional white pixels that are found belong to the same cluster. Once all neighbors have been checked, the global cluster number needs to be determined. This is straightforward for the first frame as all clusters

found are simply numbered consecutively. For the following frames it needs to be checked for each pixel of the cluster whether a white pixel at the same location in the previous frame does exist or not. One needs to pay particular attention to the case when clusters merge or separate as cluster numbers need to be omitted or newly assigned. Due to the nature of the experiment, there is always a big surrounding cluster present at the margins of the convection rolls which frequently absorbs clusters that are transported away from the convection center. It is therefore necessary to limit the temporal connectivity to one direction which means that once a cluster merges with another and may get a new index this index is not used to replace the index of the cluster in previous frames. If two clusters merge one of the indices will be discontinued.

Another aspect is the spatial range that is used to look for a cluster in the previous frame to find the index of the current frame. The algorithm only checks pixels that lie directly under the cluster in the current frame for the existence of a previous cluster. It was also tested whether a grid of varying size and spacing would increase the average time span of a cluster being tracked. The downside would be an increase in falsely detected cluster merges. For the majority of the subsequent analyses of the cluster data, only clusters which are larger than 30 pixels are used. This is due to their sufficiently long lifetime and robustness against noise introduced by the color identification.

A practical reason for the one-way tracking of the clusters is the convenience to hold only a couple of frames in the RAM of the computer to allow index changes at any time. Keeping several thousand frames in HD resolution to allow index changes at any time would exceed the available memory and prevent the execution of the program. The video frames are therefore read consecutively and discarded once they are processed. However, the algorithm is designed to store a variable number of memory frames to allow the search for connections in more than one previous frame which can improve the tracking of very small clusters which might not be visible for one or two frames due to noise introduced by the color code filtering.

The program stores just two frames at a time to check for the linkage of the clusters and then discards the last frame. After the cluster identification, a number of key quantities is calculated based on the information given by two consecutive frames:

- center of mass
- eigenvectors (principal components)
- eigenvalues (scaling of the principal components)
- lifetime in frames

This data is stored in a data object which contains an extensible list of subsets of variables that are calculated for each frame and cluster when needed. The current set contains entries for the following properties:

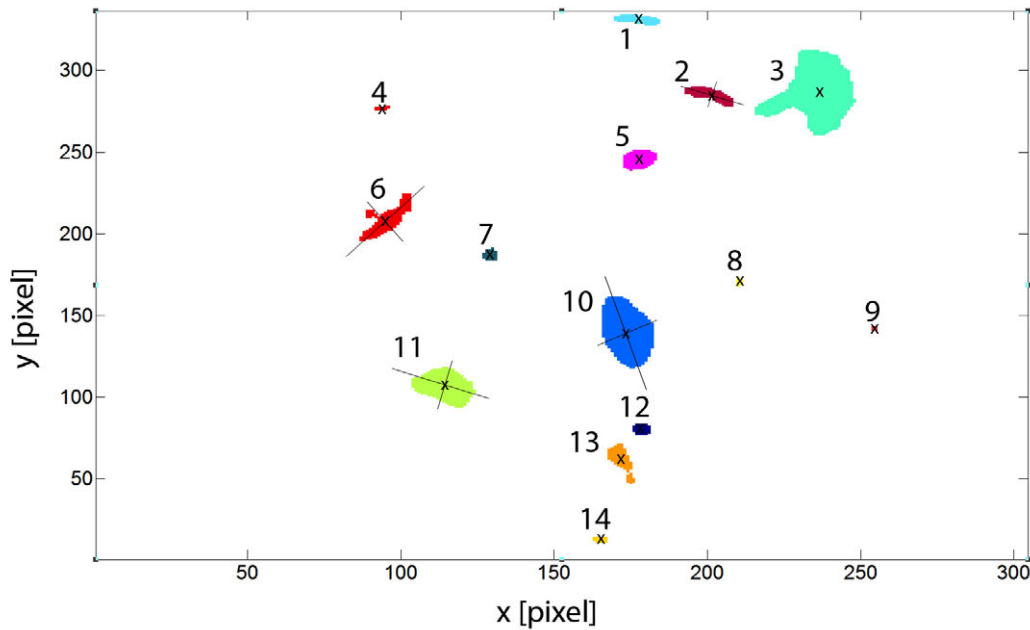


Figure 5.3.: Example of the cluster identification for one frame, including centers of mass (small x), unique cluster number and selected principle components (large crosses, not to scale).

cluster_nr	cluster number
start_frame	frame in which the cluster appeared first
end_frame	last frame in which the cluster was registered
size	number of pixels assigned to the cluster
positions	list of x- and y-coordinates of the pixels assigned to the cluster
com	x- and y-coordinates of the center of mass
eigval	eigenvalues of the two principal components
eigvec	eigenvectors of the two principal components
principal_components	scaled principal components
velocity	momentary velocity
angular_velocity	angular velocity (rotation eigenvectors)
deformation_rate	momentary change of the eigenvalues

Figure 5.3 illustrates the result of the cluster finding algorithm and the calculated centers of mass and principal axes. The data shown is a test set of a cropped region around the center of one convection roll.

deformation At this point a cluster is equivalent to a point cloud which makes it difficult to capture its deformation. Therefore the principal axis are calculated from the obtained eigenvectors and eigenvalues. Essentially, this reduces the shape of the cluster to an ellipse with a major and minor axis. The scaling of these axes are given by the eigenvalues which therefore constitute a measure of the cluster deformation.

At first the cluster finding algorithm was designed with a stack of neighboring pixels which was processed recursively till no more neighbors remained to be checked. Due to the speed limitations of the implementation in MATLAB, this part of the program was replaced by the MATLAB function `bwlabel` for each frame. This function essentially yields the same result identifying all clusters in a single frame. However, due to the call of optimized C-functions the execution is faster and consumes less memory compared to the algorithm written in MATLAB-code. The source code can be found in the appendix section A.1.

subsequent calculations Most of the calculations that are based on the cluster data rely on intelligent filtering of the data set as the original image contains noise resulting in many clusters with a size of 1 or 2 pixels. Additionally, these clusters usually last for only one or two frames which is inadequate to calculate the velocity at their location. Therefore these clusters are discarded. Clusters with long lifetimes and relatively small sizes are desirable for the generation of a velocity map as a limited volume decreases the absolute stretch of the cluster. Stretching may obscure the actual velocity information. A good limit for most of the captured data and the given resolution was a maximum of 3000 pixels which equals a feature size of 1.9 mm^2 .

The cluster finding algorithm is relatively robust against false identification of a found cluster. However, it is still possible that a link between two clusters in consecutive frames which do not belong to the same entity are falsely connected. Thereby causing a sudden jump of the center of mass and volume which produces spikes in the deformation and velocity field. It is therefore necessary to limit the velocity at least to the maximum velocity of the film determined in section 5.3.

After obtaining the filtered data set the desired values can be calculated and converted to SI-units as until now frames were used as the temporal unit and pixel as the spatial unit. In the following the velocity and deformation values are averaged over time with a spatial binning of one fifth of the original resolution. The binning is necessary because the velocity is connected to the center of mass of the cluster and it is unlikely to find multiple clusters with usable properties that will follow the exact same trajectory. The matrices of velocity and deformation vectors are then formatted into the VTK format to visualize the data in Paraview.

5.2.2. Velocity and Deformation Distribution

The cluster analysis yields results which usually are four-dimensional: Two dimensional spatial resolution, temporal resolution and the specific value at the point and time (i.e. center of mass, velocity). Therefore, it has been decided to export the data calculated in MATLAB to an external visualization tool. The Visualization ToolKit (VTK) is an open-source software package that can also be implemented in C++ or Python and was therefore chosen to allow exchange of the data between existing software environments. Another advantage is the simplicity of the data structure of the VTK-format which does not require complicated formatting and can be recreated efficiently in Matlab. The generated VTK files were imported in Paraview which is an open source visualization platform. The software was used to generate three-dimensional renderings of vector and scalar fields. A useful feature is the possibility to display various vector fields at the same

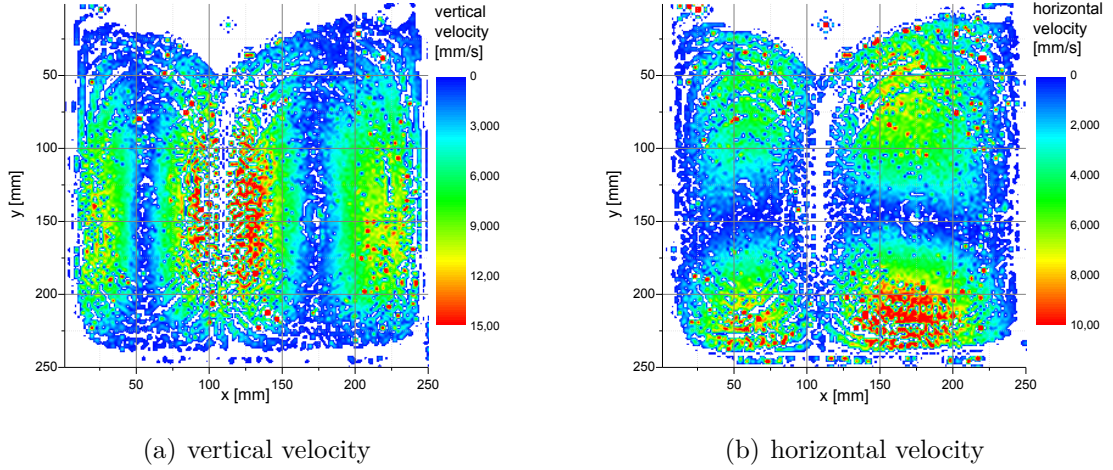


Figure 5.4.: Absolute velocity distribution. The position of the cooling rod is marked by the small star at the top. The area shown covers the whole convection zone

time which makes it possible to show both principal components, the center of mass and color-code the objects with velocity or deformation rate.

absolute values At first only the absolute values of velocity and deformation vectors will be taken into account to characterize the flow field. As it can be seen in figure 5.4(a) the vertical velocity maximizes in the center of the frame where the liquid is driven by the temperature gradient and cooling wind from the copper rod. As expected the upward convective motion at the outer sides of the convection roll is lower in absolute value compared to the inner directly driven fluid. A part of the kinetic energy is lost in friction at the border and deformation of the fluid. Furthermore, the redirection of the fluid flow at the bottom border lowers the velocity as the liquid is contracted and pushed to the side. Please note that figure 5.4(a) and figure 5.4(b) are at different scales and the velocity at the outer vertical border is greater than the horizontal velocity at the bottom.

The differing size of the left and right convection roll is due to the asymmetric placement of the cooling rod when contacted with the liquid layer. The high vertical velocity zone averages around 15 mm/s which coincides with the values extracted from the single blob tracking analysis in section 5.1.

The calculation of the cluster deformation is based on the difference between the eigenvalues of the corresponding principal component of two consecutive frames. These stretching rates are essential for the quantification of the mixing efficiency presented in section 6.4. The algorithm does not continuously track the same axis instead the assignment of minor and major axis may be commuted when the minor component exceeds the previous major component of the last frame. As a consequence most of the deformation information is contained in the plot of the major axis deformation (figure 5.5(a)) as the principal component with the largest dimension generally shows higher stretching rates. Nevertheless the deformation behavior is accurately depicted in the combination of the two graphs (5.5(a), 5.5(b)). The most evident information that can be extracted from the deformation graphs is that most of the clusters are subjected to major stretching in the outer high

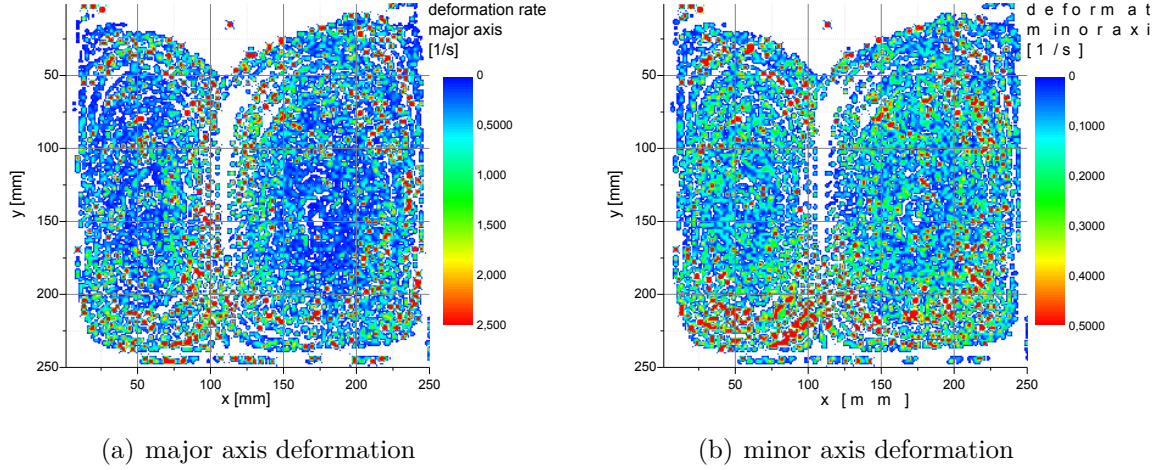


Figure 5.5.: Absolute deformation distribution in the thin film.

velocity orbits. The clusters accelerated downwards along the separatrix are stretched vertically (generally along their major axis) whereas an increase in the deformation rate of the minor axis at the bottom of the frame is congruent with the sideways direction change of the fluid. In comparison the minor component, extension is about one order of magnitude smaller than the vertical stretching. Similar to the velocity distribution the center of convection shows minimal stretching.

The deformation plots depict the absolute values of deformation omitting whether the cluster is stretched or contracted. A sign sensitive visualization does not reveal a distinct separation in areas of stretching or contraction because areas of high deformation contain negative and positive values in immediate vicinity.

vector data To complete the information about the deformation field, the average principal axis are shown in figure 5.6 and 5.7. The orientation of the clusters is congruent with the velocity field. Especially in the center region, the fluid is exposed to significant shearforce due to the large velocity gradient: The cluster is stretched which results in the orientation of the major principal component parallel to the velocity field.

The graph is scaled by the calculated principal component in pixels which is equivalent to one half of the actual dimension of the cluster. The maximum of the major component (23 pixel) translates to a total cluster length of 2 mm and equivalently for the minor component the maximum is 0.3 mm . The cumulation of larger minor principle components at the bottom side and center of the convection roll (5.7) indicates a round shape of the clusters when viewed in combination with figure 5.7 which shows major principal components of similar magnitude. At the bottom of the convection roll, the round shaped clusters can be explained by the lateral contraction of the fluid due to the decreased velocity at the sides when fluid is still forced downwards in the middle.

The most complete view of the convection is given by the averaged velocity field of the fully developed turbulent motion which clearly shows the trajectories that the fluid is following (figure 5.8). The maximum velocity of approximately 20 mm/s is reached in the center of the cell between the two convection rolls. Abrupt changes in the velocity

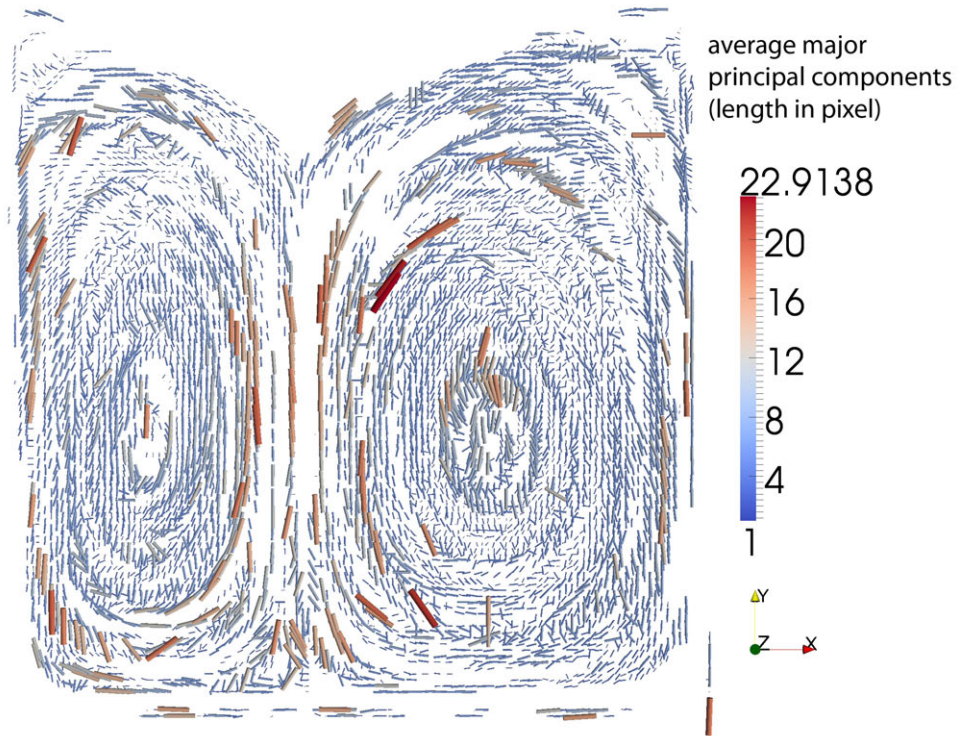


Figure 5.6.: Distribution and size of the major principal axis of the clusters in the turbulent field.

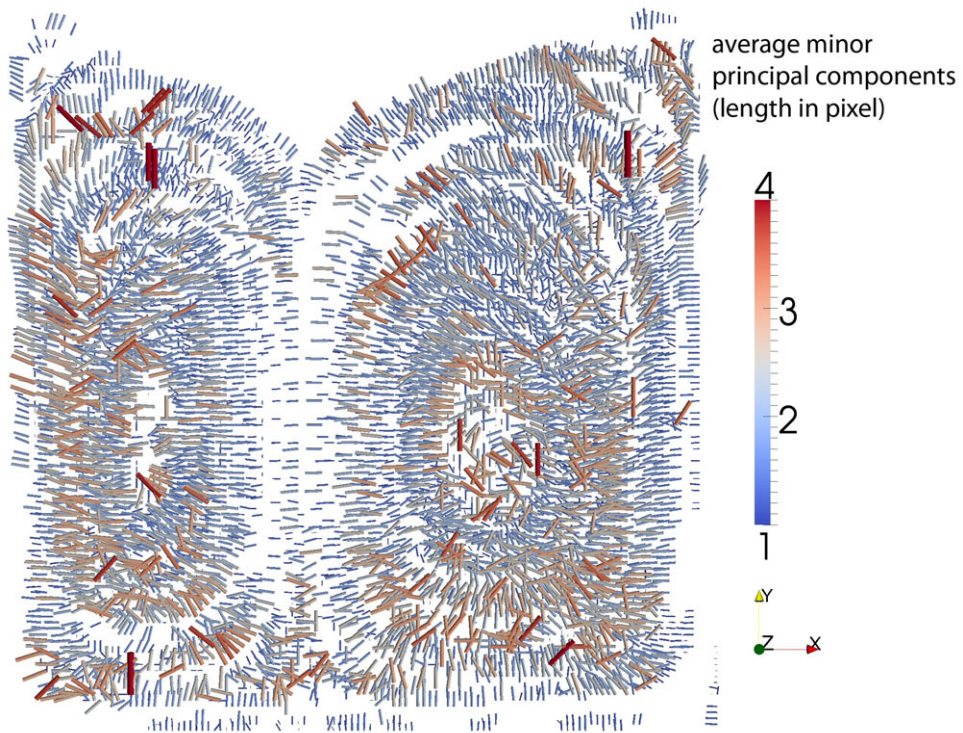


Figure 5.7.: Distribution and size of the minor principal components of the clusters in the turbulent field.

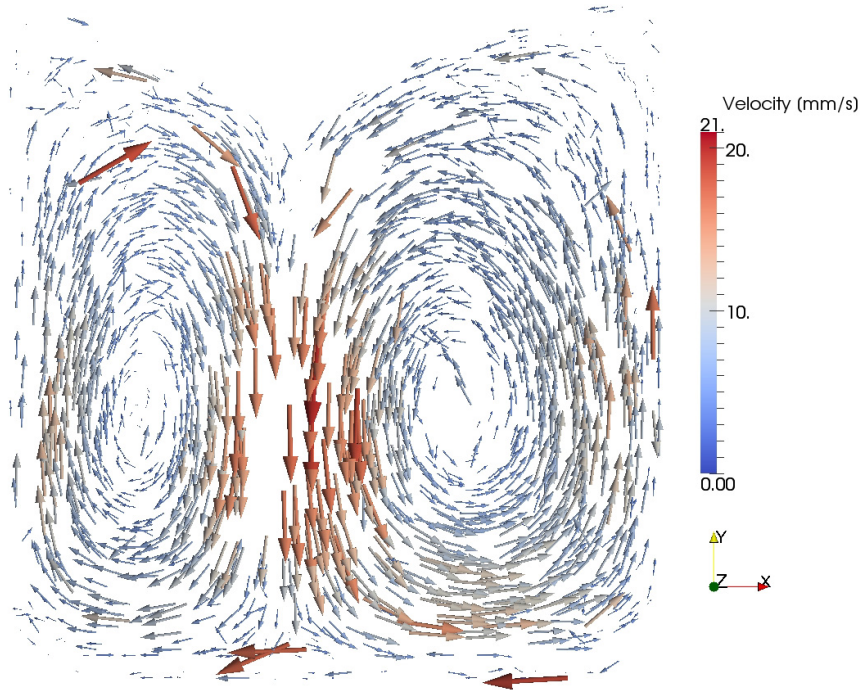


Figure 5.8.: Average velocity vector field. The vector glyphs are scaled and colored linearly according to the absolute value. The cooling rod is positioned at the top center. Capture duration was 1 *min*.

field or arrows opposing the average field direction are artifacts that have not been filtered out. Note that for the velocity field represented in figure 5.8 the cooling rod was not in contact with the film but positioned very close to the surface. This results in lower speeds of the convection. This video stream is captured at a resolution of 3,6 *k pixel* compared to later captures during the high speed in contact turbulence experiment with a resolution of 8,4 *k pixel*. Figure 5.9 presents the same velocity field for a liquid layer in contact with the cooling rod. The contact can be identified by the region without velocity vectors at the top center where the disc of crystallized solution is formed.

Although figure 5.9 is captured at higher resolution and shows more details of in the low velocity regions, the velocity field is less complete than its low speed counterpart figure 5.8. This is based on two technical difficulties. Firstly, the video post-processing of the raw material to acquire the black and white video feed for the cluster finding algorithm needs several adjustment steps for the base color which is then replaced with white. Due to the higher speed of the convection, the overall thickness changes faster and the color that is used to identify clusters will become the background color thereby inverting the black and white image. At this point, the color adjustment is done manually but it is desirable to automate this process. Secondly, to match the evolution of the turbulence shown in figure 5.9 to the previous analysis, only a quarter of the timespan was analyzed in comparison to the velocity field presented in figure 5.8 because the convection is about four times faster (compare velocities in figure 5.8 and 5.9).

The major drawback in the presented analysis is the limited frame rate. As presented in section 5.1, a high enough frame rate is needed to ensure the identification of a single

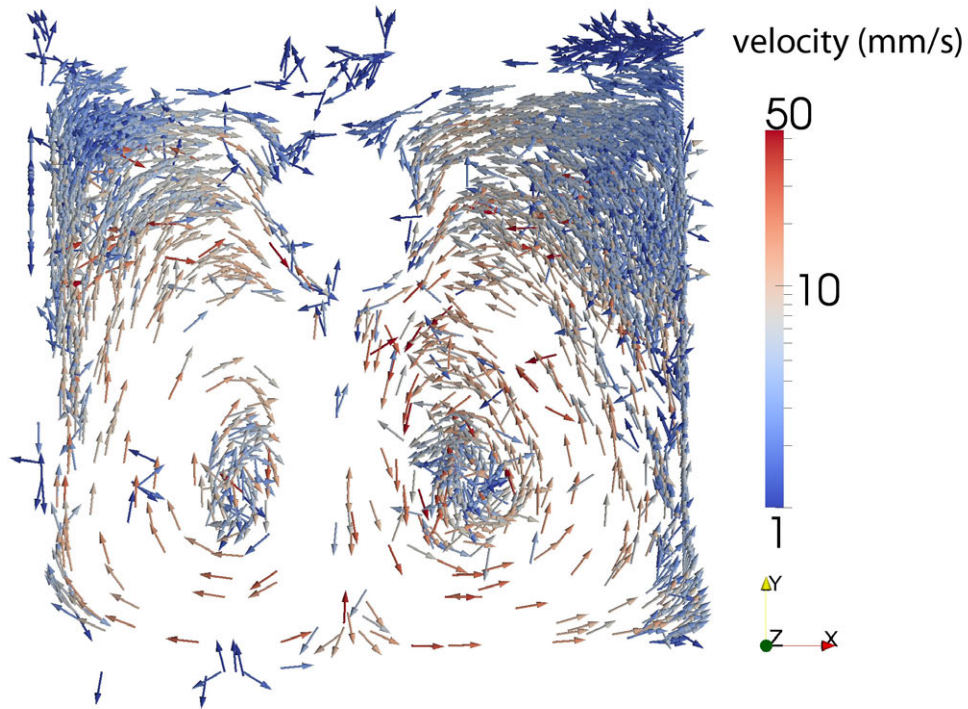


Figure 5.9.: High speed convection with the cooling rod in contact with the liquid film. Minimal cluster lifetime is **2** frames. Capture duration was 25 s.

cluster through multiple frames. When the fluid velocity is high enough to carry an arbitrary cluster a distance greater than its actual length in the timespan between two frames, the cluster finding algorithm is not able to link and treats the two representations of the same cluster as two different entities. However, for the calculation of the velocity the bare minimum is a cluster lifetime of two frames. Manual velocity calculations of clusters close to the center stream between the two convection rolls revealed values up to 70 mm/s . Figure 5.9 and 5.10 show the difference in displaying clusters with a minimum lifetime of two versus three frames. Most of the available information is based on clusters which can be tracked for only two frames. This can be overcome by increasing the frame rate or reducing the speed of the liquid film. The latter makes it necessary to lower the temperature gradient by increasing the temperature or distance of the cooling rod.

angular velocity The angular velocity of the clusters is given by the rotation of the principal components per frame. Figure 5.11 shows the averaged angular velocity for the slow speed measurement. The sampling rate for the in-contact measurement is too low to provide viable data. The angular velocity maximum differs from the velocity and deformation distribution and lies in an intermediate section between the high velocity surrounding and the slowly rotating stationary center of the convection rolls. This zone is identified by low stretching rates and average speeds which prohibit significant stretching of the cluster but enables them to rotate due to the velocity difference at the boundaries of this intermediate velocity zone. This representation of the turbulence field is affected by the exchange of minor and major principal axis at equal size mentioned earlier which generates spikes in the angular velocity field. It can therefore be viewed as a shape indicator for the clusters as unphysical high values of angular velocity indicate a frequent

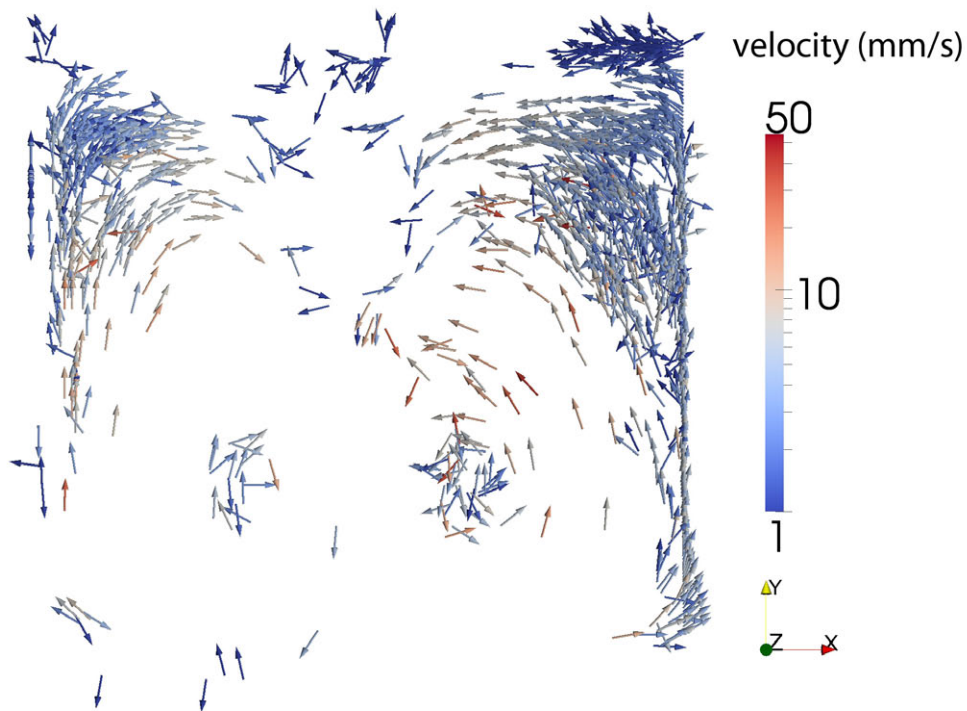


Figure 5.10.: High speed convection with cooling rod contact.

Minimal cluster lifetime: **3** frames. capture duration: 25 seconds.

switch of the principal components positions suggesting that mainly round clusters are present in these regions.

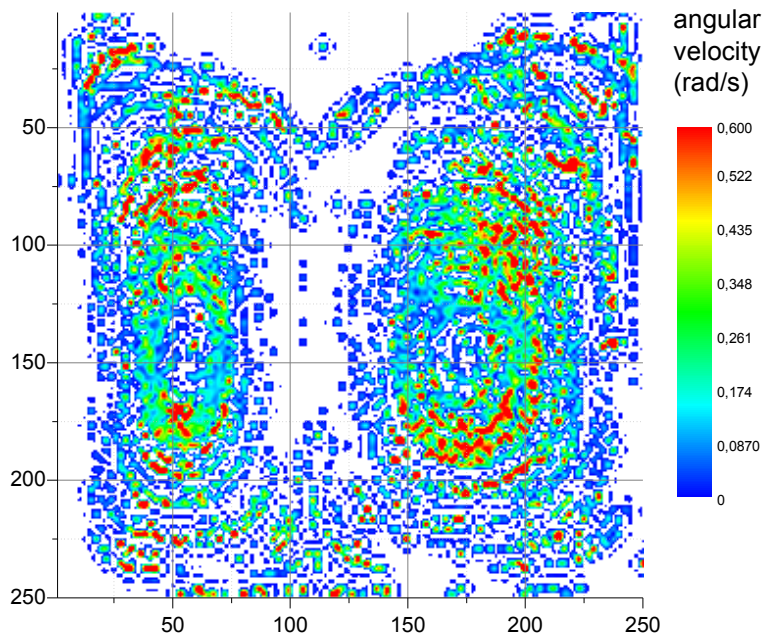


Figure 5.11.: Angular velocity distribution calculated on the basis of the low speed cluster analysis (figure 5.8).

5.3. Air Convection Velocity

The two major influences driving the thin film are the temperature gradient introduced by the cooling rod and the air convection at the back side of the film. Similar to the cold dense fluid falling downwards due to gravity in the film the cooled air develops an equivalent motion. Along the cooling rod the air increases in density and is accelerated downwards due to a temperature difference of the cooling rod and the surrounding atmosphere of approximately 180 K . It is therefore necessary to gauge the influence of the air convection on the fluid motion as they are coupled via surface friction.

At first, the maximum velocity of the air convection was measured. This was done by saturating the cell with water vapor and then introducing the cooling rod. The local vapor pressure is decreased due to the temperature drop and mist develops and is transported downwards. By illuminating the scene from the top and capturing the movement from the front side, the light reflected off the small water droplets was recorded.

The motion is captured with an SVSI highspeed camera at a resolution of 1.3 megapixel covering an area of roughly 1.5 cm^2 at a frame rate of 400 frames per second. The tracking of a small ice flake was implemented by the feature tracking algorithm available in the tracking software ProAnalyst. A track of the center, front and back end position were averaged to minimize effects of changing feature shape. The calculated velocity and acceleration of the particle are shown in figure 5.12. The distance scale represents the total distance traveled by the particle and can be regarded as a linear time scale.

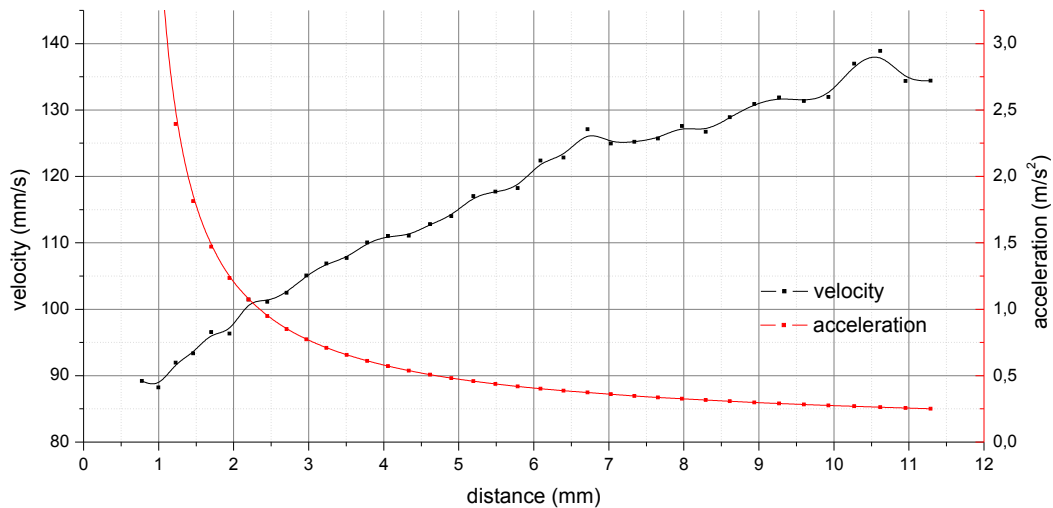


Figure 5.12.: Velocity (black) and acceleration (red) of a particle advected in the cooling jet directly beneath the cooling rod.

The velocity and acceleration profile are shown for a particle that departs from the copper rod and is accelerated into the region between the two convection rolls where the velocity reaches its maximum. It can confidently be deduced from the graph that the maximum velocity of the air convection is reached after traveling approximately 10 millimeters as

the acceleration is asymptotically approaching zero. The maximum velocity is about 140 mm/s .

For the correlation of the motion in the liquid layer and the air behind it one needs to take into account that the air convection has a slightly different geometric confinement. The downward airstream is deflected sideways by the surface of the solution reservoir which lies approximately 10 mm below the bottom margin of the liquid layer. The vertical borders are defined by the walls of the measuring cell which is approximately twice as wide as the fluid layer. Owing to the low inertia of air, the speed of the convection is vastly reduced in the outer parts of the convection far away from the driving cooling rod. This behavior could be deduced from accurate observation of the captured videos and has not been quantitatively analyzed. Therefore, It is feasible to neglect the influence of the airstream except for a thin jet of air which is directly located under the cooling rod.

6. Mixing

The presented turbulent motion is analyzed with classical mixing designs in mind to evaluate the behavior of this two-dimensional mixer and its mixing efficiency based on the theoretical aspects discussed in chapter 3. Fluid transport between the convection rolls, overall material transport and pattern formation are the key components presented in this section.

At first, a characterization in terms of pattern evolution is presented in section 6.1. This is followed by thoughts on folding and fluid transport. Conclusively, based on the deformation field (section 5.2) an overall mixing efficiency is calculated.

6.1. Spatial and Spectral Analysis

Spatial analysis The initial step towards the characterization of the mixing behavior is the time evolution of the spatial wavenumber. When the cooling rod is contacted with the liquid film and the turbulence develop thin material is carried downwards coiling around the centers of convection. Along a single horizontal line that intersects the centers of the two convection rolls the number of transitions from thick to thin material increases. This is effectively the spatial wavenumber in the image as the thickness is encoded by the color scheme. Figure 6.1 and 6.2 show the stringing together of the single lines taken out of a large number of frames. It is crucial to note that the example in figure 6.1 was captured without contact of the cooling rod and is therefore roughly six times slower in comparison to the convection shown in figure 6.2 which had contact. Another difference is the initial thickness of the samples. The direct contact convection was also done with a thinner film of a thickness ranging from 200 - 700 nm whereas the slow convecting film had a thickness of 500 - 1100 nm.

For further analysis only a single channel out of the three available color channels (red, green and blue) was chosen. The choice of channel is dependent on the degree of thinning the film has reached and the respective color when the turbulence is introduced.

The first insight into the mixing behavior is the temporal evolution of the variance of the intensity $\langle\langle I(x, t) \rangle\rangle$ (Figure 6.3). When the cooling rod is in place the variance increases instantly indicating distribution of the fluid away from its center of mass. The fluid is driven downwards and advected around to the side of the frame and thereby transported away from the mean value which is located in the center of the frame logically increasing the variance. Due to the continuous stretching of the filament like structures of fluid with varying thickness they will eventually merge into each other forming a domain of uniform thickness. At that point the variance will decrease again indicating the end of the mixing which is trackable by thickness variations. Of course the mixing by stretching and folding

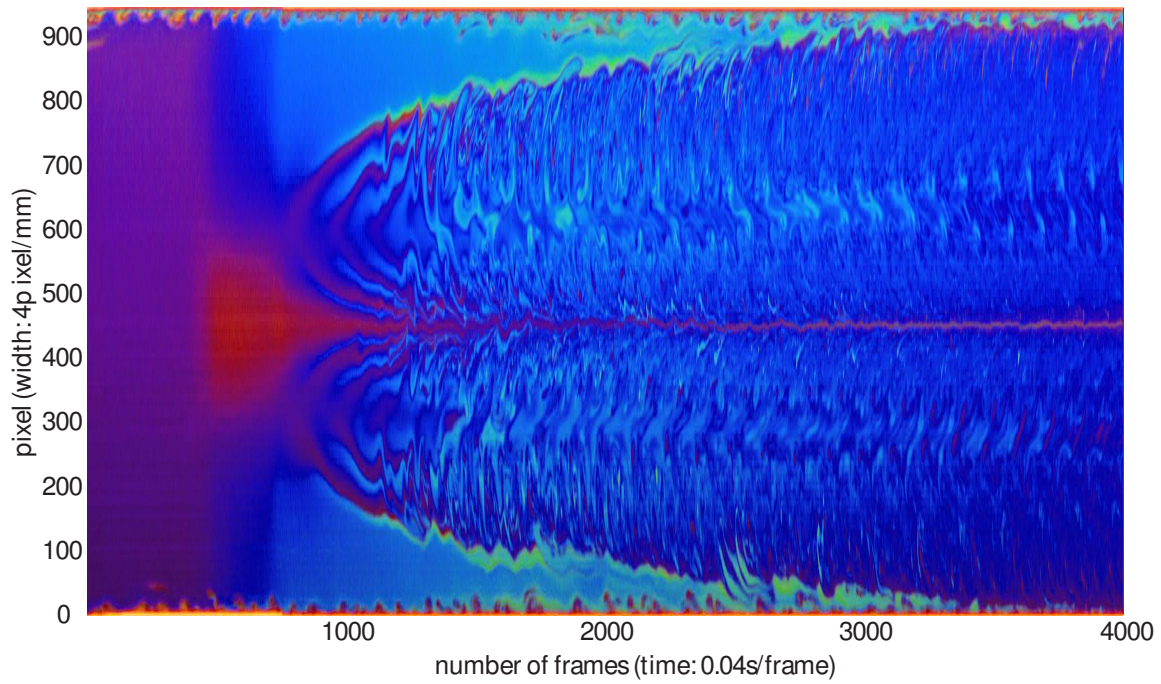


Figure 6.1.: Real color image of a one pixel wide horizontal line through the center of convection over time. The spatial extent is 25 mm . The convection is shown for a timespan of 160 seconds. Cooling rod is not in contact with the film.

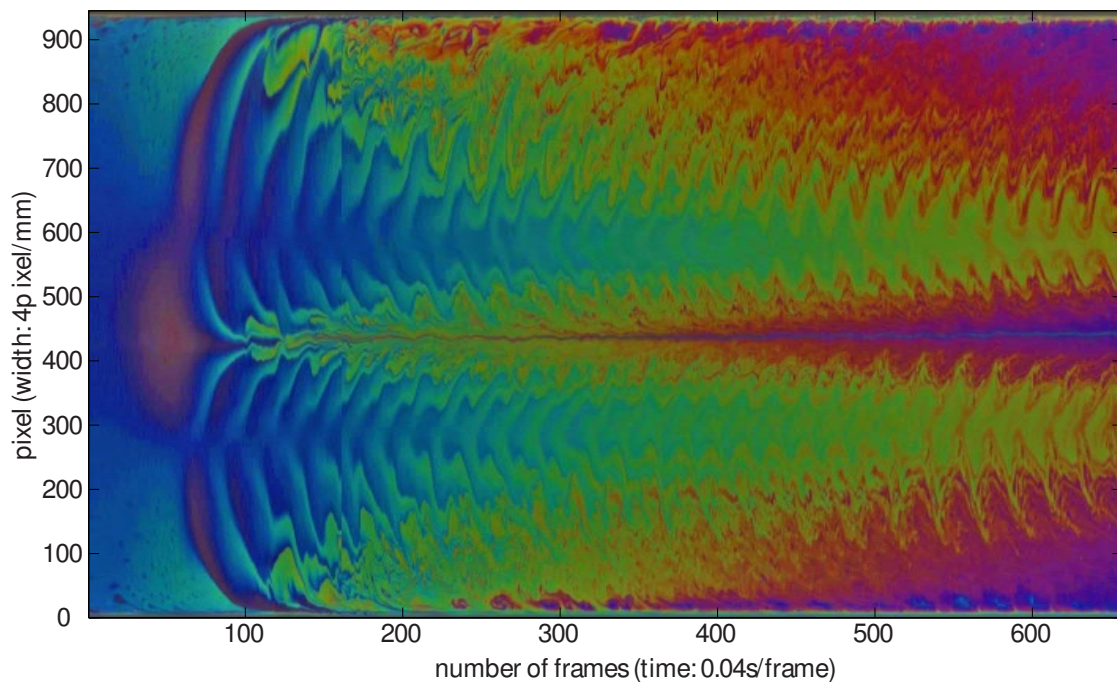


Figure 6.2.: Real color image of a one pixel wide horizontal line through the center of convection over time. The spatial extent is 25 mm . The convection is shown for a timespan of 25 seconds. Cooling rod is in contact with the film.

will still continue in the film with homogeneous thickness, it is just not visually trackable anymore.

In the presented setup the decrease of the variance is linear which indicates good mixing. However, devices designed to implement mixing based on the baker transformation reach faster decays complying to a power law and thereby offer more efficient mixing.

Although the mixing characteristics identified in chapter 3 point towards relatively ideal mixing conditions this difference is the consequence of the relative laminar shear flow in the center of the convection rolls. In this area the crossing of stream lines is less pronounced and it is more likely for a fluid segment to stay in the same orbit.

The variance of the red channel of the fast convection and the variance of the green channel of the slow convection is shown. The behavior is very similar albeit on different time scales. The velocity information given in section 5.2 indicates a fourfold speed increase of the convection with contact to the cooling rod in comparison to no contact. This effect translates directly into the mixing behavior. It leads to an increased efficiency because mixing of the fluid happens significantly faster.

The initial peak can be assigned to the initial pull down of thin material before the actual convection roll develops. It is also noteworthy that the rotational center of the convection is not constant but moves back and forth oscillating around an average center point. This oscillation can be seen in figure 6.2 as the repeating structures along the time axis with a period of roughly 20 frames corresponding to 0.8 seconds.

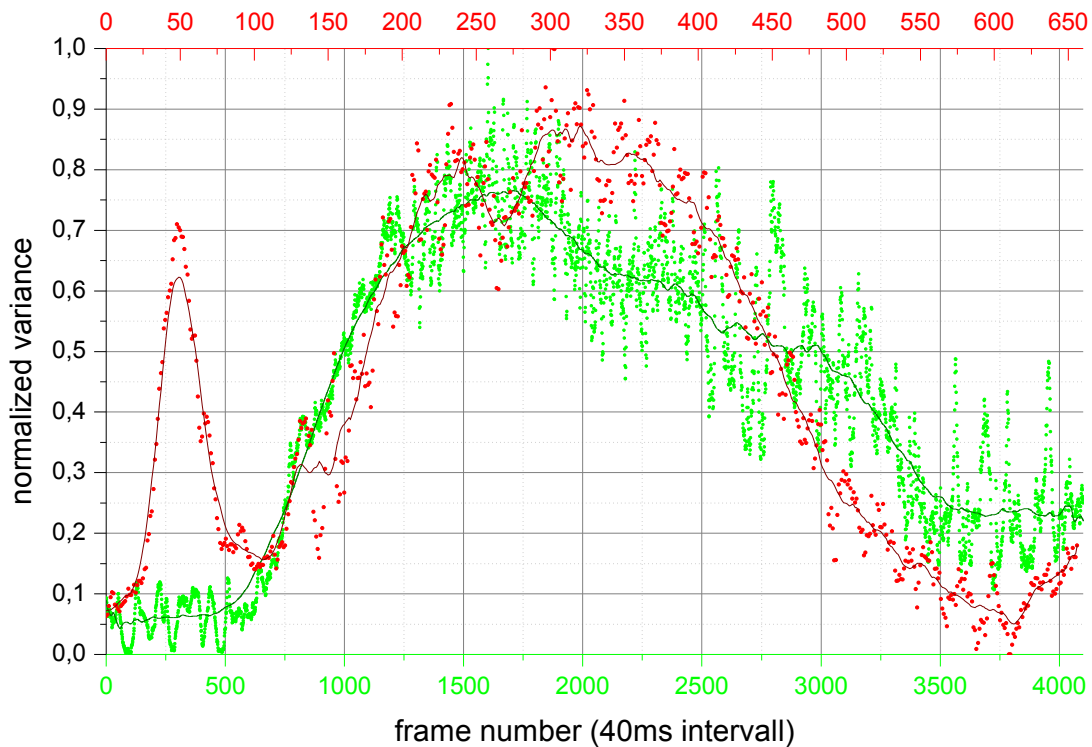


Figure 6.3.: Normalized variance of the center cut images 6.1 and 6.2. Please note that the curves are plotted with respect to different x-axes / time scales.

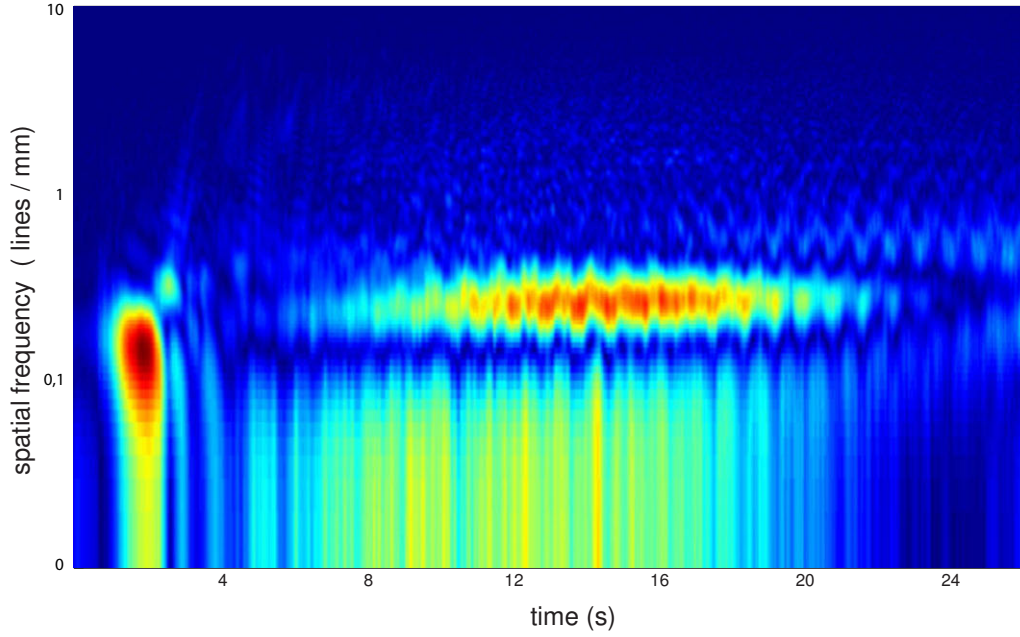


Figure 6.4.: Semi-logarithmic plot of the spatial frequency over time of the red channel of figure 6.2. The intensity is normalized and *linearly* mapped to a color range from blue (0) to red (1).

Frequency analysis Similarly it is possible to analyze the mixing with respect to the frequency behavior. Whereas the contrast between different thicknesses is the basis for the patterns created. The frequency spectrum offers a convenient way to observe the homogeneity and thereby the mixing of the film.

The original data was filtered with a squared cosine window function with one wavelength spanning the width of the frame. This mainly attenuates edge effects that would create high frequency ringing and also smoothes the spatial data. The discrete Fourier transformation is implemented via the fast Fourier transform algorithm with a zero padding of the data to reach a power of two with a four fold number of data points compared to the initial set thereby decreasing the frequency bin size to smooth the frequency spectrum. In the presented example the spatial resolution was approximately $25 \mu\text{m}/\text{pixel}$ which is equivalent to a sampling frequency of $40 \text{ pixel}/\text{mm}$.

As seen in figure 6.4, the Fourier spectrum of the chosen channel shows the same dependency of the spatial frequency amplitude over time like the previous variance calculation. The dominant frequency is located at around $0.43 \frac{\text{lines}}{\text{mm}}$ and increases over time in intensity until a homogeneous color spans the film and no patterns are visible. A general increase of fine structures in the fluid is evident in the broad spectrum frequency noise which rises significantly when the mixing starts. This is more easily identified in figure 6.5 compared to figure 6.4 as it shows the frequency spectrum with a logarithmic color scale.

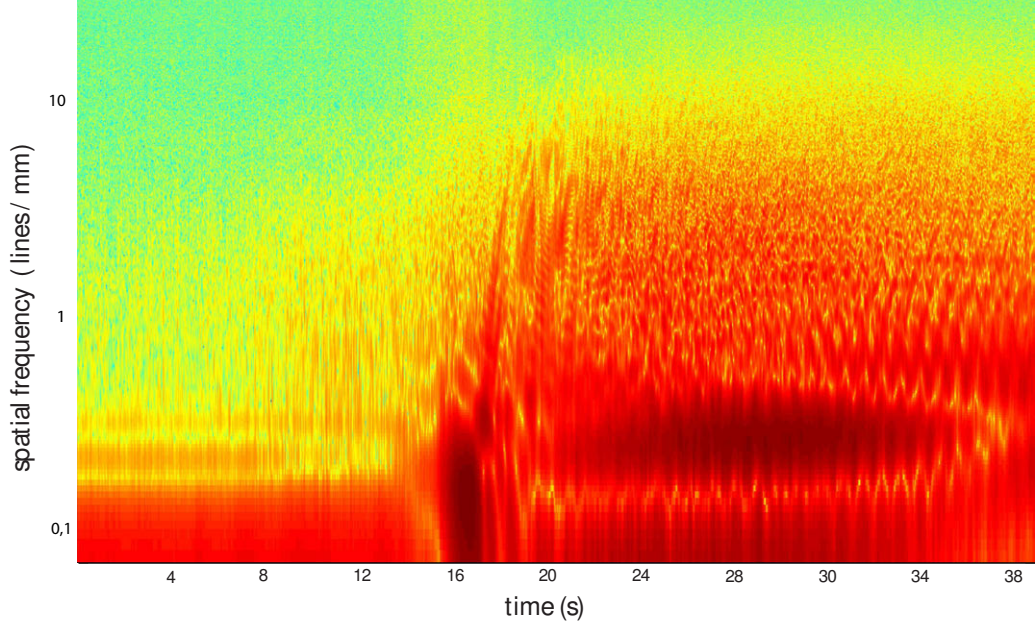


Figure 6.5.: Semi-logarithmic plot of the spatial frequency over time of the red channel of figure 6.2. More frames in the equilibrium state before the turbulence starts are shown to enhance visibility. The intensity is normalized and *logarithmically* mapped to a color range from blue (0) to red (1).

6.1.1. Scale and Aspect Ratio Considerations

The current experiment operates with a rectangular frame oriented vertically with an aspect ratio of 1.6. Accordingly the convection zone below the cooling rod placed in the center of the frame has an aspect ratio of 1.25. When the liquid film contacts the cooling rod the driving force of the temperature gradient is strong enough to involve the complete bottom half of the film in the convective motion and establish a stable state with two convection rolls. By keeping the cooling rod at a distance the convection velocity is reduced and the convection rolls may not reach the bottom margin of the frame. Additionally, two counterrotating secondary convection rolls may develop in the lower quarter of the frame. The convection rolls have a circular shape and are not forced into the rectangle of the frame.

6.2. Key Elements and Quality of Mixing

The temperature gradient and air stream forces thinner material from the top section of the film downwards into the thicker material. This process leads to the formation of two convection rolls. During the motion thin fluid elements are stretched into long filaments that wind around the center of the convection roll which results in folding of the filament on itself. The initial condition of the liquid is a homogeneous system of layers with different thicknesses. To simplify the structural mixing behavior, only two distinct phases are considered in this section.

Firstly, when an arbitrary cluster of thin film is brought into the convection the number of transitions between thick and thin material increases by 2 for each convection cycle. However, continuous observation of this layering process is difficult because the fluid stream of thin material is sequential. In terms of mixing this is a positive effect as the liquid filament is broken up into smaller clusters which may diverge into different orbits. Secondly, the total mixing is enhanced by the inter-convection zone mixing which is quantified in section 6.3.

Another element that increases the overall efficiency of mixing is the turbulent character of the fluid motion. Due to the high shear and velocity gradients at the frame border and different zones of the convection (discussed in section 5.2) a single stream of liquid may branch off into multiple material lines. This effect is generally observable in the outer corners of the convection roll and is schematically displayed in figure 6.6. Due to this effect the folding of the liquid filaments is increased considerably.

A general aspect that needs to be considered is the overall thinning of the convection rolls which can easily be identified by the color change over time: The transition from green over blue to red indicates thinning [20]. The thicker material in the convection center is exposed to a constant centrifugal force which pushes the material to the sides.

Additionally, it is surrounded by thinner material that is accelerated to a lesser extent compared to the core mass due to the linear proportionality of the centrifugal force to mass $F_{cent} \propto m$. However, the thinner material moves at an increased speed compared to the inner material resulting in an increased outward acceleration which should outweigh the mass difference as $F_{cent} \propto \omega^2$. However, this is complicated by the fact that the outer liquid is bound by the frame which forces the fluid to deform. Overall, this study could not reveal whether the thick material is accelerated out of the convection center or if thin material is forced into the convection center.

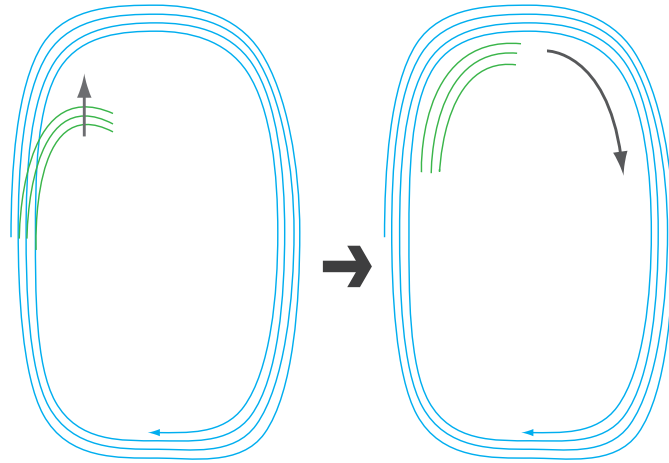


Figure 6.6.: Simplified scheme of the turbulent branching of fluid filaments.

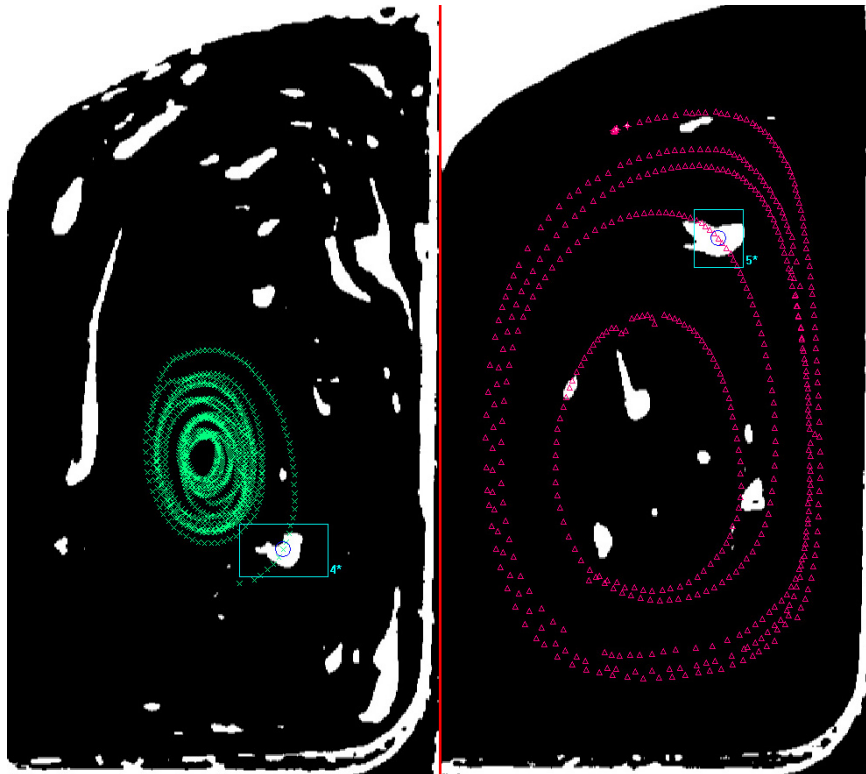


Figure 6.7.: Snapshots of the right convection roll taken from the motion tracking software proAnalyst. Traces of two clusters at different initial positions are shown. Left: moving inward. Right: moving outward.

Tracking of single clusters reveals a critical radius r_C , where clusters on orbits with a radius smaller than r_C tend to move closer to the center during the advection and vice versa. The analysis on this effect was done for a small number of selected clusters which does not grant a statistically reliable quantification.

Nevertheless, it presents a rough estimate. Figure 6.7 shows two clusters of similar size and lifetime that were tracked during the same experiment at different times. Following the path of each cluster validates the stated argument with a critical radius of $r_C \approx 6,2\text{ mm}$.

Due to this directed motion, the central core of the convection roll is less involved in the mixing process which is further diminished by the drastically lower speed of the convection center. However, local mixing due to the velocity gradient is unaffected and the clusters in the center still deform and mix although the exchange with new material from the outer regions is limited.

6.3. Fluid Transfer between Convection Rolls

A key element to determine the fluid mixing is the quantification of the fluid transfer between the convection rolls. After the fluid is accelerated downwards at the center between the convection rolls it is transported either to the right or the left side. The choice of direction is a chaotic process.

The liquid is sucked from the area surrounding the copper rod, more specifically the crystallized disc, into the cooling jet. During this process the liquid undergoes a small change in effective density. This is due to a minor compression which can be identified by a color change. In the following downward motion, the liquid is stretched due to the velocity increase (refer to section 5.2). Afterwards, it is inversely stretched again at the bottom of the frame and then transported into one of the convection rolls.

To analyze the fluid transport, the same video editing function used for tracking clusters was used to uncover the fluid transport. The fluid stream between the convection rolls is predominantly composed of thinner material relative to the thickness of the convection rolls. Therefore, it can easily be identified and all other material can be masked. Three sample frames of the color coding are shown in figure 6.8. To determine the amount of fluid transported per frame, a probing window is placed on the left and on the right side (black rectangles in figure 6.8). The amount of blue pixels in the window is counted and averaged over the width of the window. This is done for a large number of frames to get reliable statistics of the fluid transport.

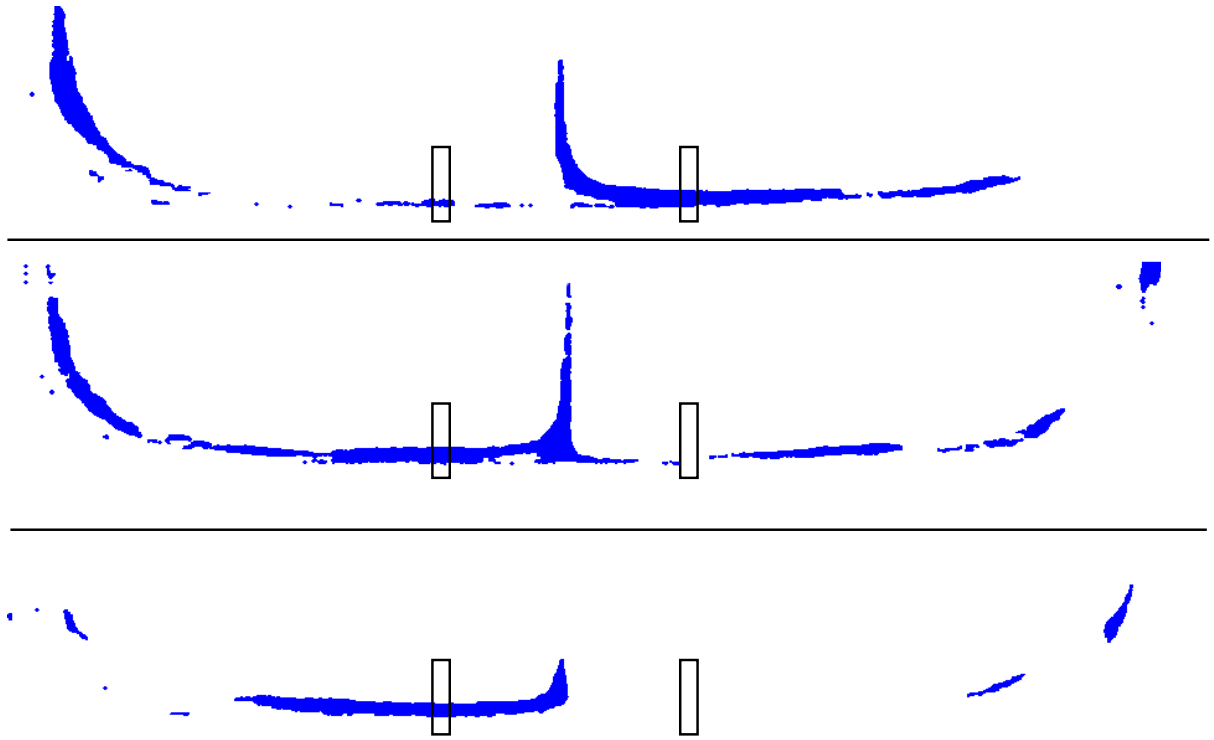


Figure 6.8.: Three individual snapshots of the fluid transport at the center between the convection rolls. The transported liquid is marked in blue. The probing windows are represented by the black squares.

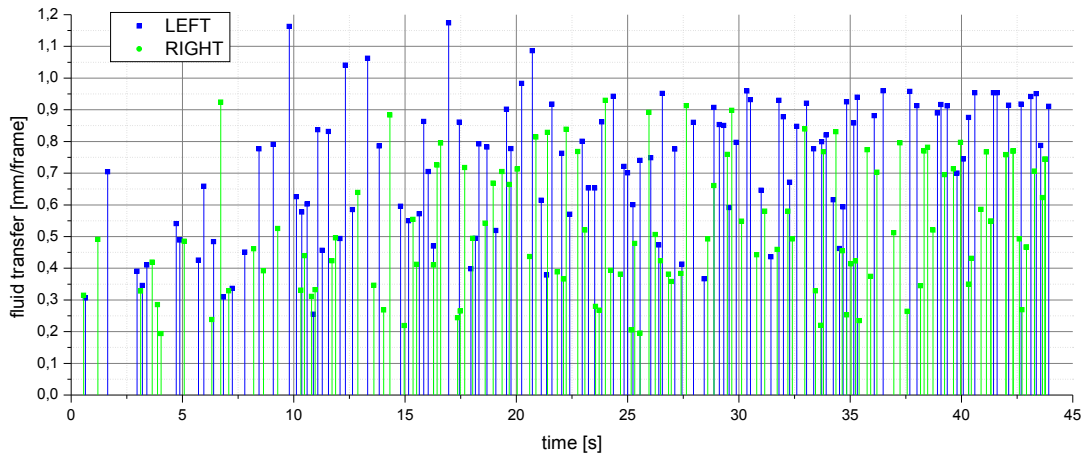


Figure 6.9.: Peak extraction of the fluid transfer area over time.

This procedure is analogous to the volume flow through a given area. However, since this is a two-dimensional system the area flow through a given line is measured. For the left and the right convection roll the peaks of the transported area over time were extracted (figure 6.9). The higher average value of the fluid transport into the left convection roll is due to an asymmetric placement of the cooling rod. This results in a smaller area and slightly faster rotation of the left convection roll. Although the sequence of left and right

transport appears to be random it is possible to determine an average time at which a blob of liquid will be transported distinctly into the right or the left convection roll. This information is readily available in the frequency spectrum of the fluid transport shown in figure 6.10. Despite being relatively noisy the frequency spectrum clearly peaks at around 0.8 Hz with harmonics visible at 1.6 Hz and 2.4 Hz . This results in a fluid transport period of $T_{trans} = 1.25\text{ s}$ for each convection roll.

The average speed in the outer layer of the convection roll is approximately 20 mm/s which results in a period of $T \approx 2.5\text{ s}$ (refer to section 5.2 for detailed velocity information). Thus, for every rotation of the convection roll on average two new filaments are added on each side.

It is important to note that the fluid transfer at the bottom of the frame towards the left and right convection roll is sequential. This is evidenced in figure 6.9 by the distinct identification of peaks in the transport profile.

In consequence, the material merging at the top center is conveyed either to the right or to the left. If the system is symmetric one can assume that both convection rolls contribute the same amount of fluid. With an average count of 15 pixel per vertical line in the probing window, the average area exchanged per second is equal to $3,75\text{ mm}^2/\text{s}$ (total area of the convection zone: 625 mm^2). Figure 6.11 shows the averaged path of the fluid transport and the area from which material is drawn into the convection. This does not necessarily imply that the same fluid is convected along that path without exchange: Due to turbulent motion fluid domains from the center of the convection roll are transported into the upper region and merge. The data shown in figure 6.11 is generated by accumulating the paths taken by the fluid which is marked by the dominant color involved in the inter-roll transport. It therefore resembles the location probability of the exchanged fluid.

Note that new material is also brought into the convection from the top by the two wing like conduits around the crystallization disc (figure 6.11). Due to the high shear rates the flow does not remain laminar and forms turbulent perturbations. The periodic ripple visible in figure 6.11 is a result of a resonant perturbations which enables the exchange of fluid from the out convection into the core and vice versa.

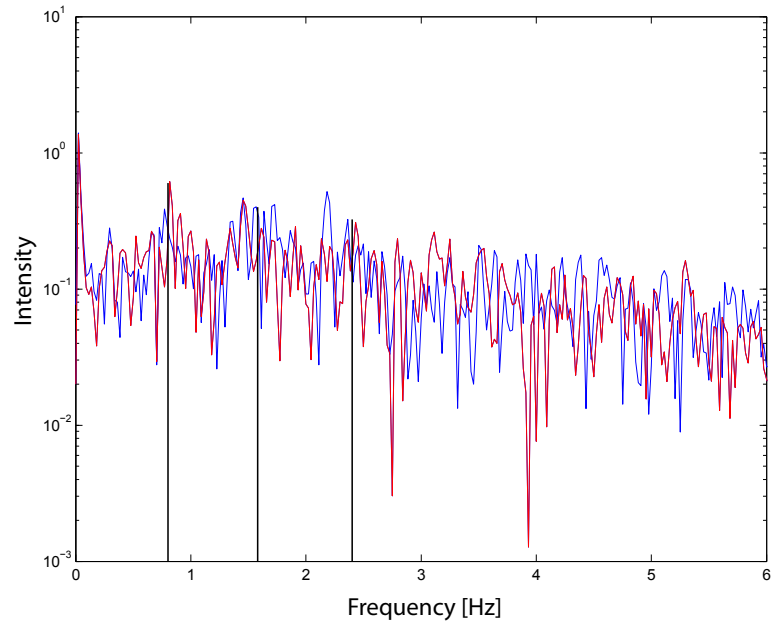


Figure 6.10.: Frequency power spectrum of the inter-convection roll fluid transfer. The red line shows the spectrum of the left probing window. The blue line shows the spectrum of the right probing window. The black markers indicate the position of the determined transport frequency and its harmonics.

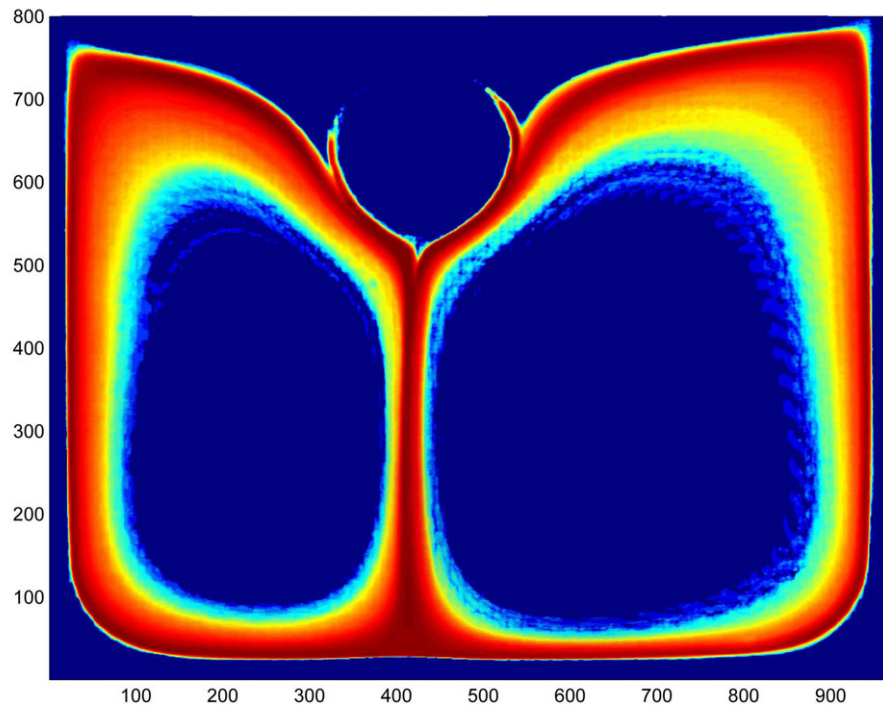


Figure 6.11.: Averaged path of the fluid involved in the transfer between the convection rolls. The color scale (from blue to red) represents the location probability of the fluid exchanged between the convection rolls. The color scale is logarithmic. The coordinates are given in pixels.

6.4. Mixing Efficiency

Conclusively, the overall mixing efficiency can be calculated from the presented experimental data. The linked twist map presented in section 3.4 is valid for a sequential rotation of the left and the right annulus. However, in the experiment both convection rolls rotate simultaneously. The alternating order can be mimicked when the sequential fluid transfer between the convection rolls is used as a means of discretization of the flow.

The key quantities determined in the preceding chapters are the following:

- rotation period of the convection roll: $T_c = 2.5 \text{ s}$
- transport period for sequential fluid transport at the bottom: $T_{trans} = 1.25 \text{ s}$
- spatial distribution of the deformation

As mentioned in the introductory chapters about mixing theory (chapter 3) the quintessence of mixing is stretching and folding. Stretch is achieved by continuous elongation of the fluid filaments in the deformation vector field. Folding happens due to coiling of these filaments due to the rotation of the convection rolls and turbulent horse shoe formation (section 3.3). By considering the fluid velocity in the Eulerian (i.e. laboratory) frame, the length stretch of a fluid filament is given by:

$$\lambda = \lim_{\Delta x_0 \rightarrow 0} \frac{\Delta x_t}{\Delta x_0} \quad (6.1)$$

The local stretching rate ϵ_λ is given by the deformation field (figure 5.5(a), 5.5(b)). This rate is measured in a moving reference system (Lagrangian). As a consequence, the velocity of exponentially separating particles is observed.

$$\epsilon_\lambda = \frac{D \ln \lambda}{Dt} \quad (6.2)$$

This is equivalent to the Lyapunov Exponent.

$$\lambda = \left\langle \lim_{\Delta x \rightarrow 0} \ln \left(\frac{\Delta x(t)}{\Delta x(0)} \right) \right\rangle \quad (6.3)$$

The average $\langle \rangle$ of the stretching rate is along the trajectory which is equivalent to the ensemble average in the case of an ergodic system. The time averaged stretching efficiency E_λ in the Eulerian frame is given in equation 6.4.

$$E_\lambda = \int_0^t \frac{\frac{D \ln \lambda}{Dt'}}{\sqrt{\vec{D} : \vec{D}}} dt' \leq 1 \quad (6.4)$$

In this equation, the symmetric part of the velocity gradient $\vec{D} = \frac{1}{2} [\nabla \vec{v} + (\nabla \vec{v})^T]$ which is equivalent to the stretching tensor, is used as a normalization to obtain a stretching efficiency smaller or equal to one. Ottino demonstrates that the upper bound of the

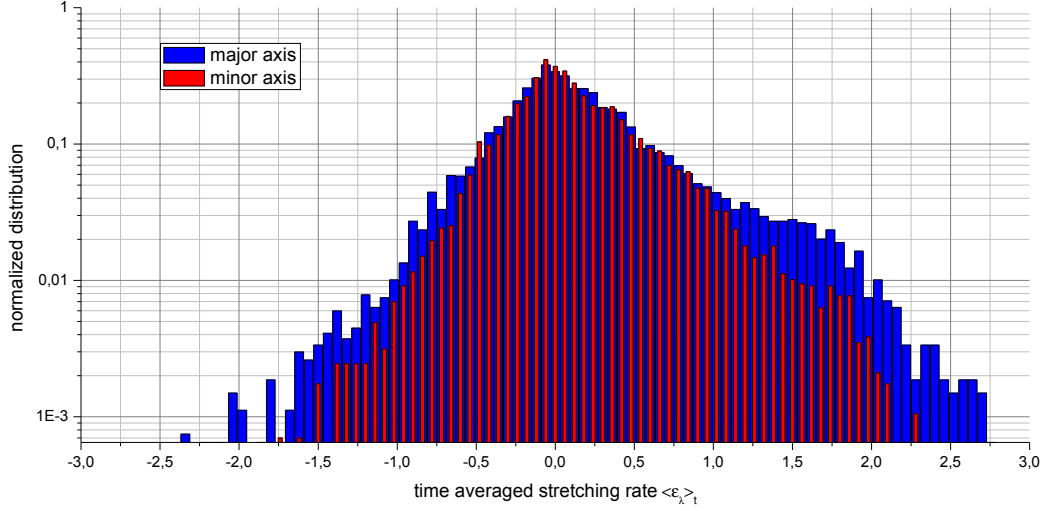


Figure 6.12.: Semi-logarithmic plot of the spatially-averaged stretching distribution.

efficiency for two-dimensional flows is $E_{\lambda,max} = \sqrt{2}/2 = 0.707$ [30]. Since the stretching tensor is not readily available from the cluster data and is only used as a normalization in equation 6.4 it was omitted in the presented analysis. For the primary axis of elongation the time averaged stretching rate distribution is shown in figure 6.12. A semilogarithmic plot was chosen for better visibility of the logarithmic scaling of the stretching rate. To satisfy the limit towards elements Δx_0 of infinitesimal length, the cluster data was filtered to resemble the smallest clusters available while maintaining a sufficient number to acquire reliable statistics.

To acquire the overall stretching efficiency it is necessary to average over time and normalize the distribution shown in figure 6.12. This results for the major axis in $E_{\lambda,1} = \langle \epsilon_\lambda \rangle_{t,\vec{r}} = 0.075$ and for the minor axis in $E_{\lambda,2} = \langle \epsilon_\lambda \rangle_{t,\vec{r}} = 0.071$. The associated variance for the major axis is $\langle \langle \epsilon_\lambda \rangle \rangle = 0.1275$ and equivalently for the minor axis $\langle \langle \epsilon_\lambda \rangle \rangle = 0.0979$.

The distribution of the stretching rate does not yield a sufficiently definite declaration of the stretching behavior. One would expect a distinct peak of positive stretching rates for the major axis which is on average parallel to the direction of maximum shear. Equivalently, the distribution for the minor axis which is parallel to the direction of contraction should yield an overall lower average in the negative domain. The relatively ambiguous distribution in figure 6.12 can be attributed to the average over the whole convection roll. Many clusters rotate in the center of the convection rolls and are not influenced by the severe stretching at the outer orbits.

However, as mentioned previously and illustrated in section 3.3 the mixing in the presented turbulent convection is also influenced by a folding mechanism. Every 2.5 s a fluid filament completes one convection cycle and is folded back onto itself. The sequential fluid transport at the bottom which can be viewed as a generation of a new stretching filament has a period which is twice as fast ($T_{trans} = 1.25$ s). Conclusively, this gives the connection to the picture of Linked Twist Maps and the Baker's transformation. For one folding cycle two stretching processes happen with the overall efficiency E_λ .

7. Thinning

A thick colored film is in a transient state and thins over time due to gravity and marginal regeneration until the equilibrium state, a Newton black film is reached. This chapter focuses on the thinning behavior of a turbulent liquid film in comparison to the unperturbed case. A quantitative analysis of the observed accelerated thinning and black film generation is presented.

7.1. Intrinsic Thin Film Effects and Regular Thinning

For most of the turbulence experiments the thin film is considered to be quasi-static in terms of thinning due to marginal regeneration and gravitation. This assumption is based on the time scale argument that the turbulence is examined within seconds and minutes whereas the thinning of the film after an initial phase of fast fluid drainage slows down and it takes more than an hour to reach the equilibrium state of black film. After the liquid layer is cast rapid motion on the surface is visible for approximately 10 seconds which indicates the drainage of excess liquid into the reservoir. Shortly after, the first color fringes become visible in the top section of the liquid layer.

If the electrolyte concentration is high enough to allow the formation of common or Newton black film small black spots will form in the first minutes at the top border of the frame. These spots coalesce quickly and form a layer of black film with a sharp border towards the thicker, colored film.

It is usually not possible to get a patterned reflective image for the first one to two minutes of the film drainage as the film is too thick thereby diminishing the intensity of the reflection off the back surface. Thinning profiles calculated by Couder et al. [6] with the assumption of constant surface tension and equilibrium thickness predict an exponential shape in the vertical direction of the fluid surface.

While for thicker films the approximation of an exponential wedge like shape can be assumed, thinner films will show a more linear thickness distribution. The thickness profile of a thin film is readily available by evaluating the positions of the maxima of a monochromatic reflection and measuring the distance between them.

In figure 7.1 examples of a thin film with perturbations which are caused by marginal regeneration are shown. Due to the larger thickness difference of the sample displayed in the right image of figure 7.1 the buoyant forces accelerating the thinned liquid domains at the border are higher resulting in a wider area which is affected by the thinning motion. When the overall thickness of the film decreases the upward velocity of the thinned areas is diminished and less turbulences are visible. This is evident in the sample film shown in the left image of figure 7.1.

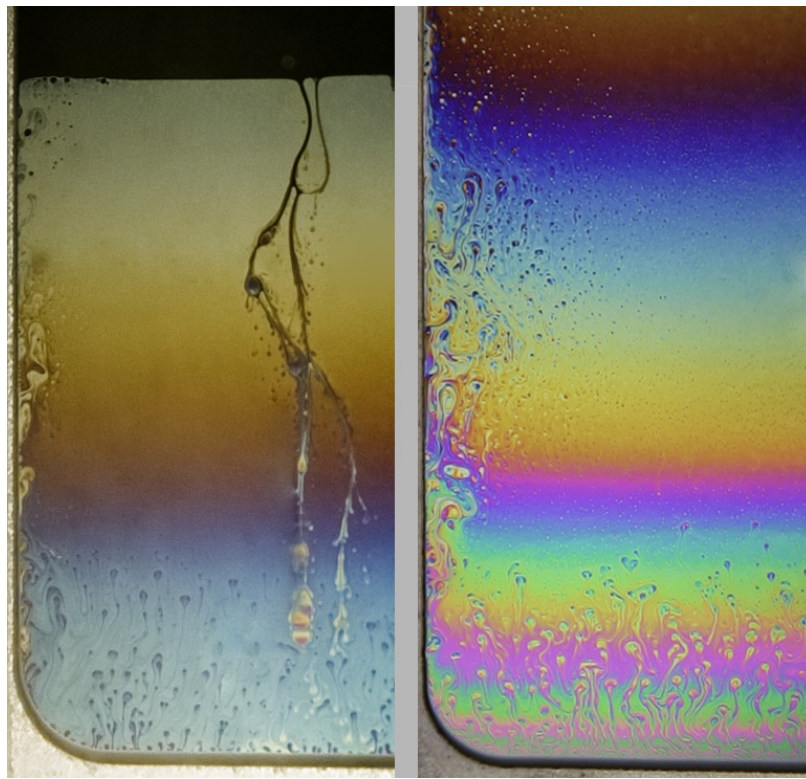


Figure 7.1.: Thinning snapshots taken at two different stages of the film thinning.
left: Progressed thinning. Random black streamers.
right: Thicker film at the beginning of the thinning process; Pronounced marginal regeneration artifacts.

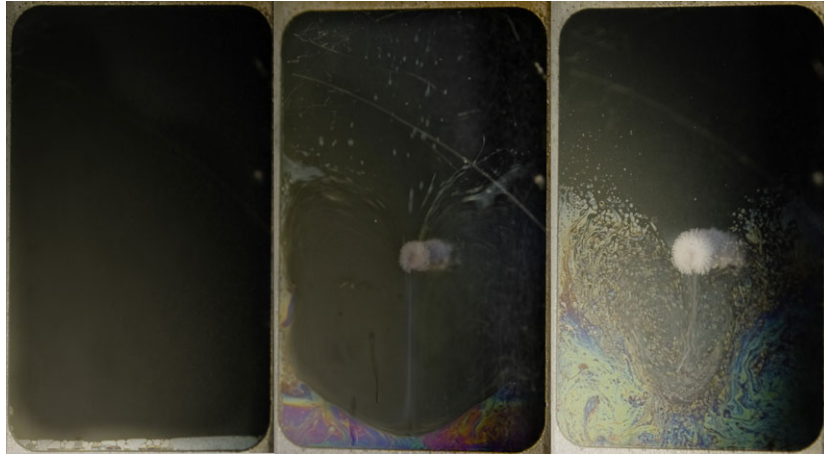


Figure 7.2.: Sequence of snapshots while introducing turbulence in black film with residues of thicker colored film at the bottom of the frame.

As previously documented by Nierstrasz et al.[28] marginal regeneration is present at the bottom of the thin film. However, it does not contribute to the thinning since that would require an increase in thinning speed with increasing width of the frame which is not the case as reviewed in section 2.2.5.

The black streamers shown in figure 7.1 can develop spontaneously but do not lead to accelerated thinning for the surfactant concentration used. It is also possible that these fissures are closed again as can be seen at the lower end of the streams.

7.2. Superfast Thinning

7.2.1. Thinning and Turbulence

residual fluid One aspect of the thinning process which has a significant impact on the turbulence experiments is the drainage of liquid out of the frame. There is usually a reservoir of liquid at the bottom of the frame which may drain completely when given enough time. In the unperturbed thinning which takes more than one hour to fully reach its equilibrium state no such reservoir is present. In the sequence shown in figure 7.2 some parts of the film at the lower border with a thickness of approximately 100 nm have not yet reached the equilibrium state. When turbulence is introduced at that point, thicker liquid is advected back into the black film and hinders turbulence observation in a purely black film. It is therefore essential to allow enough time for the film to fully reach its equilibrium state without any residual thick film.

Due to accelerated thinning (section 7.2.2) the reservoir may still be present even when the liquid film has reached its equilibrium state (black film). It is visible in figure 7.4 as a dark gray stripe between the frame and the convection roll. In contrast to the residual thicker film affecting the black film turbulence sequence in figure 7.2 the thick reservoir in figure 7.4 appears to be sealed off due to surface forces and no thick film is advected.

However, in the convection of thicker colored film it cannot be assumed that there is no transport of fluid from the bottom reservoir into the film.

thickness variation during convection Over time the convection roll will shift its color and it is crucial to note whether the convection roll thins or thickens. This can be independent of the overall faster increase of the amount of black film when the turbulence is present. In general the pattern suggest and overall thinning of the convection roll as the color change is initiated by thin material that is transported down from the top and gradually changes the color of the whole convection roll. As mentioned in section 6.2 the sequence of colors determines whether it thins or thickens. Despite most experiments revealing an overall thinning of the convection rolls there where cases in which the color pattern without doubt indicated a thickening of the liquid layer. These cases however where not stable and ruptured shortly after the introduction of the turbulent motion.

7.2.2. Superfast Thinning

turbulence driven thinning The critical film behavior, first documented by Mysels [26], which destabilizes the liquid film through the spontaneous formation and growth of channels of black film through the thicker colored film and can be introduced by turbulent motion. Mysels attributed the effect solely to the surfactant concentration. This argument may still hold as the turbulent motion can vary the surface concentration of the surfactant thereby favoring the generation of black film islands. The phenomenon of turbulent induced accelerated thinning named superfast thinning is described in the this section.

Depending on the location in the turbulent field where the black film is spontaneously created and the velocity profile these black spots may not be able to escape and coalesce with the top layer of black film. However, due to the disjoining pressure gradient at the boundary to the thick film the diameter of the black spots will increase. Thereby, the buoyant force increases which will eventually lead to the escape of the cluster and merging with the top layer of black film.

The onset of the superfast thinning effect is marked by black film reaching the bottom of the frame and staying there long enough to form a critical amount of black film. The black film at the bottom then starts the chain reaction of generating clusters of black film drifting upwards (figure 7.3, frame 3). The most common incident to initiate the reaction is a drop of thicker film that is surrounded by a precursor of black film and drops to the bottom. These kind of thicker areas are generated when a piece of colored film is completely surrounded by black film. The pressure gradient forces the droplet to thicken further until the gravitational load cannot be supported anymore by the surrounding film. The droplet sinks towards the bottom carrying the thin layer of black film with it. It functions similar to an anchor for the streamer of black film which was created during the descent. The pressure gradient developing between the black film and the thick material at the bottom of the frame leads to a fast expansion of the black film.

The rising black film will divide the colored film into segments which will then start to shrink by increasing their density and fall to the bottom. This process is accelerated by the transport of the black film through the convection zone leaving trails of black film behind which serve as additional sources of black film generation. The black film behaves similar to a soap solution in air creating a two-dimensional foam filled with thicker material. In contrast to conventional foam, in this study the thinner material is

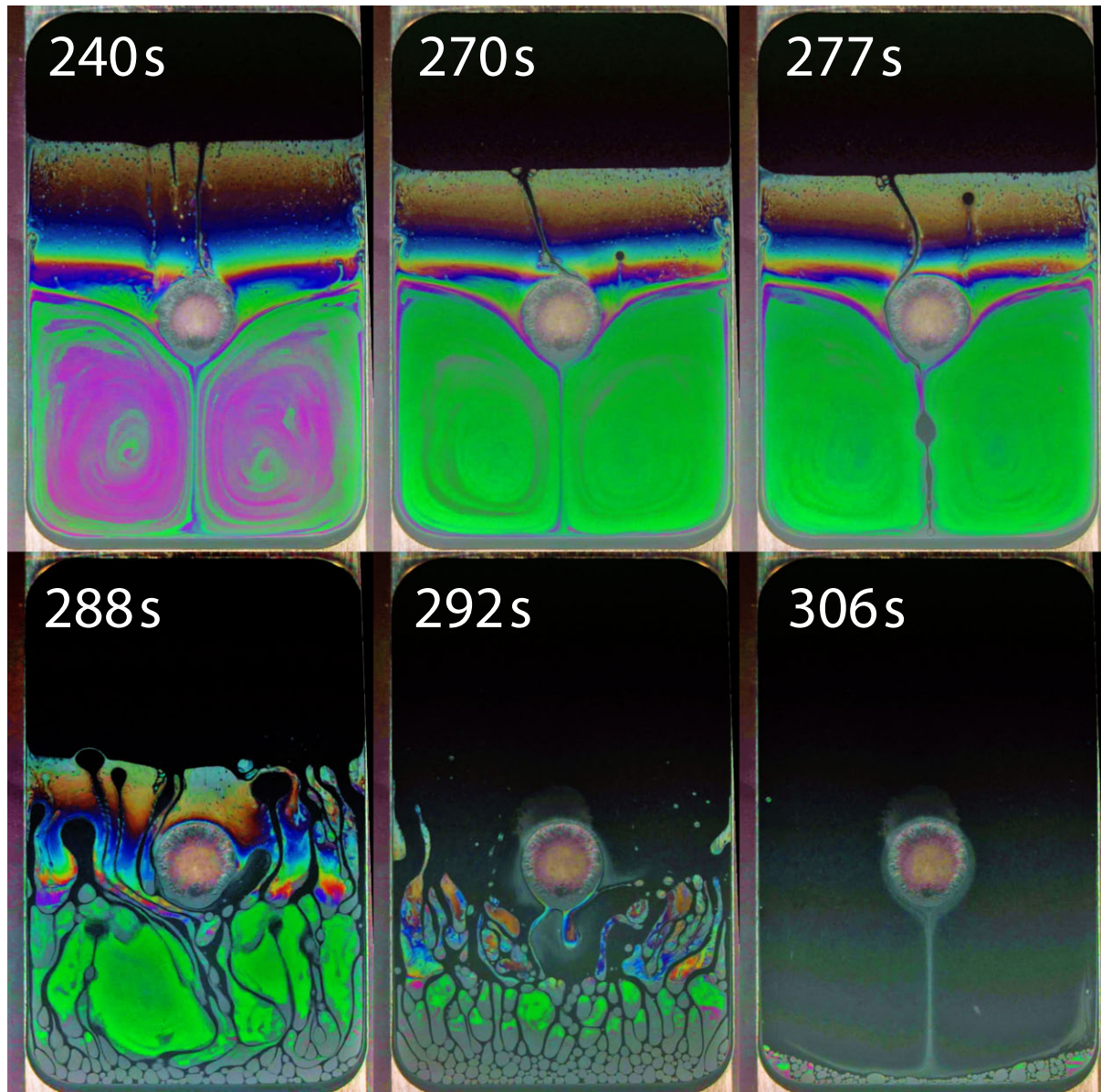


Figure 7.3.: Sequence of snapshots of the developing film destabilization. Shown times are absolute values starting with the film creation.

forming the framework of the foam. This is due to the higher disjoining pressure of the black film.

The reservoir at the bottom of the frame does not show the same interaction with the black film like undrained, remaining thick film does (figure 7.2). The reservoir appears to be sealed off and does not exchange fluid with the convection rolls in the black film after the critical thinning.

frozen particles The gray line that is deflected to the sides at the bottom of the frame (last frame in figure 7.3) is the trace of the cooled liquid. The convection is not concealed by the reflection patterns visible in the thicker colored film and it is possible to track this stream to a certain extent. This is possible due to the extreme cooling that leads to small frozen areas of the aqueous core which appear as opaque spots.

The visible movement of frozen film domains poses the question whether this phenomenon is limited to common black film or if it is possible in Newton black film. Freezing a Newton Black film results in a more rigid, inflexible structure that will probably rupture if a large force is exerted. On the other hand, in common black films it is possible that only clusters of water are frozen inside the aqueous core and the surface remains liquid which enables the transport through the film. Note that pure Poiseuille flow carrying the ice crystals between the surfaces is not possible as the friction at the two surface layers would be too high. Forcing the NBF to crystallize might also break the structure of the ordered water around the surfactant molecules leading to a rupture of the film.

residual droplets The gray colored liquid droplets are the final stage of the compensation between surface tension and disjoining pressure at the interface to the surrounding black film. The liquid cannot escape and is forced to increase its thickness until the surface tension is high enough to counter the pressure exerted by the black film. The gray color indicates that thicknesses in the order of several micrometers are reached as the reflection off the back surface of the film is too low in intensity to produce pronounced interference patterns.

quantitative analysis To quantify the evolution of superfast thinning the total amount of black film was tracked over time for an unperturbed film and a film subjected to turbulent motion. In general, the thinning process is linear with a constant velocity for the front propagation from black into colored film when no perturbation is present (black curve in figure 7.4). This itself is an important observation as the thinning behavior is found to be of exponential nature [26, 41, 39].

The turbulent motion, however, leads to an increased speed of thinning which finds expression in the higher slope of the blue curve in figure 7.4. The contact between the cooling rod and the liquid film is established at approximately 120 seconds after the film creation indicated by the first green marker. Before the contact is established the growth of the black film area is congruent with the previous unperturbed sample. However, an acceleration of the front propagation is not noticeable instantaneously at the moment of contact but approximately 50 seconds later. This can be explained by the successive growth of the convection area which reaches its full size at this time and influences the thinning mechanism at the film margin.

Once the turbulent destabilization sets in, the amount of black film increases to almost 100 percent in a time interval of approximately 25 seconds. The instability onset is marked with a green line at 277 seconds (figure 7.3). Note that the two steps at the beginning of the steep slope are software artifacts introduced by a contrast change necessary to accurately track the amount of black film and are without any physical relevance.

Due to this vastly increased thinning speed it is possible to use this method to reach a frame filling black film significantly shorter than possible with regular unperturbed thinning.

The inset in figure 7.4 is an excerpt of the rapid thinning curve where the y-axis of the graph is inverted therefore being equivalent to the amount of colored film. This was done to allow an exponential decay fit on the superfast thinning data. The assumption of an exponential behavior is justified by the argument that the generated black film itself

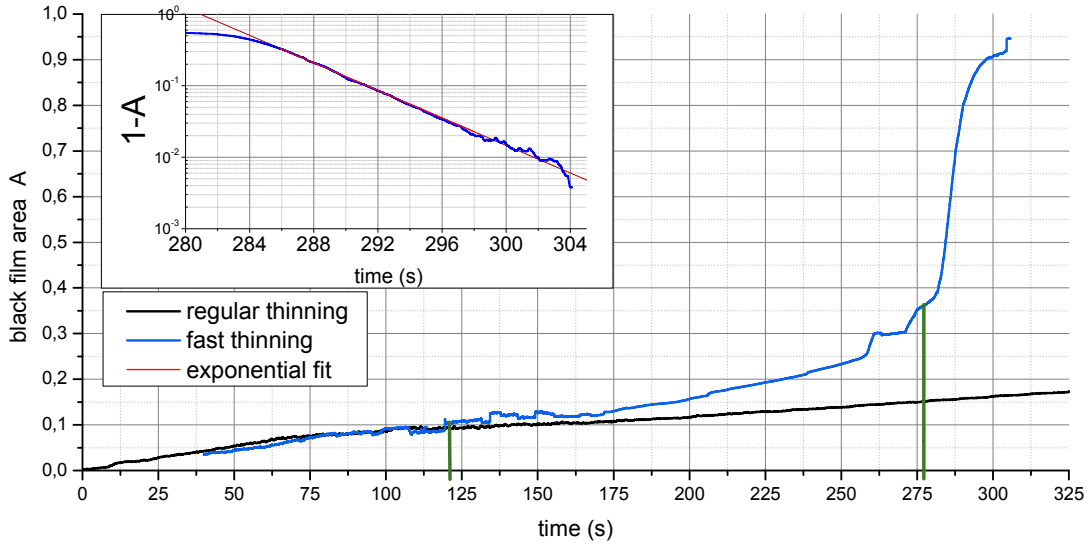


Figure 7.4.: Thinning of an unperturbed and turbulent film over time. Film area is normalized to one. Inset: Exponential fit of the rapid thinning.

serves as a source of new black film constituting a multiplicative process. The captured video data is a discretized representation of the actual film evolution. Each frame the amount of black film increases by a fixed factor which is iterated subsequently and in the limit of $n \rightarrow \infty$ this process approaches the exponential function. The analysis revealed a time constant of $T = 4.5 \text{ s}$ for the decay to $\frac{1}{e}$ of the initial value.

Until now most turbulent experiments ended in the rupture of the black film. A possible cause may be that the solution is designed to reach a NBF in its equilibrium state. Experiments conducted at the MPI-KG suggest that there is no significant phase of CBF in solutions with electrolyte concentrations equivalent to the composition used in the presented experiments. Unfortunately, the tracking of the transition from CBF to NBF - if there is any - is difficult to observe in the given setup and for macroscopic thin films in general. Intrinsically the NBF is a more rigid structure which may not be able to withstand the stress exerted by the turbulent motion thereby leading to the rupture of the film.

Similar experiments focused on the analysis of the critical black film propagation were conducted during the stay in Hong Kong. The thin film was heated from below and cooled from above leading to similar effects as described here. However, the final state of a black film with residual thicker droplets was longterm stable and it was possible to observe convection. Detailed results of this study will be published in the future.

A major difference to previously published thinning rates [26, 10, 41] for thin films is the linear thinning behavior in the unperturbed state and during the turbulent motion before the critical instability occurs. Mysels early quantification of thinning rates of soap films [26] were based on the position of the black film to colored film boundary. This is an equivalent measure compared to the total area of black film calculated in this study. Therefore, are in contradiction with the presented results.

Thickness measurements published by Exerowa [10] or recently by Stöckle [41] measured the thickness of microscopically small films with an interferometer and focused on thicknesses below 100 nm and therefore cannot easily be matched to the experimental results presented in this thesis.

8. Discussion

This last chapter provides a brief compilation of the most important findings from the experimental analysis with emphasis on embedding results in the current state of research in thin film science. The work in hand gives a detailed analysis of the following achievements:

- Hydrodynamic characterization of convection driven thin films.
- Cluster Imaging Velocimetry (CIV) - A new non-invasive velocity and deformation profiling system.
- Classification of the flow in two-dimensional fluid layers in terms of mixing theory.
- Superfast thinning - A very fast mechanism to reach the equilibrium phase of a thin liquid film by accelerated drainage.

8.1. Turbulence

The characterization of flows in two-dimensional systems has been an active field of research for many decades. In recent years with a focus on soap film interference patterns to characterize flow fields. [6, 46, 36, 17, 37]

Turbulent flows are characterized by chaotic changes in velocity and pressure and exhibit a high momentum convection. Although the thermal forcing in the presented setup converges into a stable convection state, it has a number of chaotic properties. The accelerated fluid stream breaks and curls after the jet-like deflection at the bottom margin and friction at domains of lower velocity. Additionally, the direction of the fluid jet when it reaches the bottom is random.

The most carefully studied example of non-linear systems are the convection patterns of Rayleigh-Bénard-Convection. The homogeneous heating of a fluid at the bottom side leads to a temperature gradient and accordingly to a density and pressure variation. Small perturbation due to random microscopic movement then initiate a macroscopic buoyancy driven turbulence. A 2D fluid is inherently different from the continuum setups used and first experiments conducted at the Chinese University of Hong Kong reveal similarities in the type of convection.

CIV technique To allow accurate analysis of the convection in thin liquid films, the mapping tool Cluster Imaging Velocimetry (CIV) was developed. The resulting cluster traces and their volume evolution are utilized to calculate the velocity and deformation profiles of the flow. In comparison to Particle Imaging Velocimetry PIV, CIV has the advantage of a non-invasive tracking as particles used in PIV influence the flow characteristics of nanoscale thin films as recent research by Stöckle et al. revealed [40].

Besides the advantages of capturing a complete snapshot of the turbulent motion there exist certain drawbacks. The imaging is solely based on thickness differences of the material. As a consequence CIV offers only a relative thickness measure in many situations. A virtual volume loss which is introduced by thickness changes due to thinning. This changes the color of the clusters and the difference to the set color effectively lead to a smaller size of the detected cluster.

The cluster algorithm is the basis for the presented analysis and visualization output which makes it necessary to define its limitations. The number of clusters present at a given time and their size characterize the macroscopic flow field and current state of mixture. When a homogeneous thickness of the liquid film in the convection rolls is reached, it is difficult for the algorithm to identify isolated clusters and gather a sufficient amount of data to characterize the flow field. The maximum lifetime of the tracked clusters is limited by the gradual color change due to thinning. This makes it necessary to periodically adjust the selected color and thickness which resets the cluster algorithm. Moreover, the presented analysis the quality of the output is mainly dependent on a high enough frame rate.

Thermal Forcing Similar to Rayleigh-Bénard-Convection the fluid is driven by an externally induced temperature gradient and the resulting density fluctuations. In the presented case the temperature difference is created by a cold copper rod while the frame and liquid are at ambient temperature. The system has a Rayleigh number of $Ra \approx 10^7$ and is therefore comparable to similar turbulence experiments by Zhang, Wu and Xia [48, 37] who reported similar speeds at comparable temperature gradients.

8.2. Mixing

The analysis of the absolute values of deformation and velocity is congruent with observations possible with the naked eye and confirm a two-eddy counterrotating convective motion. The fluid is accelerated at the contact point of the cooling rod and the absolute value of the velocity gradually decays due to friction at the border and low velocity layers.

The vector field of the major deformation component reveals that the primary stretching region is the center stream where acceleration and accordingly the shear between fluid layers is maximized. The major mixing mechanism is the combination of the aforementioned stretch and coiling of these layers around the static center of rotation of each convection roll.

Another key property of the mixing is the folding mechanism present at the lower border of the frame where the stretched fluid forms horseshoes (6.2). In contrast to Rayleigh-Bénard-Convection, which only shows intermittent ordered flow patterns in the form of large scale circulations and otherwise fluctuates randomly, the presented setup yields a very stable convective state. The identified chaotic processes in this system are the formation of horseshoes and the random choice of fluid deflection at the lower border as discussed in section 6.3. The presented features are analysed in terms of mixing theory and compared to established mixing schemes.

Mixing Properties In the presented setup the decrease of the contrast variance is linear which indicates good mixing. However, ideal mixing devices based on chaotic mechanisms (i.e. Baker’s transformation) reach faster decays complying to a power law which results in more efficient mixing. Although the identified mixing characteristics point towards optimal mixing conditions this deviation may be the consequence of the mostly laminar shear flow in the center of the convection rolls where the fluid velocity is low.

The overall mixing efficiency is limited by the low volume transport of 1.6 % of the convected volume per period ($T = 1.25\text{ s}$) between convection rolls. Additionally, it must be considered that on average only 50 % of the mass exchanged between the convection rolls originated in the other convection roll limiting the influx of ”new” material to approximately $1.5 \frac{\text{mm}^2}{\text{s}}$. The time needed to exchange half the fluid between the convection rolls is roughly 1 minute and 45 seconds.

The overall stretching efficiency $E_\lambda = 0,071$ reaches the 10 % margin when compared to the theoretical optimum. This result however is based on the data involving the whole convection field. It has been shown that areas close to the elliptic fixed points of the convection roll are only partially involved in the mixing process. It is therefore feasible that the mixing in the high velocity layers yields a more efficient mixing than the global rate indicates.

The mixing process in the experiment is a quasi 2D mixing scenario where film thickness is attributed to a two-dimensional density. Two image contrast dependent tools were used to analyze the progress of the mixing displayed by finer patterns of streaks with different density: Spatial variance and spatial frequency evolution. The frequency analysis falls in line with the first insights gained by calculating the variance over time as the intensity of high spatial frequency increases accordingly. The streamlines coiling around the center of convection increase the pattern frequency with each period until the structures are finer than the resolution limit and gradually merge into a homogeneous area. The uniformity at small scales is also driven by the surface tension gradient which increases with more densely layered thinner and thicker material exerting an equilibrating force. The result is an equilibration of the thickness differences by material transport perpendicular to the flow field.

8.3. Thinning

For the first time the generation of black film induced by turbulent motion in a foam film has been studied. The perturbation leads to a vastly increased acceleration of thinning and the equilibrium thickness can be reached within minutes instead of hours in the unperturbed film. This provides an excellent tool to reach a black film state very fast circumventing the long waiting times needed in equilibrium thinning scenarios.

Furthermore, it has been observed that stable convection is possible in black thin films. To date this behavior has not been explored yet and will yield new insights into the hydrodynamics of thin films in the continuing studies of this project.

The developed setup yields ideal conditions to pursue any kind of turbulence experiment in thin liquid films.

Superfast thinning is an exponential process based on the expansion of black film due to a disjoining pressure gradient. The instability can be introduced by multiple effects. Known triggers are α -irradiation [15] or heat [9] and now also turbulent motion. The driving of the film with a cold fluid flow as in this study is only one possibility as experiments with temperature induced gradients conducted at the Chinese University of Hong Kong show similar results. The process was even faster due to the increased temperature leading to a lower viscosity and increased molecular movement.

9. Outlook

In this work an experiment aiming at the exploration of dynamical properties of thin freestanding films is presented. It is an initial step in a project aimed at the investigation of thermal convection in ultra thin films.

One potential aspect of future research is the Crystallization of Newton black films and the inherent change in surface structure. The important characteristics of two-dimensional crystal growth are the velocity profile of the front propagation and its shape as it is driven by dendritic growth.

Most importantly the capturing of the visible light reflection spectra of the turbulent motion can be combined with a simultaneous capturing of the thermal convection with an infrared camera. This makes it possible to better identify and quantify the main driving force and boundary conditions of the turbulent soap film. The use of an infrared camera will also allow the observation of turbulence in newton black films where visible light methods are not available. Similarly, the tracking of fluorescent markers can yield a detailed insight into black film turbulence.

The largest potential of this setup is the simulation of classic large scale turbulence experiments with a small scale low cost setup. It is possible to change the aspect ratio of the system in a very large range and thereby alter the turbulence defining parameters (Rayleigh number, Prandtl number) to a great extent.

For the first time stable black film convection in thermally driven nano thin films has been discovered. It poses many ambiguities with regards to established models of thin film science that need to be tackled in the near future.

The insight of the experimental details of a soap film setup gained during this study and the flow field characterization via CIV form the foundation for further analysis and experiments.

A. Appendix

A.1. Cluster Algorithm Source Code

```
function [cluster] = findcluster3D(path,filename,N)
%% import video data

% choose 1=avi or 0=jpeg
import = strfind(filename,'*');
if (isempty(import)) import = 1; else import = 0; end

n = N;      % number of frames
if (import)
    %import from avi source / get first frame
    path = strcat(path,'\',filename);
    reader_obj = mmreader(path);

    height = reader_obj.Height;
    width = reader_obj.Width;
else
    %JPEG read out NOT finished yet !!

    fileFolder = fullfile(matlabroot,'toolbox','images','imdemos');
    %choose directory and base filename
    dirOutput = dir(fullfile('M:\Cluster sequences\','01CCK02_0*'));
    fileNames = {dirOutput.name};
    %n = 100; %choose frame number OR  numel(fileNames);

    I = imread(fileNames{1});
    m = size(I);
    height = m(1);
    width = m(2);
    % Preallocate the array
    % Create image sequence array
    for k = 2:n
        s = imread(fileNames{k});
        frames(:, :, k) = s(:, :, 1);
    end
end

%% cluster

% s contains all information about the ith cluster at frame nr. j
% s0 is a dummy for initialization in the frame loops
s0 = struct('cluster_nr',1,'start_frame', -1, 'end_frame', -1, ...
    'size',0, 'positions',[ ], ...
    'com',[0 0], 'eigval',[0;0], 'eigvec',[0 0 ; 0 0], ...
```

```

    'principal_components', [0 0; 0 0], ...
    'velocity', [0;0], 'angular_velocity', 0,...
    'deformation_rate', [0;0]);
s = s0;
% cluster contains a list of f for each cluster number i
% f contains a list of s for each frame the ith cluster is found
% below cluster{c} contains the list of frames which contain each a struct s
% cluster{c}{k} contains a struct s
% which is addressed by cluster{c}{k}.field_name

% init cluster array
cluster=cell(1);
cluster{1}={};

%%

ci = 1; % keep only 2 cframes
for k=1 : N
    vid_frame = read(reader_obj,k);
    frame = vid_frame(:,:,1);

    cframes(:,:,ci)=uint16(bwlabel(frame));
    cl_index = unique(cframes(:,:,ci));

    temp_cframe = (cframes(:,:,ci)>0)*(-1);

    %i=2 : ignore background cluster with zeros
    for i = 2 : (length(cl_index))
        s=s0;
        %get positions of current cluster
        [row col] = find(cframes(:,:,ci)==(cl_index(i)));
        y = row;
        x = col;

        s.positions = [x y];
        s.size = length(s.positions(:,1));
        if (s.size > 1) s.com = mean(s.positions)';
        else s.com = s.positions'; end

        %beginning continious numbering with second frame
        if(k>1)
            n=1;
            %check if a cluster is present at previous frame for all positions
            while(n<=s.size && ~cframes(row(n),col(n),ci-1))
                n = n+1;
            end

            if (n<=s.size)
                cluster_found = 1;
            else
                cluster_found = 0;
            end

            % cluster in previous frame found
            % -> replace current index with previous one
            if(cluster_found)
                %get previous cluster number
                prev_cl_nr = cframes(row(n),col(n),ci-1);

```

```

        % if another cluster in the current frame is already connected to
        % the previous frame and cluster(pre_cl_nr)
        % a new cluster number is assigned
        if(length(find(temp_cframe==prev_cl_nr))>0)
            s.start_frame = k;
            s.cluster_nr = length(cluster)+1;
        else
            %previous cluster is not yet connected
            s.start_frame = cluster{prev_cl_nr}{1}.start_frame;
            s.cluster_nr = prev_cl_nr;
        end
    else
        %use current frame as start_frame if no previous cluster was found
        s.start_frame = k;
        s.cluster_nr = length(cluster)+1;
    end
    for m = 1 : s.size
        temp_cframe(row(m),col(m)) = s.cluster_nr;
    end
    % when all testing on cframes 2 is done revert ci to 1 so that
    % temp_frame is written to cframes 1.
else
    %first frame needs to be treated separately
    s.start_frame = 1;
    if(i==2) s.cluster_nr = 1;
    else s.cluster_nr = length(cluster)+1;
    end
end

%create new cluster when the cluster nr is lower than the current max
%and cluster wasn't found in previous frames
if (s.cluster_nr<length(cluster) && isempty(cluster{s.cluster_nr}))
    cluster{s.cluster_nr}={};
end

% standard case for new clusters -
if(s.cluster_nr>length(cluster))
    cluster{s.cluster_nr}={};
end

%calculate eigenvalues and eigenvectors
cov_matrix=cov(s.positions);
[v,e] = eigs(cov_matrix);
s.eigvec=v; s.eigval = diag(e);
%append current struct to appropriate cluster
cluster{s.cluster_nr} = [cluster{s.cluster_nr} s];

end
ci = 1;
cframes(:, :, ci) = temp_cframe;
%set ci=2 so that the next cframe is written into the second slot.
%previous data from temp_frame is stored in cframe 1.
ci = 2;
end

%% set correct end_frame in all members
Nclust=length(cluster);
for nc=1:Nclust
    cl_length = length(cluster{nc});

```

```
endframe=cluster{nc}{1}.start_frame + cl_length-1;
for nf=1:cl_length
    cluster{nc}{nf}.end_frame=endframe;
end
end
```

A.2. Publications

The pioneering character of this work lead to numerous presentations of the topics and a publication which presents partial results of the analyzed thin film turbulence. In the following the presentations and papers are listet:

- presentation during the High Rayleigh Convection - Euromech Colloquium #520 in Les Houches, France
- presentation during the International Conference on Multiscale Complex Fluid Flows and Interfacial Phenomena (MULTIFLOW2010) in Brussels, Belgium
- presentation during the 3rd Conference on Non-linear Science and Complexity (NSC10) in Ankara, Turkey
- peer reviewed paper which was published in the conference proceedings of the aforementioned NSC10 conference.

For reference the published paper is included in this work on the following pages.

Turbulent Mixing in Soap Films

M. Winkler * S. Stöckle ** G. Kofod * R. Krastev *** M. Abel *

** Institute for Physics and Astrophysics, University of Potsdam
(e-mail: Michael.Winkler@uni-potsdam.de).*

*** Max-Planck-Institute for Colloids and Interfaces, Potsdam
(e-mail: Silke.Stoeckle@mpikg.mpg.de)*

**** Naturwissenschaftliches und Medizinisches Institut, University of
Tübingen (Rumen.Krastev@nmi.de)*

Abstract: We show first results on a thermal convection experiment with very thin aqueous films. Film thinning is an important but very slow process. For our experiment, we use an enhanced experimental setup and extremely well-controlled chemistry :n-dodecyl- β -maltoside is used as the surfactant stabilizing the sheet of water making it possible to reach stable common and Newton black films. We demonstrate how thinning can be enhanced by a temperature gradient which in turn drives the film into a turbulent regime. Consequently, we analyze the flow with respect to its mixing properties using statistical tools. The mixing in each vortex is characterized by the average of the stretching over the vortex area whereas the crossing of the separatix describes the global mixing. Applying effective diffusion and finite size analysis, we characterize the mixing efficiency in terms of the probability distribution of increments in time and space.

Keywords: Thin Film, Nanofluid, Mixing, Turbulent Convection, Rapid thinning

1. INTRODUCTION

Liquid thin films are found everywhere in nature, such as in cellular membranes, condensation layers on surfaces, and in general on interfaces between material domains. This contribution reports on experiments on a soap bubble captured in a frame, that combines three scientific areas: thin, free-standing films, thermal convection, and mixing. Thin films are not only beautiful as soap film, but highly important for process engineering and life sciences. Further, the limits of physical theories are tested when films become exceedingly thin, i.e., on the nanometer scale. Convection is often considered in the context of Rayleigh-Bénard (RB) convection as a model for large systems as the earth mantle convection and atmospheric, thermally driven turbulence. Mixing, finally, is very important in process engineering, wherever one or more substances must be brought to reaction consistently.

A thin-film forming system was placed in a closed container to prevent evaporation and to control the thermodynamic state. The setup is based on a measuring cell that was designed at the Max-Planck-Institute for Colloids and Interfaces and is not yet published. Very thin translucent films and thicker opaque films can both be prepared with a lifetime of several hours. A cooling rod was inserted through a hole until it just touched the film, thus creating the desired thermal gradient. Thus, cooling occurred in a small area of the film, and heat from everywhere else flowed to the point of cooling – an experimental realization of the condition ideally described as „cooling from above, heating from below”, as in RB convection. When cooling begins, a highly turbulent movement of film portions sets in. approximation. The motion can be observed visually

and in real time, hence video recording is used and the images subsequently characterized by statistical analysis and tracking of the fluid. The experiments show that a lubrication approximation can be employed, where the dynamics in film-normal direction is effectively decoupled and can be independently described by a thin-film equation. Thus, the dynamics of the free-standing film are found to be effectively two-dimensional.

2. EXPERIMENTAL METHODS

A film consisting of pure water ruptures almost immediately due to the capillary forces generated by the surface tension. Adding a surfactant that covers the surface of the film generally reduces the surface tension and increases the surface elasticity, therefore stabilizing the sheet of water. Several further components help maintain film stability over hours, these are described in the following.

Macroscopic foam films are obtained by spanning an aluminum frame with surfactant solution, creating a quasi two dimensional liquid film with an area of several square centimeters. The base solvent is deionized water with a residual conductivity of $1.37 \mu S/cm$. The use of purified water for solutions is generally recommended (Muruganathan et al. (2004)), as it reduces contaminations with non-conducting carbon chain remnants. However, it was found here that soap film stability and ultra thin film formation (thickness $\leq 10nm$) was not affected by the type of water used.

Glycerin is also required to achieve macroscopically large films with an area of several square centimeters or meters (Martin et al. (1998); Kellay et al. (1995)), serving to adjust bulk and surface viscosity. Due to its high viscosity

($\eta = 945 \text{ mPa s}^{-1}$, compared to $\approx 1 \text{ mPa s}^{-1}$ for water) it reduces the thinning speed of vertical films and allows the film to remain stable for a longer period of time (Isenberg (1992)). Typically, a concentration of 25 %_{vol} was used, yielding a net viscosity of $\approx 2 \text{ mPa s}^{-1}$ (Rutgers et al. (2001)). Frequently, experiments on 2D fluid dynamics involve a constant flow and replacement of the film material (Kellay et al. (1995); Shakeel and Vorobieff (2007); Yang et al. (2001)), which requires a different soap composition (Rutgers et al. (1996)).

The electrolyte concentration also has a major effect on film stability and thickness (Zhang et al. (1996)). The addition of ions shields the electrostatic double-layer repulsion as described by the DLVO-theory (Derjaguin (1989)) hence permitting the appearance of a black film. Here, sodium chloride was chosen, since it has negligible influence on surface tension and critical micelle concentration (CMC). To eliminate any surface active contaminations, the laboratory grade *NaCl* (Merck, Darmstadt, Germany) was roasted at 600°C .

The chosen surfactant, n-dodecyl- β -maltoside (here after $\beta\text{-C}_{12}\text{G}_2$), belongs to a new generation of sugar-based surfactants which are non-toxic, biodegradable and low cost. It consists of hydrophilic head group, made up of two glucose rings ($\text{C}_6\text{H}_{12}\text{O}_6$) connected by an ether bond, and a hydrophobic alkyl chain ($\text{C}_{12}\text{H}_{25}$). The surfactant is soluble in water so that the hydrophilic head group is submerged in the core liquid. The hydrophobic tail is oriented normal to the liquid-air-interface and not in contact with film surface. All experiments were performed with a concentration above the CMC, to guarantee that the equilibrium surface tension remains constant. Above CMC, deviations in surface surfactant density are compensated by diffusion of surfactants from or to the bulk liquid.

3. THIN FILMS

NBF vs. CBF The thinning of a membrane can terminate in two distinct equilibrium states. One being the Common Black Film (CBF) and the other one being the Newton Black Film (Exerowa and Kruglyakov (1998)). The latter is a bilayer formation of the surface stabilizing surfactant molecules without an aqueous core. This state can only be reached with a electrolyte concentration high enough to shield the long range molecular repulsion forces of the two surfaces so that the final thickness is only determined by the balance between surface and disjoining pressure. Common Black Films on the other hand are achieved when there are only very few free ions present and the film is stabilized due to electrical double layer repulsion. Because of the dissimilar stabilizing mechanisms it is expected that there is a distinct difference in crystallization behaviour. Typically a Newton Black Film reaches a thickness of roughly 5 nanometers whereas Common Black Films develop at a thickness of approximately 15 nanometers (Muruganathan et al. (2004)). Since we are forcing motion in the film it is necessary to keep in mind that these results are equilibrium values. Therefore the actual thickness in our experiment may vary.

The disjoining pressure for freestanding films is given by the sum of the Van-der-Waals and electrostatic pressure:

$$\Pi = \Pi_{VdW} + \Pi_{el} = -\frac{A}{6\pi h^3} + \frac{\epsilon\kappa^2}{8\pi}\Psi_0^2\text{sech}^2(\kappa h) \quad (1)$$

Whereas A denotes the Hamaker constant, h is the film thickness, ϵ is the dielectric constant of the medium, κ is the inverse Debye length and Ψ_0 is the surface potential. The electrostatic part is based on solid charged wall model which implies that the charges are located at the air-water-interface for non-ionic surfactants. Note that the application of this model for thin films is still under debate (see Stubenrauch et al. (2004) and the references in there).

The thinning of these films is governed by a pressure difference between the border the film area which is generated by a change of surface curvature Stein (1991). Due to the increased thickness of the films at the margins it is believed that the liquid is mainly drained by ducts at the vertical frame film interface whereas the transport of liquid towards the margin is driven by a surface tension gradient Nierstrasz and Frens (1999). The average thinning velocity in our setup is around $v = 18\mu\text{m/s}$.

4. THIN FILM CONVECTION

When a fluid is subject to a temperature difference at two different places, above a critical value, the onset of convection is observed. The famous Rayleigh-Bénard System Ahlers et al. (2009); Squires and Quake (2005) is well-studied and yet some fundamental questions are still unsolved, regarding the scaling behaviour of Nusselt vs. Prandtl for high Rayleigh numbers or the dependence on aspect ratio and the question of universality.

In our setup we bring a liquid film in contact with an extremely cold metal tip (roughly -160°C) that introduces a temperature gradient which generates turbulences which are observable with the naked eye. It also forces the liquid to crystallize to a certain extent until a thermal equilibrium is reached. In addition the cooling rod also creates a cooling wind right behind the film which also enhances the turbulences by driving the surface due to friction at the surface. A sketch of the experiment is given in Fig. 1

The system is described by the Navier-Stokes equations, here, we use the 2D approximation with temperature in the overbeck boussinesq approximation, the thickness is described in the lubrication approximation coupled to the fluid through the boundary conditions. The lubrication approximation assumes that scales in x and y are large compared to the typical film thickness (z -dimension). An equation for the film thickness $h(x, y) = h_r(x, y) - h_l(x, y)$ is derived by multiscale expansion Oron et al. (1997), assuming independence of the left and right surfaces h_l , h_r .

$$\mu\partial_t h + \nabla_1 \left[(\tau + \nabla_1\sigma) \left(\frac{1}{2}h^2 + \eta h \right) \right] - \nabla_1 \left[\left(\frac{1}{3}h^3 + \eta h^2 \right) \nabla_1 (\Delta\Phi - \sigma\nabla_1^2 h - \Pi) \right] = 0, \quad (2)$$

with $\nabla_1 = (\partial_x, \partial_y)^T$, σ the surface tension, η the slip coefficient between surface and air, $\Delta\Phi = \Phi|_{z=h_l} - \Phi|_{z=h_r}$, Φ describes a body force, here this is gravity, τ and Π are

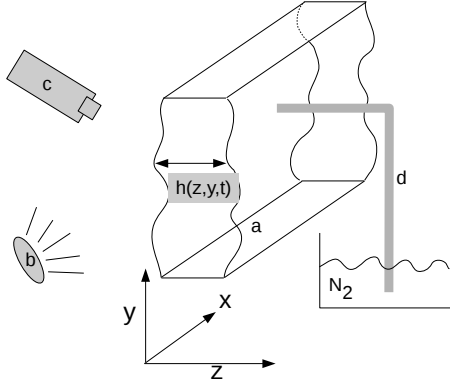


Fig. 1. Setup of the experiment. (a) schematic sketch of the free-standing thin film, (b) light source, (c) camera, (d) cooling rod with liquid nitrogen reservoir.

tangential and normal forcings at the surface (left/right). For the temperature, we have At h_l , and h_r , respectively we have

$$\kappa_{th} \nabla \theta \cdot \mathbf{n} + \alpha_{th} (\theta - \theta_{\infty}) \quad (3)$$

α_{th} : heat transfer to ambient, θ_{∞} : outer temperature. And in the bulk we assume Overbeck-Boussinesq Ahlers et al. (2009)

$$\partial_t \mathbf{u} + \mathbf{u} \cdot \nabla_1 \mathbf{u} = -\nabla_1 p + \nu \Delta_1 \mathbf{u} + \beta g \delta_{i3} \theta \quad (4)$$

$$\partial_t \theta + \mathbf{u} \cdot \nabla_1 \theta = \kappa_{th} \Delta_1 \theta \quad (5)$$

ρ : density, c : specific heat, κ_{th} : thermal conductivity. β : thermal expansion coefficient. For a two-dimensional thin film, to 0th order one can assume that the thickness is advected passively. But the surface tension depends parametrically on the temperature, and thus certainly becomes important in the next better approximation. Of course, in contrast to usual thermal convection, chemical potentials and surfactant forces matter.

With our parameters the Rayleigh number is quite high, $Ra \sim 10^6$ which clearly yields turbulent behaviour in the fluid. Please note that for very thin films it is not clear how viscosity changes with the film thickness.

Since we use a point thermal force for driving our system, we have two rolls on either side of the cooling rod. A snapshot of the thin film is given in Fig. 2.

5. MIXING

The analysis for the presented experiment is based on the fundamentals of mixing, which include the identification of the mixing scheme (i.e. tendril whirl flow or blinking vortex flow) and stationary points and orbits. Geometry wise the soap film can be treated as a two dimensional fluid with an area to thickness ratio of approximately $2 \cdot 10^4$. The current setup forces two counter rotating annulars which are bounded by the rectangular frame. At the intersection of the two annuli the counter rotating shear results in a co-twisting linked twist map. The description of any mixer in terms of linked twist maps (LTM) gives

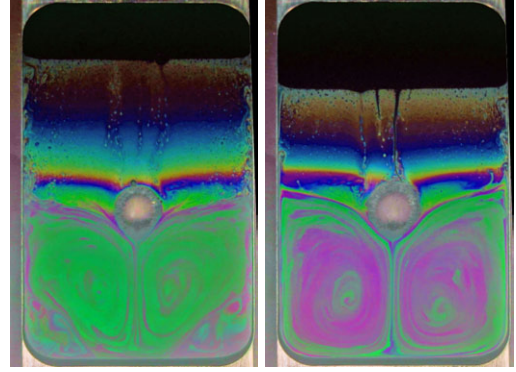


Fig. 2. Snapshot of a turbulent convecting thin film. Center (grey/white): The copper needle surrounded by ice. On the sides the typical meandering of rising thin/sinking thick film is observed. On the top a layer of black film has formed which is transported downwards. Thickness can be read from the colors. Left: The convection is not yet fully developed, such that corner vortices are observed; they disappear after transients. Right: Turbulent convection has fully developed and thin film is transported and mixed quickly by the convection. Of course, the same holds for hot/cold film (not shown). The time difference between the two pictures is 60s.

a quantitative understanding of the efficiency and quality of its mixing properties. LTMs are simply defined by the composition of a uniform shear map and a twist map ($M_{LTM} = M_{shear} \circ M_{twist}$). For one annulus the twist map in angular coordinates can be written as

$$M_{LTM}(r, \theta) = (r, \theta + f_1(r)) \quad (6)$$

The annuli are centered at a certain distance l out of the center. It is therefore necessary to apply a transformation that shifts accordingly:

$$T_1(r, \theta) = (r \cos \theta - 1, r \sin \theta)$$

$$(7) \text{ shift for left annulus}$$

$$T_2(r, \theta) = (1 - r \cos \theta, -r \sin \theta)$$

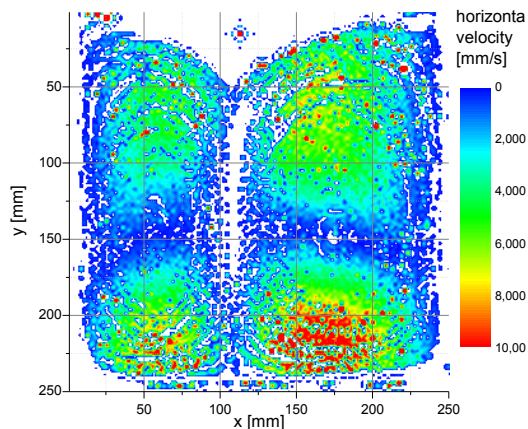
$$(7) \text{ shift for right annulus}$$

It is now possible to combine the two transformed twist maps to describe the system:

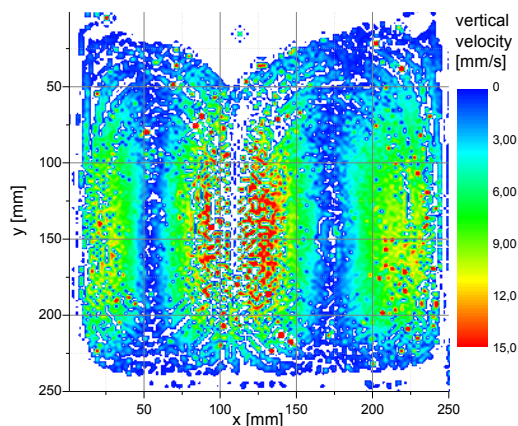
$$M = T_1 M_{LTM}^{(1)} T_1^{-1} \circ T_2 M_{LTM}^{(2)} T_2^{-1} \quad (8)$$

It is assumed that M is a bijection. However due to the nature of the experiment the fluid domains of varying thickness will diffuse to a certain extent and therefore are not volume conserving. Nevertheless we consider the diffusion constant is small enough to be neglected. Applying this ergodic theory to the presented setup possess the problem that the consecutive twist (i.e. blinking vortex flow) of the right and left annulus actually acts simultaneously. Further details on the theory of mixing can be found in Sturman et al. (2006).

In the generated velocity field (Fig. 3) the fluid is stretched in regions of high velocity and compressed when it enters areas of lower velocity. Due to the shear which is present



(a) horizontal velocity



(b) vertical velocity

Fig. 3. averaged velocity field of the forced advection

between layers of different velocity folding happens. These two processes are the main aspects of mixing in a two dimensional fluid. Diffusion processes can be neglected as the Reynolds number is of the order of 10^3 .

We consider a very peculiar situation since we have two rolls, one on each side of the device. There are two hyperbolic points at the bottom and directly below the ice lowest part of the ice surrounding the cooling needle and a separatrix running top-down. In a way we have the minimum setup for mixing between vortices, but in contrast to the well-studied blinking vortex flow, the vortices are maintained, similar to macroscopic flows, Ottino (1989). So, we characterize mixing within the two rolls by an effective diffusion approach and the mixing between the two rolls again by an averaging procedure, taking into account the probability to cross the separatrix in the middle of the setup.

To compute the local stretching we cast the colors into black and white by choosing a specific color / thickness (white) and the rest (black). The movement of these spots

can be tracked by following the „clusters” of a certain color, this analysis is described below. An analysis by means of the FSLE Aurell et al. (1996); Cencini et al. (2009) is on the way. Here, we calculate for each instant of time the center of mass, the principle axes, the corresponding eigenvalues, giving the stretching/contraction rate, and the volume shrinking (because a spot thins in time and thus changes color). From these we calculate the velocity as a finite difference, and finally the angular velocity.

The overall mixing can be characterized within each vortex as an averaging of the stretching rate over the vortex area. The global mixing between the vortices is characterized by the probability of a fluid element to cross the separatrix. This procedure can be seen in the view of effective diffusion, because the averaged turbulent velocity field is a kind of random walker with possibly anomalous and space dependent transition rates, which when averaged yield the diffusion coefficient. The transition from one cell to the other is the minimal setup, as discussed in Abel et al. (2000).

We use a naive approach to analyze our film: take a spot of material of size Δx , compute its time derivative approximatively from the time evolution as finite difference and use then averaging to determine the macroscopic properties. This is in contrast to studies with particles, where the velocity of relative dispersion is calculated, and only possible because we have already a field at hand. From the clusters of the same thickness, we obtain the eigenvalues $e_{1,2}^i$ along the principal axes; they correspond directly to the size of the spot numbered i . Averaging the e^i over time and filtering yields an estimate for the fields $e_{1,2}(x, y)$. Now we compare that with the definition of the diffusion coefficient:

$$D = \lim_{\Delta t \rightarrow 0} \frac{\langle (x(t + \Delta t) - x(t))^2 \rangle}{\Delta t}.$$

In our situation the limit cannot be reached, due to sampling and consequently we should use methods like the FSLE Aurell et al. (1996), which are ongoing work. Here we show the results for the finite-size spots with $\Delta t = \Delta_s$ fixed to the minimal sampling time. We make of course an error in mixing different spot sizes, which we counteract by choosing homogeneous spots of similar size.

The space-dependent diffusion is then simply estimated by

$$D_{est} = \frac{\overline{\langle (x(t + \Delta_s t) - x(t))^2 \rangle}}{\Delta_s}$$

where averaging over many times is performed. Of course this is a very rough approach, but we will see how far we can go and compare this with the enhancement of thinning. This is, however not the full story: for mixing it can be desirable to have faster than normal diffusion, the characterization of a real process involves *finite* intervals Δt , Δx , and the degree of anomaly is given by the scaling $\Delta t \sim \Delta x^\alpha$, with $\alpha = 2$ for normal diffusion. since we prescribe Δt and determine Δx accordingly, the full statistical characterization is given by the probability function $P(\Delta x, \Delta t)$

6. RESULTS

6.1 Experiment

To capture the movement of the soap film turbulence we use a generic HD video camera which is able to record 1920 times 1080 pixel at 25 frames per second. The maximum speed measured is around 14mm/s so that the frame rate limited minimal resolution is roughly 0.5mm . We use a demountable measuring cell that encloses a aluminum frame holding the film and a small reservoir of the solution. The film is 2.5 cm wide and 4 cm high where the corners are rounded. To measure the temperature of a copper rod which is semi-immersed in liquid nitrogen a PT-100 temperature sensor is placed inside the rod and connected to a digital instrument (Meilhaus RedLab TEMP).

It is vitally important for the long term stability of the film to restrict the exchange of air from the inside of the cell and the outside laboratory atmosphere as evaporation of the film is countered by a saturated atmosphere in the cell. The film is illuminated through the viewing window with a flexible halogen lamp. To minimize reflections the rear panel of the measuring cell is covered by a sheet of black cellular rubber.

The diffused light is reflected by the front and back side of the film where as the front reflection is shifted by $\pi/2$ due to reflecting of an optically thicker medium. If the film thickness is much smaller than $\lambda/4$ of the smallest emitted wavelength the light waves interfere $\pi/2$ out-of-phase and no light is reflected. Hence the name black film. The reason why there is no smooth transition in the intensity of the reflected light is the abrupt change in thickness when the black film is formed. At $\lambda/4$ of the smallest wavelength, which is blue ($\sim 450\text{nm}$) in the case of the used full spectrum halogen bulb, the reflected waves interfere constructively. In addition every other wavelength is reflected as well which sums up to a white color with a blue tint. Before that thickness is reached the film exhibits an orange tint as the film is approximately 200nm thick which corresponds to the amplification of red light and the cancellation of blue. To get an absolute value of the thickness corresponding to a certain color displayed one needs to take into account that the refractive index of the solution is slightly higher than that of pure water. In our setup we cool the film from a spot in the center generating convection in the lower half whereas the top half remains nearly unchanged if no instabilities occur. The latter was first described by Mysels et al. (1959) as irregular mobile films.

6.2 Data Analysis

The captured video data is post-processed to enhance colors and contrast. To analyze the behaviour of domains of the same thickness the video is converted into a binary image where white corresponds to a single color respectively thickness. As the spectrum repeats continually this technique is only valid if the overall thickness deviation is smaller than a full period of the smallest wavelength.

Subsequently in each frame all clusters of the same thickness are numbered and consecutively linked through the following frames (Fig. 4). This enables us to track the

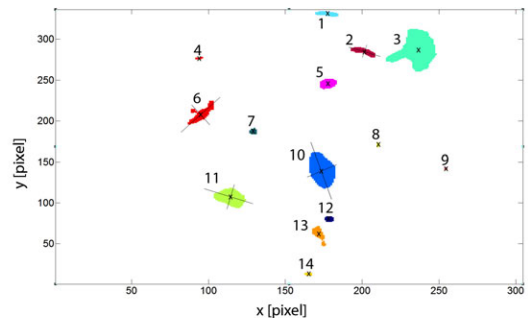


Fig. 4. example of the cluster identification for one frame, including center of mass and selected principle components (not to scale).

volume, velocity, deformation rate and angular velocity of the moving fluid. For each cluster the velocity is calculated using the shift of its center of mass per frame. The deformation rate is calculated by determining the change of the scale of the principal components per frame. Similarly the angular velocity is given by the rotation of the principal component. Averaging over all frames then delivers the spatial characteristics of the flow field generated by the cooling tip. The cluster finding algorithm is operating with a linear backwards memory of variable depth. However for now a tracking of one frame backwards is sufficient to maintain connectivity of each cluster through all frames. The memory needs to be limited as merging or dividing clusters would be considered connected thereby distorting the velocity and deformation rate. As the raw video data is captured in HD resolution the algorithm only keeps the memory frames necessary for the relevant for the current data analysis to prevent a system memory overflow.

The intermittency of the mixing film is described by the probability $P(\Delta x, \Delta t)$. With a selected subset of our data we calculated the distance Δx for fixed Δt (on logarithmic scale). The result is plotted in Fig. 5. We observe basically ballistic transport for small Δt , as could be expected because the more chaotic small scales are not resolved, and the large scale transitions are not found by our cluster analysis. However, note that this is a much faster scaling than for usual thinning, where the thinning procedure is governed by the propagation of the front of the Newton black film, now this is assisted by a ballistic transport downwards. Thus an enhanced thinning due to turbulent mixing is observed. The further analysis and data acquisition is subject to ongoing research.

7. CONCLUSION

We present a novel type of experiments, where the typical Rayleigh-Bénard situation is inverted: we cool from above instead of heating. Putting aside the question of the formation of ice about the needle, a heavy convection is found. Being in almost two dimensions, several fundamental questions can be studied, among them mixing within the film and more specific the enhanced transport of thin film. Since the stability and thinning of films is of

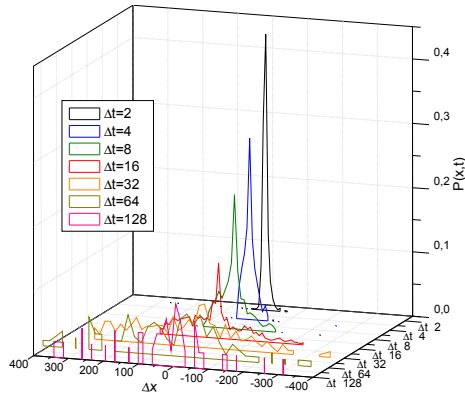


Fig. 5. Probability $P(\Delta x, \Delta t)$ for different time scales Δt . The transport is ballistic over one decade. Larger times are not shown due to the insufficient number of data.

high scientific interest, and of technological relevance, we analyzed our setup under the aspect of mixing.

We found that mixing enhances the thinning of a film considerably, quantitative analysis in this respect will be published elsewhere. The videographic analysis of the thinning procedure enables to track spots of equal thickness and quantify the thinning rate in comparison to normal thinning. We found an enhancement by a factor of roughly 30. This is in correspondence to the effective diffusion approach discussed above.

The open directions we identified are: i) what is the exact effect of temperature. This is very hard to measure, but very important, ii) thickness dependent enhancement, i.e. are different thicknesses advected differently? iii) What if the transport is so violent that a whole area of newton black film is transported from top to bottom? First observations suggest an even much faster thinning of the film. iv) What is the Nusselt number in such a thin film? At present a systematic study is not possible in experiments. All these questions will be subject to numerical investigations to support the experiment and to enhanced experimental setup.

We think that with our extremely simple experiment we can touch deep physical questions on the microscopic nature of thin film flows and treat at the same time very praxis relevant topics.

ACKNOWLEDGEMENTS

We acknowledge the initial gift of the idea by N.P. Abel, the 6-year old son of one of the authors. A. Pikovsky and D. Lohse helped with fruitful discussion, B. Eckhardt encouraged to carry out the experiment in the early stage.

REFERENCES

M. Abel, L. Biferale, M. Cencini, M. Falcioni, D. Vergni, and A. Vulpiani. Exit-time approach to ϵ -entropy. *Phys. Rev. Lett.*, 84(26):6002–6005, 2000.
 Guenter Ahlers, Siegfried Grossmann, and Detlef Lohse. Heat transfer and large scale dynamics in turbulent

rayleigh-bnard convection. *Rev. Mod. Phys.*, 81:503537, 2009.
 E. Aurell, G. Boffetta, A. Crisanti, G. Paladin, and A. Vulpiani. Growth of non-infinitesimal perturbations in turbulence. *Phys. Rev. Lett.*, 77:1262–1265, 1996.
 M. Cencini, F. Cecconi, and A. Vulpiani. *Chaos: from simple models to complex systems*. World Scientific, Singapore, 2009.
 B.V. Derjaguin. *Theory of stability of colloids and thin films*. Consultants Bureau New York and London, 1989.
 D. Exerowa and P.M. Kruglyakov. *Foam and foam films: theory, experiment, application*. Elsevier, New York, 1998.
 C. Isenberg. *The science of soap films and soap bubbles*. Dover Pubns, 1992.
 H. Kellay, XL Wu, and WI Goldburg. Experiments with turbulent soap films. *Physical review letters*, 74(20):3975–3978, 1995.
 BK Martin, XL Wu, WI Goldburg, and MA Rutgers. Spectra of decaying turbulence in a soap film. *Physical Review Letters*, 80(18):3964–3967, 1998.
 RM Muruganathan, R. Krustev, HJ Mller, H. Mhwald, B. Kolaric, and RV Klitzing. Foam films stabilized by dodecyl maltoside. 1. Film thickness and free energy of film formation. *Langmuir: the ACS journal of surfaces and colloids*, 20(15):6352, 2004.
 K.J. Mysels, S. Frankel, and K. Shinoda. *Soap films: studies of their thinning and a bibliography*. Pergamon Press, 1959.
 V.A. Nierstrasz and G. Frens. Marginal regeneration and the Marangoni effect. *Journal of colloid and interface science*, 215(1):28–35, 1999.
 Alexander Oron, Stephen H. Davis, and S. George Bankoff. Long-scale evolution of thin liquid films. *Rev. Mod. Phys.*, 69:931 – 980, 1997. Nice review on the fluid properties in thin liquid films.
 JM Ottino. *The kinematics of mixing: stretching, chaos, and transport*. Cambridge Univ Pr, 1989.
 MA Rutgers, R. Bhagavatula, AA Petersen, and WI Goldburg. Two-dimensional velocity profiles and laminar boundary layers in flowing soap films. *Physics of Fluids*, 8:2847, 1996.
 MA Rutgers, XL Wu, and WB Daniel. Conducting fluid dynamics experiments with vertically falling soap films. *Review of Scientific Instruments*, 72:3025, 2001.
 T. Shakeel and P. Vorobieff. Decaying turbulence in soap films: energy and enstrophy evolution. *Experiments in Fluids*, 43(1):125–133, 2007.
 Todd M. Squires and Stephen R. Quake. Microfluidics: Fluid physics at the nanoliter scale. *Rev. Mod. Phys.*, 77:9771026, 2005.
 HN Stein. On marginal regeneration. *Advances in Colloid and Interface Science*, 34:175–190, 1991.
 C. Stubenrauch, D. Kashchiev, and R. Strey. Phase diagrams of nonionic foam films: construction by means of disjoining pressure versus thickness curves. *Journal of colloid and interface science*, 280(1):244–255, 2004.
 R. Sturman, J.M. Ottino, and S. Wiggins. *The mathematical foundations of mixing*. Cambridge University Press, 2006.
 T.S. Yang, C.Y. Wen, and C.Y. Lin. Interpretation of color fringes in flowing soap films. *Experimental Thermal and Fluid Science*, 25(3-4):141–149, 2001.

B. Bibliography

- [1] V. Bergeron. Measurement of forces and structure between fluid interfaces. *Current Opinion in Colloid & Interface Science*, 4(4):249–255, 1999.
- [2] B.J. Boyd, C.J. Drummond, I. Krodziewska, and F. Grieser. How Chain Length, Headgroup Polymerization, and Anomeric Configuration Govern the Thermotropic and Lyotropic Liquid Crystalline Phase Behavior and the Air-Water Interfacial Adsorption of Glucose-Based Surfactants. *Langmuir*, 16(19):7359–7367, 2000.
- [3] O.C. Bridgeman and E.W. Aldrich. Vapor pressure tables for water. *Journal of Heat Transfer*, pages 279–286, 1964, <http://webbook.nist.gov>, (retrieved July 1, 2010).
- [4] R. Bruinsma. Theory of hydrodynamic convection in soap films. *Physica A Statistical Mechanics and its Applications*, 216:59–76, 1995.
- [5] DOW Chemicals. Freezing points table of glycerin- and water solutions. website, 2010, (<http://www.dow.com/glycerine/resources/table8.htm>).
- [6] Y. Couder, J.M. Chomaz, and M. Rabaud. On the hydrodynamics of soap films. *Physica D*, 37(1-3):384–405, 1989.
- [7] PG De Gennes. Polymers at an interface; a simplified view. *Advances in Colloid and Interface Science*, 27(3-4):189–209, 1987.
- [8] B.V. Derjaguin. *Theory of stability of colloids and thin films*. Consultants Bureau New York and London, 1989.
- [9] D. Exerowa, K. Khristov, and I. Penev. Some Techniques for the Investigation of Foam Stability. *Foams, RJ Akers (ed.), Academic Press, New York*, 1976.
- [10] D. Exerowa and P.M. Kruglyakov. *Foam and foam films: theory, experiment, application*. Elsevier, New York, 1998.
- [11] O. Greffier, Y. Amarouchene, and H. Kellay. Thickness fluctuations in turbulent soap films. *Physical Review Letters*, 88(19):194101, 2002.
- [12] RR Highfield, RP Humes, RK Thomas, PG Cummins, DP Gregory, J. Mingins, JB Hayter, and O. Schaerpf. Critical reflection of neutrons from a soap film. *Journal of Colloid and Interface Science*, 97(2):367–373, 1984.
- [13] C. Isenberg. *The science of soap films and soap bubbles*. Dover Pubns, 1992.
- [14] J.N. Israelachvili and H. Wennerstroem. Entropic forces between amphiphilic surfaces in liquids. *The Journal of Physical Chemistry*, 96(2):520–531, 1992.
- [15] M.N. Jones, K.J. Mysels, and P.C. Scholten. Stability and some properties of the second black film. *Transactions of the Faraday Society*, 62:1336–1348, 1966.

- [16] Y. Jun and XL Wu. Large-scale intermittency in two-dimensional driven turbulence. *Physical Review E*, 72(3):35302, 2005.
- [17] H. Kellay. Dispersion in the enstrophy cascade of two-dimensional decaying grid turbulence. *Physical Review E*, 69(3):36305, 2004.
- [18] H. Kellay and W.I. Goldburg. Two-dimensional turbulence: a review of some recent experiments. *Reports on Progress in Physics*, 65:845–894, 2002.
- [19] H. Kellay, XL Wu, and WI Goldburg. Experiments with turbulent soap films. *Physical Review Letters*, 74(20):3975–3978, 1995.
- [20] Dongseo University Korea. Soap film simulations. website, 2010, (http://kowon.dongseo.ac.kr/~seewhy/CyberExp/interference_soapy_water_film/interference_soapy_water_film_2.htm).
- [21] R. Leberman and A.K. Soper. Effect of high salt concentrations on water structure. *Nature*, 378:364–366, 1995.
- [22] R. Mancinelli, A. Botti, F. Bruni, MA Ricci, and AK Soper. Hydration of sodium, potassium, and chloride ions in solution and the concept of structure maker/breaker. *Journal of Physical Chemistry B*, 111(48):13570–13577, 2007.
- [23] BK Martin, XL Wu, WI Goldburg, and MA Rutgers. Spectra of decaying turbulence in a soap film. *Physical Review Letters*, 80(18):3964–3967, 1998.
- [24] D. Meyer. Surfactant Science and Technology. *VCH F [2bushers], Inc*, 1992.
- [25] R.M. Muruganathan, R. Krustev, H.J. Müller, H. Möhwald, B. Kolaric, and R.V. Klitzing. Foam films stabilized by dodecyl maltoside. 1. Film thickness and free energy of film formation. *Langmuir: the ACS journal of surfaces and colloids*, 20(15):6352, 2004.
- [26] K.J. Mysels, S. Frankel, and K. Shinoda. *Soap films: studies of their thinning and a bibliography*. Pergamon Press, 1959.
- [27] V.A. Nierstrasz and G. Frens. Marginal regeneration in thin vertical liquid films. *Journal of colloid and interface science*, 207(2):209–217, 1998.
- [28] V.A. Nierstrasz and G. Frens. Marginal regeneration and the Marangoni effect. *Journal of colloid and interface science*, 215(1):28–35, 1999.
- [29] A. Oron, S.H. Davis, and S.G. Bankoff. Long-scale evolution of thin liquid films. *Reviews of Modern Physics*, 69(3):931–980, 1997.
- [30] JM Ottino. *The kinematics of mixing: stretching, chaos, and transport*. Cambridge Univ Pr, 1989.
- [31] C.M. Persson, U.R.M. Kjellin, and J.C. Eriksson. Surface pressure effect of poly(ethylene oxide) and sugar headgroups in liquid-expanded monolayers. *Langmuir*, 19(20):8152–8160, 2003.
- [32] C.C. Ruiz. *Sugar-Based Surfactants: Fundamentals and Applications*. CRC, 2008.
- [33] MA Rutgers, R. Bhagavatula, AA Petersen, and WI Goldburg. Two-dimensional velocity profiles and laminar boundary layers in flowing soap films. *Physics of Fluids*, 8:2847, 1996.

- [34] MA Rutgers, XL Wu, and WB Daniel. Conducting fluid dynamics experiments with vertically falling soap films. *Review of Scientific Instruments*, 72:3025, 2001.
- [35] J. Schlarmann, C. Stubenrauch, and R. Strey. Correlation between film properties and the purity of surfactants. *Physical Chemistry Chemical Physics*, 5(1):184–191, 2003.
- [36] T. Schnipper, A. Andersen, and T. Bohr. Vortex wakes of a flapping foil. *Journal of Fluid Mechanics*, 633:411–423, 2009.
- [37] F. Seychelles, Y. Amarouchene, M. Bessafi, and H. Kellay. Thermal Convection and Emergence of Isolated Vortices in Soap Bubbles. *Physical Review Letters*, 100(14):144501, 2008.
- [38] T. Shakeel and P. Vorobieff. Decaying turbulence in soap films: energy and enstrophy evolution. *Experiments in Fluids*, 43(1):125–133, 2007.
- [39] A. Sheludko. Thin liquid films. *Advances in Colloid and Interface Science*, 1(4):391–464, 1967.
- [40] S. Stöckle. *Thin liquid films with nanoparticles and rod-like ions as models for nanofluidics*. PhD thesis, Universitätsbibliothek Potsdam, 2010.
- [41] S. Stöckle, P. Blecua, H. Möhwald, and R. Krastev. Dynamics of Thinning of Foam Films Stabilized by n-Dodecyl- β -maltoside. *Langmuir*, 26 (7):4974–4977, 2010.
- [42] HN Stein. On marginal regeneration. *Advances in Colloid and Interface Science*, 34:175–190, 1991.
- [43] C. Stubenrauch, D. Kashchiev, and R. Strey. Phase diagrams of nonionic foam films: construction by means of disjoining pressure versus thickness curves. *Journal of Colloid and Interface Science*, 280(1):244–255, 2004.
- [44] C. Stubenrauch and R. Miller. Stability of foam films and surface rheology: an oscillating bubble study at low frequencies. *Journal of Physical Chemistry B*, 108(20):6412–6421, 2004.
- [45] R. Sturman, J.M. Ottino, and S. Wiggins. *The mathematical foundations of mixing*. Cambridge University Press, 2006.
- [46] T.S. Yang, C.Y. Wen, and C.Y. Lin. Interpretation of color fringes in flowing soap films. *Experimental Thermal and Fluid Science*, 25(3-4):141–149, 2001.
- [47] J. Zhang and XL Wu. Velocity intermittency in a buoyancy subrange in a two-dimensional soap film convection experiment. *Physical review letters*, 94(23):234501, 2005.
- [48] J. Zhang, XL Wu, and K.Q. Xia. Density fluctuations in strongly stratified two-dimensional turbulence. *Physical review letters*, 94(17):174503, 2005.
- [49] L. Zhang, P. Somasundaran, and C. Maltesh. Electrolyte Effects on the Surface Tension and Micellization of n-Dodecyl- β -d-Maltoside Solutions. *Langmuir*, 12(10):2371–2373, 1996.

- [50] R. Zhang, L. Zhang, and P. Somasundaran. Study of mixtures of n-dodecyl- β maltoside with anionic, cationic, and nonionic surfactant in aqueous solutions using surface tension and fluorescence techniques. *Journal of Colloid and Interface Science*, 278(2):453–460, 2004.